

**Measurement of Elliptic Flow in  $p$ +Au Collisions at  $\sqrt{s_{NN}} =$   
200 GeV using the PHENIX Detector at RHIC**

by

**Theodore Koblesky**

B.S., University of Illinois, 2011

A thesis submitted to the  
Faculty of the Graduate School of the  
University of Colorado in partial fulfillment  
of the requirements for the degree of  
Doctor of Philosophy  
Department of Physics  
2017

This thesis entitled:  
Measurement of Elliptic Flow in  $p+\text{Au}$  Collisions at  $\sqrt{s_{NN}} = 200$  GeV using the PHENIX  
Detector at RHIC  
written by Theodore Koblesky  
has been approved for the Department of Physics

---

Professor James Nagle

---

Professor Dennis Perepelitsa

Date \_\_\_\_\_

The final copy of this thesis has been examined by the signatories, and we find that both the content and the form meet acceptable presentation standards of scholarly work in the above mentioned discipline.

Koblesky, Theodore (Ph.D., High Energy Nuclear Physics)

Measurement of Elliptic Flow in  $p+\text{Au}$  Collisions at  $\sqrt{s_{NN}} = 200$  GeV using the PHENIX Detector  
at RHIC

Thesis directed by Professor James Nagle

The Quark Gluon Plasma (QGP), a hot and dense state of matter in which quarks are not confined inside hadrons, is thought to be the same as the matter comprising the entire universe approximately one microsecond after the Big Bang. In  $\text{Au}+\text{Au}$  collisions at  $\sqrt{s_{NN}} = 200$  GeV at the Relativistic Heavy Ion Collider (RHIC) and  $\text{Pb}+\text{Pb}$  collisions at  $\sqrt{s_{NN}} = 2.76$  TeV at the Large Hadron Collider (LHC), QGP has been discovered to have unique properties, such as its opacity to color charges and the fact that it behaves like a near-perfect fluid. Collective behavior in the form of a substantial elliptical azimuthal anisotropy ( $v_2$ ) in the momentum distribution of final state particles has been observed, indicating a strongly-coupled, hydrodynamically flowing medium.

Recently, features of collectivity have been detected in high-multiplicity, small collision systems thought to be too small to produce the QGP, such as  ${}^3\text{He}+\text{Au}$  and  $d+\text{Au}$  at  $\sqrt{s_{NN}} = 200$  GeV,  $p+\text{Pb}$  at  $\sqrt{s_{NN}} = 5$  TeV, and in  $p+p$  at  $\sqrt{s} = 13$  TeV events. In order to constrain models seeking to describe this phenomena, collision systems with distinct initial collision geometries were run at RHIC:  ${}^3\text{He}+\text{Au}$  for triangular geometry,  $d+\text{Au}$  for elliptical geometry, and  $p+\text{Au}$  for circular geometry. Together with coauthors, in a theory paper published in 2014, we proposed the suite of measurements at RHIC of the three collision systems [1].

This thesis is the completion of that set of three measurements, by measuring  $v_2$  in the  $p+\text{Au}$  system. This thesis gives details on the analysis techniques used to make the measurement including the quality assurance of the data, the optimization of the midrapidity charged hadron cuts, and the event plane angle calibration. Special attention is given to correcting the systematic effects produced by the beam alignment unique to the  $p+\text{Au}$  dataset in order to make the  $v_2$  measurement with sufficient precision. Comparisons of  $v_2$  in the three collision systems and various theoretical

models are made and the results appear to be consistent with a QGP being formed. I am a coauthor on the experimental paper with these thesis results which has been published in Physical Review C [2].

## **Dedication**

To all the lonely people, where do they all belong?

## Acknowledgements

There are many people without whom I could not have completed my thesis: most especially my lab, my friends, and my family. While it would take far too long to thank all the people who have helped make this work possible, I'd like to take the opportunity to acknowledge a number of people who were most important.

My advisor, Professor Jamie Nagle, made it possible with his guidance and patience for me to produce my thesis. He is the sharpest person I have ever worked with and always serves as an inspiration. Everyone in my lab was very helpful, particularly Javier and Ron who generously gave me amazing feedback and their time. Everyone on PHENIX was helpful and welcoming and a pleasure to work with.

Thanks also go to my supportive friends: Nathan, Dave, Taylor. To my friend Conner, truly you helped me get through the hard times.

Finally, my family was instrumental in my accomplishment not only in the specific ways they helped my project, but by helping me grow as a human being. My father, David, helped me with the graphics in my thesis. My sister, Norah, gave me valuable advice on my presentation. My mother, Laurie, contributed so much that it is difficult to overstate. She supported me in uncountably many ways, and I will be always grateful. Thank you.

## Contents

### Chapter

<b>1</b>	<b>Physics Overview</b>	<b>1</b>
1.1	The Standard Model . . . . .	1
1.1.1	Quantum Chromodynamics . . . . .	3
1.2	Quark Gluon Plasma . . . . .	7
1.2.1	The QGP Evolution Timeline . . . . .	9
1.2.2	Emergent Properties of the QGP . . . . .	10
1.2.2.1	Particle Energy Loss . . . . .	11
1.2.2.2	Collective Flow and Azimuthal Anisotropy . . . . .	14
<b>2</b>	<b>Collectivity and Flow in QCD Systems</b>	<b>17</b>
2.1	A Conceptual Understanding of Collectivity and Flow . . . . .	17
2.1.1	Initial Conditions . . . . .	18
2.2	Mathematical Introduction to Measuring and Quantifying Flow . . . . .	19
2.2.1	Two-Particle Correlations . . . . .	19
2.2.2	Flow Harmonics . . . . .	22
2.2.3	Cumulants . . . . .	23
2.2.4	Event Plane Formulation . . . . .	24
2.3	An Overview of Heavy Ion Collectivity Models . . . . .	26
2.3.1	Initial Condition Models . . . . .	26

2.3.1.1	Monte-Carlo Glauber	27
2.3.1.2	IP-Glasma	28
2.3.1.3	Comparison between IP-Glasma and MC-Glauber	30
2.3.2	Medium Evolution Models	30
2.3.2.1	Hydrodynamic Modeling	30
2.3.2.2	Hybrid Models: SONIC and superSONIC	32
2.3.3	AMPT	33
2.4	A Review of Flow Measurements in Small Collision Systems	34
2.4.1	Nearside Ridge in Small Systems	34
2.4.2	Mass Ordering in $v_2$	36
2.4.3	Multi-Particle Cumulants and Fluctuations	37
2.4.4	Measurements Made at RHIC	39
<b>3</b>	<b>Experiment Setup</b>	<b>42</b>
3.1	RHIC	42
3.2	PHENIX	44
3.2.1	PHENIX Magnet System	46
3.2.2	Beam Beam Counter	47
3.2.3	Forward Vertex Detector	48
3.2.4	Drift Chamber	49
3.2.5	Pad Chambers	50
3.2.6	Ring Imaging Cherenkov Detector	51
3.2.7	PHENIX Data Acquisition System	52
3.2.7.1	Triggering	52
3.2.7.2	Event Builder	53
3.2.8	Run 15	54
3.2.8.1	Beam Collision Geometry	56

3.2.9	Centrality Determination	57
<b>4</b>	<b>Analysis</b>	<b>61</b>
4.1	The Building Blocks of the Measurement	61
4.1.1	Central Arm Tracks	61
4.1.1.1	Signalization of PC Variables	65
4.1.2	FVTX Clusters	65
4.1.3	BBC PMTs	66
4.2	The Event Plane Method	68
4.2.1	Event Plane Resolution Calculation	69
4.2.2	Event Plane Flattening Calibration	71
4.3	East West $v_2$ Discrepancy	73
4.4	Correcting for the Effects of Beam Alignment	74
4.4.1	Analytic Correction Method	77
4.4.2	FVTX Inverse Phi Weighting	78
4.4.3	BBC Charge Weighting	79
4.4.4	Applying Weighting to $v_2$	82
4.5	Other Sources of Systematic Uncertainty	86
4.5.1	Effect of Event Pile-Up	86
4.5.2	Event Plane Detectors	86
4.5.3	Track Background	87
4.5.4	Effects of Non-Flow	88
4.6	Systematic Uncertainties Summary	90
<b>5</b>	<b>Results and Discussion</b>	<b>92</b>
5.1	$v_2$ Measurement	92
5.1.1	Non-flow Contribution	92
5.2	Comparison with Other Species at $\sqrt{s_{NN}} = 200$ GeV 0–5% Centrality	93

5.3	Comparison with Theory	95
5.3.1	Initial Conditions and Eccentricity	97
5.3.2	Comparison to Alternative Models	102
<b>6</b>	Summary and Outlook	<b>105</b>
<b>Bibliography</b>		<b>109</b>
<b>Appendix</b>		
<b>A</b>	$v_2(p_T)$ with Different $\Psi_2$ Weighting	<b>116</b>
<b>B</b>	Summary of Acronyms and Terms	<b>131</b>

## Tables

### Table

1.1	All four of the fundamental forces and the effective strengths of each relative to gravity. Gravity is not covered by the SM but is included for completeness. . . . .	2
3.1	An example 2015 $p$ +Au at $\sqrt{s_{NN}} = 200$ GeV trigger configuration and parameters. A trigger's scale down number reduces its rate by $1/(1+\text{scale down})$ . . . . .	53
3.2	Some relevant RHIC parameters from Run 15. . . . .	55
4.1	Quality categorization of CA tracks, as a function of PC1 and DC wire hits. The quality parameters used in this analysis are 31 and 63 to maximize information available. Table from Ref [3]. . . . .	64
4.2	Quality categorization of CA tracks, as a function of DC wire momentum information. The quality parameters used in this analysis are 31 and 63 to maximize information available. Table from Ref [3]. . . . .	64
4.3	CA Track cuts for each relevant variable and their units. . . . .	65
4.4	The event plane angle resolutions for the FVTXS and the BBCS for the second and third order harmonics. . . . .	70
4.5	Systematic uncertainties given as a percent of the $v_2$ measurement. Note that the non-flow contribution is $p_T$ dependent and the value here quoted corresponds to the highest measured $p_T$ . . . . .	91



## Figures

### Figure

1.1	The fundamental particles of the SM arranged to highlight flavor (horizontal) and charge (vertical) patterns among the particles for the first three columns. The five particles on the right are the force carriers. All of these are thought to be the smallest discrete pieces of matter which make up everything else in the universe [5]. . . . .	2
1.2	Parton distribution functions (PDF) of the momentum fraction $x$ in the proton extracted from data taken by the H1 Collaboration. The curves $xS$ , $xg$ , $xu_v$ , and $xd_v$ correspond to PDFs of sea quarks, gluons, up valence quarks, and down valence quarks in the proton. The gluon $g$ and sea $S$ distributions are scaled by a factor 0.01. The uncertainties include experimental (inner) and model (middle) uncertainties and the parametrization variations (outer) [6]. . . . .	5
1.3	The strong coupling $\alpha_s$ as a function of energy of the square root of the momentum transfer $Q$ [7]. . . . .	6
1.4	QCD phase diagram of temperature on the y-axis and net baryonic density on the $x$ -axis [8]. . . . .	7
1.5	Disappearance of degrees of freedom through the evolution of the Universe in time and how this affects the fractional drop of temperature compared to red-shift [9]. . .	8
1.6	The energy density $\epsilon$ divided by $T^4$ vs temperature $T$ at the physical value of the light quark mass [10]. . . . .	8

1.7 Relativistic heavy ion collision evolution timeline. Three distinct phases and their times are shown as well as the particles produced [11]. . . . .	11
1.8 The $R_{AA}$ vs $p_T$ of $\pi^0$ mesons produced in Au+Au collisions at $\sqrt{s_{NN}} = 200$ GeV by PHENIX at RHIC for two different collision multiplicity classes [12]. . . . .	13
1.9 A diagram of a heavy ion collision. The blue shapes are the two colliding nuclei and the elliptical yellow shape is the collision overlap region which forms the medium. In the next instant of time the two nuclei would travel farther along the collision axis (into and out of the page) and the medium would expand along the direction of the arrows [13]. . . . .	15
1.10 $v_n$ vs $p_T$ for RHIC Au+Au at $\sqrt{s_{NN}} = 200$ GeV and for LHC Pb+Pb at $\sqrt{s_{NN}} = 2.76$ TeV for mid-peripheral events for harmonic orders $n$ up to five. The colored curves are the hydrodynamic calculations. The $\eta/s$ is the viscosity parameter used in the calculations [14]. . . . .	16
2.1 A diagram demonstrating the initial state geometry being transformed into the final state momentum anisotropy. The left depicts two spherical nuclei colliding parallel to the z-axis. The pair of nuclei leave behind an ellipsoidal shaped medium. This ellipsoid hydrodynamically evolves such that it expands along the steepest pressure gradient, which corresponds to the transverse direction. The right depicts the elliptical pattern present in the transverse momentum distribution of the final state particles after the medium has finished evolving [14]. . . . .	18
2.2 A diagram of the possible initial conditions of heavy ion collisions. The impact parameter is the red line. The language used in heavy ion physics is as follows: the larger the overlap between the colliding nuclei, the more central it is, the smaller the overlap, the more peripheral it is [15]. . . . .	19

2.3	The left plot is 2-D two-particle correlation function for $p+p$ collisions at $\sqrt{s_{NN}} = 7$ TeV for hadrons with the same trigger and associated $p_T$ range of $1.0 \text{ GeV}/c < p_T < 3.0 \text{ GeV}/c$ for all events measured by CMS[16]. The left plot is 2-D two-particle correlation function for Pb+Pb collisions at $\sqrt{s_{NN}} = 2.76 \text{ TeV}$ 0-10% centrality events for trigger hadrons with $3 < p_T^t < 4 \text{ GeV}/c$ and associated hadrons with $2 < p_T^a < 2.5 \text{ GeV}/c$ measured by ALICE [17].	21
2.4	The 1-D correlation function in Pb+Pb at $\sqrt{s_{NN}} = 2.76 \text{ TeV}$ for the most central events for trigger hadrons with $2 < p_T^t < 2.5 \text{ GeV}/c$ and associated hadrons with $1.5 \text{ GeV}/c < p_T^a < 2 \text{ GeV}/c$ . The 1-D two-particle correlation function is a projection in $0.8 <  \Delta\eta  < 1.8$ from the 2-D correlation function, the 2-D correlation function being similar to that of the right panel of Figure 2.3. The black dotted points are the values of the correlation function and the colored lines are the first five cos Fourier decomposition components. The black dotted line is the sum of these five components [17].	23
2.5	Diagram showing from the point of view of the beam of several variables used to characterize events. The spectators are the nucleons that do not participate in the collision, as opposed to the participants that do participate in the collision. The impact parameter is denoted as $b$ and $\Psi_{\text{PP}}$ is the reaction or participant plane angle. $\phi$ is the standard azimuthal angle and $\varphi = \phi - \Psi_{\text{PP}}$ . Adapted from [15].	25
2.6	Glauber Monte Carlo event (Au+Au $\sqrt{s_{NN}} = 200 \text{ GeV}$ with impact parameter $b = 6 \text{ fm}$ ) viewed in the transverse plane and along the beam axis in the left and right panels, respectively. The darker color disks correspond to the participating nucleons [18].	29
2.7	Initial energy density distributions (arbitrary units) in the transverse plane in two different heavy-ion collision events for IP-glasma (top) MC-Glauber (bottom) models [19].	31

2.8	An example time evolution of a ${}^3\text{He}+\text{Au}$ event from the initial state to final state. The color scale indicates the local temperature and the arrows are proportional to the velocity of the fluid cell from which the arrow originates [1]. . . . .	33
2.9	2-D two-particle correlation function for $p+p$ collisions at $\sqrt{s} = 7$ TeV for hadrons with $1.0 < p_T < 3.0$ GeV/c in high multiplicity events, with greater than 109 charged particles, and for any multiplicity of events are shown in the left and right panels, respectively [16]. . . . .	35
2.10	2-D two-particle dihadron correlation function for $p+\text{Pb}$ collisions for 0-20% and 60-100% centrality events as measured by the ALICE detector in the left and middle panel, respectively. The rightmost panel shows the subtraction of the left panel by the middle panel to remove non-flow effects [20]. . . . .	36
2.11	$v_2(p_T)$ for different particles (see legend) in $\text{Pb-Pb } \sqrt{s_{NN}} = 2.76$ TeV 10-20% events as measured by the ALICE detector (left) [21] and the $v_2(p_T)$ for different particles (see legend) in $\text{p-Pb } \sqrt{s_{NN}} = 5.02$ TeV for 0-20% events that were subtracted by peripheral 60-100% events (right) [20]. The $\Delta\eta$ gap at minimum is 0.9 units. The $v_2$ is extracted directly from the two particle correlation function shown in Figure 2.10. . . . .	37
2.12	Elliptic flow measurements made using the 2nd, 4th, 6th, and 8th multi-particle cumulants, where the 2nd multi-particle is subtracted by peripheral events. Also the Lee Yang zero method non-flow elimination method is shown. These quantities are plotted vs the event multiplicity measured as $N_{trk}^{offline}$ , which is the number of charged particle tracks observed during the offline analysis averaged over $0.3 \text{ GeV/c} < p_T < 3.0 \text{ GeV/c}$ and over $ \eta  < 2.4$ . The left panel is $v_2^{sub}\{2,  \Delta\eta  > 2\}$ , $v_2\{4\}$ , and $v_2\{6\}$ in $p+p$ collisions at $\sqrt{s} = 13$ TeV. The middle panel $v_2^{sub}\{2,  \Delta\eta  > 2\}$ , $v_2\{4\}$ , $v_2\{6\}$ , and $v_2\{8\}$ , in $p+\text{Pb}$ at $\sqrt{s_{NN}} = 5$ TeV collisions. The right panel is $v_2^{sub}\{2,  \Delta\eta  > 2\}$ , $v_2\{4\}$ , $v_2\{6\}$ , and $v_2\{8\}$ in $\text{Pb+Pb}$ collisions at $\sqrt{s_{NN}} = 2.76$ TeV. The error bars correspond to the statistical uncertainties, while the shaded regions correspond to the systematic uncertainties [22]. . . . .	39

2.13 $v_n(p_T)$ measured for $d+\text{Au}$ and ${}^3\text{He}+\text{Au}$ at $\sqrt{s_{NN}} = 200$ GeV for 0-5% central events. $v_2$ was measured for both systems and $v_3$ was measured for ${}^3\text{He}+\text{Au}$ . The grey boxes correspond to systematic uncertainties [23]. . . . .	40
2.14 $v_2(p_T)$ for $d+\text{Au}$ and ${}^3\text{He}+\text{Au}$ at $\sqrt{s_{NN}} = 200$ GeV 0-5% centrality events for $\pi^\pm$ and $p+\bar{p}$ separately measured by PHENIX. The boxes correspond to the systematic uncertainty [23]. . . . .	41
3.1 An aerial view of the accelerator chain in BNL starting at the Tandems (in gold) and ending at the RHIC ring (in blue and yellow for the two counter-circulating beams). STAR and PHENIX can be seen at two of the interaction regions. The ring is 2.38 miles in circumference [24]. . . . .	43
3.2 A cross-section diagram of the PHENIX detector from the incoming beam's perspective (top) and a cross-section diagram of the PHENIX detector from the side (bottom). The central arm detectors are not shown in the bottom diagram [25]. . . . .	45
3.3 The PHENIX coordinate system. The origin is in the middle of the PHENIX detector at the collision point. North and south are parallel to the beam axis. East and west are transverse to the beam axis. Central detectors have a west and an east arm on either side of the beam. Forward detectors have a north and a south arm relative to the origin. . . . .	46
3.4 PHENIX magnetic field lines from the MMS, CM, and MMN, (left) and the total magnetic field strength from the CM vs the radial distance from the center of PHENIX at $\phi = 0$ (right) [26]. . . . .	47
3.5 Photographs of the BBC detector. The left is of a single detector element consisting of a quartz radiator and a PMT. The right is of one of the BBC arms, consisting of 64 detector elements [27]. . . . .	48

3.6	A photograph of half of the FVTX. In the cutaway, one sees the half disks on either end of the picture (left) and a schematic of the FVTX at a slightly different angle (right). The FVTX is only 20 cm in the $z$ direction from the PHENIX coordinate system origin (the center of each picture) [25]. . . . .	49
3.7	A diagram of the DC titanium frame that encloses the detector (left) and a diagram of the X, U, and V wires in the DC (right) [27]. . . . .	50
3.8	Ratio of energy to momentum for all Drift Chamber tracks (dashed-dotted line), and tracks associated with RICH hits (solid line) in Au+Au $\sqrt{s_{NN}} = 200$ GeV collisions. The $p$ range is 1.1 – 1.2 GeV/c [28]. . . . .	51
3.9	Diagram of a granule. Granules are the building blocks of the PHENIX DAQ. Each detector subsystem has at least one granule. This granule shows the BBC. . . . .	54
3.10	Diagram of the event builder. . . . .	55
3.11	The distribution of BBC charges in $p$ +Au at $\sqrt{s_{NN}} = 200$ GeV events for different triggers. The black curve is the distribution of charges for the minimum bias trigger. The blue and red curves are the distributions of charges for the high multiplicity trigger. The red curve being scaled by a factor of 1/40 to show agreement with the black curve. The definition of the top 5% more central events are BBC south charges $\geq 48.0$ . The plot shows the large enhancement of the number of 0-5% centrality events that are gained using the high multiplicity trigger compared to the number of 0-5% centrality from the minimum bias trigger alone. . . . .	56
3.12	A vector diagram illustrating the yellow and blue beam angle confirmation relative to the PHENIX coordinate system. . . . .	57
3.13	The BBC $z$ -vertex distribution in a typical $p$ +Au run for different triggers as described in Table 3.1. The teal curve is the BBC(>0 PMTs) novertex trigger, the blue is the BBC(>0 PMTs), and the magenta is the BBC(>0 PMTs) narrowvertex. . . . .	58

3.14	A Monte Carlo Glauber d+Au event display. Each circle is a nucleon and filled circles are nucleons with at least one collision. The red nucleons are from the projectile (deuteron) and the green nucleons are participants from the target (gold) [29]. . . . .	58
3.15	Real data for BBCs charge shown as open circles and MC-Glauber + NBD (top). The colors correspond to the various percentiles relative to the total inelastic $p$ +Au cross section, from right to left: 0–5%, 5–10%, 10–20%, 20–30%, 30–40%, 40–50%, 50–60%, 60–70%, and 70–84%. The blue and red curves correspond to the minimum bias trigger efficiency in all inelastic collisions and inelastic collisions producing a particle at mid-rapidity, respectively (bottom). . . . .	60
4.1	Reference coordinate system for the PHENIX detector. The origin is set at the collision point, around which the detector is centered. The beam runs parallel to the (longitudinal) $z$ –axis, where the direction of positive $z$ is defined as <b>north</b> . The <b>east</b> and <b>west</b> directions are defined as perpendicular to the longitudinal direction, where the direction of positive $x$ is defined as west. . . . .	62
4.2	Momentum resolution $\sigma_p/p$ as a function of the reconstructed track momentum, $p$ for simulated single-particle events [30] (left) and the transverse momentum $p_T$ distribution of CA tracks in $p$ +Au events at $\sqrt{s_{NN}} = 200$ GeV. High $p_T$ tracks ( $p_T > 5$ GeV/c) observed correspond to unsubtracted background (right). . . . .	63
4.3	The distribution of (left) $n0$ , i.e., the number of PMTs fired in the RICH, and (right) $zed$ , i.e., the longitudinal position of tracks in the DC, for CA tracks in 0–5% central $p$ +Au events at $\sqrt{s_{NN}} = 200$ GeV. The structure observed in the $zed$ distribution corresponds to a gap in the detector acceptance. . . . .	63
4.4	The PC3 matching $d\phi$ fit in range $1.0 \text{ GeV}/c < p_T < 1.1 \text{ GeV}/c$ for positive a) and negative b) hadrons and the $dz$ signalization for positive c) and negative d) hadrons. The blue and pink lines are single Gaussian fits to the signal and background, respectively, which are combined in the red line. . . . .	66



4.11 A corrected measurement of $v_2(p_T)$ with the FVTXS (top two panels) and the BBCS (bottom two panels) event plane for the $p+\text{Au}$ $\sqrt{s_{NN}} = 200$ GeV. The default resolution as shown in Table 4.4 is used. The plotting conventions are the same as described in the caption of Figure 4.9. . . . .	76
4.12 (left) Cartoon diagram illustrating $\eta$ acceptance shift due to a beam offset in one of the FVTXS layers. (right) Pseudorapidity distribution of charged particles from the AMPT Monte Carlo generator for $p+\text{Au}$ $\sqrt{s_{NN}} = 200$ GeV, showing the shift in $\eta$ acceptance. . . . .	77
4.13 The modification of the $\eta$ acceptance as a function of $\phi$ for the FVTX first layer (left) and the calculated correction factor from this modification (right). . . . .	78
4.14 These four panels show the FVTX $\phi$ dependent cluster weighting when calculating the FVTX event plane for each layer separately for events when a collision vertex in $z$ is around 0. There are some $\phi$ regions where weight factor is outside of the dotted line bounds. This indicates that either there was a severe deficit or excess of clusters measured in the region. Later, we will examine the effect of keeping these regions or cutting them out on the $v_2$ measurement. . . . .	80
4.15 The black is the FVTX weighting and the blue is the analytic weighting. They have good agreement. . . . .	81
4.16 Shown here is BBC the multiplicative weight factor $F$ used when calculating the modified event plane for events where the collision vertex in $z$ is around 0. The $y$ -axis is the weight factor and the $x$ -axis is the PMT number for the BBCS (there are 64 total in the BBCS). . . . .	81



4.19 Plotted is the BBC correction summary where the y-axis is the east/west $v_2$ ratio and the x-axis is the different subset of PMTs used to calculate the $v_2$ . The black markers correspond to the default corrections. The red boxes correspond to the corrections with the analytic weighting shown in Figure 4.13. Finally, the blue diamonds correspond to the BBC inverse $\phi$ charge weighting as shown in Section 4.4.3. The first column is the quantity calculated from all PMTs. Columns 2 through 6 are using PMTs from certain rings as defined in Figure 4.6. Ring 1 is the hardest to correct. The first column should approximately be the average of all the other columns. . . . .	84
4.20 FVTXS $v_2$ event plane measurement corrected with inverse $\phi$ weighting and 20% cut with FVTXS layer 3 excluded (top) and BBCS $v_2$ event plane measurement corrected with $p+p/p+\text{Au}$ ratio weighting (bottom). . . . .	85
4.21 The distribution of BBC PMT timing values. The x-axis is the difference between the southern BBC PMT $t_0$ – the mean $t_0$ in the south. An example of a normal event (left) and an example pile-up event (right), are shown. . . . .	87
4.22 $v_2(p_T)$ measured separately in the BBCS and the FVTXS after beam alignment corrections (left) and the ratio of $v_2^{\text{FVTXS}}$ to $v_2^{\text{BBCS}}$ (right). The red line is the average of the ratio across $p_T$ . . . . .	87
4.23 2D profile of a correlation function in $\Delta\eta\Delta\phi$ space of a dijet event. The area bounded by red dotted lines represents the exclusion zone in $\Delta\eta$ , such that the measurement is made only using data from outside of the exclusion zone to reduce non-flow contributions. . . . .	89
4.24 (a) The second order harmonic coefficients $c_2(p_T)$ for long range angular correlations in 0%–5% $p+\text{Au}$ collisions, as well as for minimum bias $p+p$ collisions. The latter are scaled down by the factor $(\sum Q^{\text{BBC-S}})_{p+p} / (\sum Q^{\text{BBC-S}})_{p\text{Au}}$ . (b) The ratio of the two harmonics is plotted with the corresponding statistical errors. . . . .	90

5.1	The $v_2$ measurement of $p+\text{Au}$ at $\sqrt{s_{NN}} = 200$ GeV 0–5% centrality. . . . .	93
5.2	The $v_2$ measurement of $p+\text{Au}$ at $\sqrt{s_{NN}} = 200$ GeV 0–5% centrality with the statistical and systematic errors corresponding to the bars and the boxes respectively. The stars are the same $p+\text{Au}$ points but with the non-flow estimate subtracted rather than treated as a systematic uncertainty. . . . .	94
5.3	$v_2$ of charged hadrons within $ \eta  < 0.35$ in 0–5% centrality $p+\text{Au}$ at $\sqrt{s_{NN}} = 200$ GeV events compared to the $v_2$ of charged hadrons in 0–5% centrality $d+\text{Au}$ and ${}^3\text{He}+\text{Au}$ events at $\sqrt{s_{NN}} = 200$ GeV. . . . .	96
5.4	$v_2$ of charged hadrons within $ \eta  < 0.35$ in 0–5% $p+\text{Au}$ , $d+\text{Au}$ , and ${}^3\text{He}+\text{Au}$ central collisions, compared to hydrodynamic calculations using the SONIC model, matched to the same multiplicity as the data. Note that the data points shown include non-flow contributions, whose estimated magnitude is accounted for in the asymmetric systematic uncertainties. . . . .	97
5.5	The top three panes show the transverse spatial locations of the initial hot spots of the three collision species, $p+\text{Au}$ , $d+\text{Au}$ , and ${}^3\text{He}+\text{Au}$ , respectively. The bottom three plots show the resulting medium produced from the overlapping hot spots as well as the resulting particle momentum vector field as calculated from a hydrodynamic model, calculation details in [31] . . . . .	99
5.6	$v_2$ of charged hadrons within $ \eta  < 0.35$ in 0–5% $p+\text{Au}$ , $d+\text{Au}$ , and ${}^3\text{He}+\text{Au}$ central collisions, divided by their corresponding eccentricity $\varepsilon_2$ from MC-Glauber calculations, compared to SONIC calculations of the same quantity. Note that the data points shown include non-flow contributions, whose estimated magnitude is accounted for in the asymmetric systematic uncertainties. . . . .	100

5.7 $v_2/\varepsilon_2$ versus $\varepsilon_2$ with the flow coefficient for pions evaluated at $p_T = 1.0$ GeV/c from $p$ +Au, $d$ +Au, and $^3\text{He}+\text{Au}$ central ( $b < 2$ fm) events (which roughly corresponds to 0–5% centrality). The results are with input parameters $\eta/s = 1/4\pi$ and initial Gaussian smearing $\sigma = 0.4$ fm and a freeze-out temperature of $T_F = 150$ MeV. Diagrams of two possible $d$ +Au initial configurations are overlayed on top of the plot. Increasing distance between the two $d$ +Au nucleons correspond to a larger $\varepsilon_2$ [1].	101
5.8 Centrality dependence of $\varepsilon_2$ calculated in a variety of small collision systems with a variety of models for collision detection [disklike (left), Gaussian (middle), quark-subdivided nucleons with $\sigma_g = 0.3$ fm (right)] [32].	102
5.9 Transverse momentum dependence of $v_2$ in central 0–5% (a) $p$ +Au, (b) $d$ +Au, and (c) $^3\text{He}+\text{Au}$ collisions at $\sqrt{s_{NN}} = 200$ GeV. Theoretical calculations from AMPT, SuperSONIC, and IP-Glasma+Hydro are shown in each panel. Note that the data points shown include non-flow contributions, whose estimated magnitude is accounted for in the asymmetric systematic uncertainties.	104
6.1 $v_2$ of charged hadrons within $ \eta  < 0.35$ in 0–5% centrality $p$ +Au, $d$ +Au, and $^3\text{He}+\text{Au}$ at $\sqrt{s_{NN}} = 200$ GeV, compared with hydrodynamic calculations using the SONIC model, matched to the same multiplicity as the data [33].	106
6.2 The total space-time volume as a function of $\sqrt{s_{NN}}$ in heavy ion collisions calculated by a hydrodynamic model [34].	107
6.3 Calculations of $v_2(p_T)$ $d$ +Au events at various $\sqrt{s_{NN}}$ (given on the upper right of each panel) for AMPT, SONIC, and SuperSONIC models. Note that there are data points in the lower right panel due to the fact that the $v_2$ in $d$ +Au at $\sqrt{s_{NN}} = 200$ GeV has been measured previously by PHENIX from data taken in 2008 [34].	108
A.1 FVTXS event plane measurement with default correction and FVTX layers 1, 2, and 4 of $v_2(p_T)$ with the for the $p$ +Au $\sqrt{s_{NN}} = 200$ GeV (left) and the ratio of the east and west $v_2$ measurements to the inclusive $v_2$ (right).	116

A.2 FVTXS event plane measurement with inverse $\phi$ weighting and FVTX layers 1, 2, and 4 of $v_2(p_T)$ with the for the $p+\text{Au}$ $\sqrt{s_{NN}} = 200$ GeV (left) and the ratio of the east and west $v_2$ measurements to the inclusive $v_2$ (right). . . . .	117
A.3 FVTXS event plane measurement with analytic weighting and a 20% cut and FVTX layers 1, 2, and 4 of $v_2(p_T)$ with the for the $p+\text{Au}$ $\sqrt{s_{NN}} = 200$ GeV (left) and the ratio of the east and west $v_2$ measurements to the inclusive $v_2$ (right). . . . .	117
A.4 FVTXS event plane measurement with inverse $\phi$ weighting and a 20% cut and FVTX layers 1, 2, and 4 of $v_2(p_T)$ with the for the $p+\text{Au}$ $\sqrt{s_{NN}} = 200$ GeV (left) and the ratio of the east and west $v_2$ measurements to the inclusive $v_2$ (right). . . . .	117
A.5 FVTXS event plane measurement with default correction and FVTX layer 1 of $v_2(p_T)$ with the for the $p+\text{Au}$ $\sqrt{s_{NN}} = 200$ GeV (left) and the ratio of the east and west $v_2$ measurements to the inclusive $v_2$ (right). . . . .	118
A.6 FVTXS event plane measurement with inverse $\phi$ weighting and FVTX layer 1 of $v_2(p_T)$ with the for the $p+\text{Au}$ $\sqrt{s_{NN}} = 200$ GeV (left) and the ratio of the east and west $v_2$ measurements to the inclusive $v_2$ (right). . . . .	118
A.7 FVTXS event plane measurement with analytic weighting and a 20% cut and FVTX layer 1 of $v_2(p_T)$ with the for the $p+\text{Au}$ $\sqrt{s_{NN}} = 200$ GeV (left) and the ratio of the east and west $v_2$ measurements to the inclusive $v_2$ (right). . . . .	118
A.8 FVTXS event plane measurement with inverse $\phi$ weighting and a 20% cut and FVTX layer 1 of $v_2(p_T)$ with the for the $p+\text{Au}$ $\sqrt{s_{NN}} = 200$ GeV (left) and the ratio of the east and west $v_2$ measurements to the inclusive $v_2$ (right). . . . .	119
A.9 FVTXS event plane measurement with default correction and FVTX layer 2 of $v_2(p_T)$ with the for the $p+\text{Au}$ $\sqrt{s_{NN}} = 200$ GeV (left) and the ratio of the east and west $v_2$ measurements to the inclusive $v_2$ (right). . . . .	119
A.10 FVTXS event plane measurement with inverse $\phi$ weighting and FVTX layer 2 of $v_2(p_T)$ with the for the $p+\text{Au}$ $\sqrt{s_{NN}} = 200$ GeV (left) and the ratio of the east and west $v_2$ measurements to the inclusive $v_2$ (right). . . . .	119

A.11 FVTXS event plane measurement with analytic weighting and a 20% cut and FVTX layer 2 of $v_2(p_T)$ with the for the $p+\text{Au}$ $\sqrt{s_{NN}} = 200$ GeV (left) and the ratio of the east and west $v_2$ measurements to the inclusive $v_2$ (right). . . . .	120
A.12 FVTXS event plane measurement with inverse $\phi$ weighting and a 20% cut and FVTX layer 2 of $v_2(p_T)$ with the for the $p+\text{Au}$ $\sqrt{s_{NN}} = 200$ GeV (left) and the ratio of the east and west $v_2$ measurements to the inclusive $v_2$ (right). . . . .	120
A.13 FVTXS event plane measurement with default correction and FVTX layer 3 of $v_2(p_T)$ with the for the $p+\text{Au}$ $\sqrt{s_{NN}} = 200$ GeV (left) and the ratio of the east and west $v_2$ measurements to the inclusive $v_2$ (right). . . . .	120
A.14 FVTXS event plane measurement with inverse $\phi$ weighting and FVTX layer 3 of $v_2(p_T)$ with the for the $p+\text{Au}$ $\sqrt{s_{NN}} = 200$ GeV (left) and the ratio of the east and west $v_2$ measurements to the inclusive $v_2$ (right). . . . .	121
A.15 FVTXS event plane measurement with analytic weighting and a 20% cut and FVTX layer 3 of $v_2(p_T)$ with the for the $p+\text{Au}$ $\sqrt{s_{NN}} = 200$ GeV (left) and the ratio of the east and west $v_2$ measurements to the inclusive $v_2$ (right). . . . .	121
A.16 FVTXS event plane measurement with inverse $\phi$ weighting and a 20% cut and FVTX layer 3 of $v_2(p_T)$ with the for the $p+\text{Au}$ $\sqrt{s_{NN}} = 200$ GeV (left) and the ratio of the east and west $v_2$ measurements to the inclusive $v_2$ (right). . . . .	122
A.17 FVTXS event plane measurement with default correction and FVTX layer 4 of $v_2(p_T)$ with the for the $p+\text{Au}$ $\sqrt{s_{NN}} = 200$ GeV (left) and the ratio of the east and west $v_2$ measurements to the inclusive $v_2$ (right). . . . .	122
A.18 FVTXS event plane measurement with inverse $\phi$ weighting and FVTX layer 4 of $v_2(p_T)$ with the for the $p+\text{Au}$ $\sqrt{s_{NN}} = 200$ GeV (left) and the ratio of the east and west $v_2$ measurements to the inclusive $v_2$ (right). . . . .	122
A.19 FVTXS event plane measurement with analytic weighting and a 20% cut and FVTX layer 4 of $v_2(p_T)$ with the for the $p+\text{Au}$ $\sqrt{s_{NN}} = 200$ GeV (left) and the ratio of the east and west $v_2$ measurements to the inclusive $v_2$ (right). . . . .	123

A.20 FVTXS event plane measurement with inverse $\phi$ weighting and a 20% cut and FVTX layer 4 of $v_2(p_T)$ with the for the $p+\text{Au}$ $\sqrt{s_{NN}} = 200$ GeV (left) and the ratio of the east and west $v_2$ measurements to the inclusive $v_2$ (right). . . . .	123
A.21 BBCS event plane measurement with default correction and all BBC rings of $v_2(p_T)$ with the for the $p+\text{Au}$ $\sqrt{s_{NN}} = 200$ GeV (left) and the ratio of the east and west $v_2$ measurements to the inclusive $v_2$ (right). . . . .	123
A.22 BBCS event plane measurement with inverse charge correction and all BBC rings of $v_2(p_T)$ with the for the $p+\text{Au}$ $\sqrt{s_{NN}} = 200$ GeV (left) and the ratio of the east and west $v_2$ measurements to the inclusive $v_2$ (right). . . . .	124
A.23 BBCS event plane measurement with $p+p/p+\text{Au}$ ratio correction and all BBC rings of $v_2(p_T)$ with the for the $p+\text{Au}$ $\sqrt{s_{NN}} = 200$ GeV (left) and the ratio of the east and west $v_2$ measurements to the inclusive $v_2$ (right). . . . .	124
A.24 BBCS event plane measurement with default correction and BBC ring 1 of $v_2(p_T)$ with the for the $p+\text{Au}$ $\sqrt{s_{NN}} = 200$ GeV (left) and the ratio of the east and west $v_2$ measurements to the inclusive $v_2$ (right). . . . .	124
A.25 BBCS event plane measurement with inverse charge correction and BBC ring 1 of $v_2(p_T)$ with the for the $p+\text{Au}$ $\sqrt{s_{NN}} = 200$ GeV (left) and the ratio of the east and west $v_2$ measurements to the inclusive $v_2$ (right). . . . .	125
A.26 BBCS event plane measurement with $p+p/p+\text{Au}$ ratio correction and BBC ring 1 of $v_2(p_T)$ with the for the $p+\text{Au}$ $\sqrt{s_{NN}} = 200$ GeV (left) and the ratio of the east and west $v_2$ measurements to the inclusive $v_2$ (right). . . . .	126
A.27 BBCS event plane measurement with default correction and BBC ring 2 of $v_2(p_T)$ with the for the $p+\text{Au}$ $\sqrt{s_{NN}} = 200$ GeV (left) and the ratio of the east and west $v_2$ measurements to the inclusive $v_2$ (right). . . . .	126
A.28 BBCS event plane measurement with inverse charge correction and BBC ring 2 of $v_2(p_T)$ with the for the $p+\text{Au}$ $\sqrt{s_{NN}} = 200$ GeV (left) and the ratio of the east and west $v_2$ measurements to the inclusive $v_2$ (right). . . . .	126

A.29 BBCS event plane measurement with $p+p/p+\text{Au}$ ratio correction and BBC ring 2 of $v_2(p_T)$ with the for the $p+\text{Au}$ $\sqrt{s_{NN}} = 200$ GeV (left) and the ratio of the east and west $v_2$ measurements to the inclusive $v_2$ (right). . . . .	127
A.30 BBCS event plane measurement with default correction and BBC ring 3 of $v_2(p_T)$ with the for the $p+\text{Au}$ $\sqrt{s_{NN}} = 200$ GeV (left) and the ratio of the east and west $v_2$ measurements to the inclusive $v_2$ (right). . . . .	127
A.31 BBCS event plane measurement with inverse charge correction and BBC ring 3 of $v_2(p_T)$ with the for the $p+\text{Au}$ $\sqrt{s_{NN}} = 200$ GeV (left) and the ratio of the east and west $v_2$ measurements to the inclusive $v_2$ (right). . . . .	127
A.32 BBCS event plane measurement with $p+p/p+\text{Au}$ ratio correction and BBC ring 3 of $v_2(p_T)$ with the for the $p+\text{Au}$ $\sqrt{s_{NN}} = 200$ GeV (left) and the ratio of the east and west $v_2$ measurements to the inclusive $v_2$ (right). . . . .	128
A.33 BBCS event plane measurement with default correction and BBC ring 4 of $v_2(p_T)$ with the for the $p+\text{Au}$ $\sqrt{s_{NN}} = 200$ GeV (left) and the ratio of the east and west $v_2$ measurements to the inclusive $v_2$ (right). . . . .	129
A.34 BBCS event plane measurement with inverse charge correction and BBC ring 4 of $v_2(p_T)$ with the for the $p+\text{Au}$ $\sqrt{s_{NN}} = 200$ GeV (left) and the ratio of the east and west $v_2$ measurements to the inclusive $v_2$ (right). . . . .	129
A.35 BBCS event plane measurement with $p+p/p+\text{Au}$ ratio correction and BBC ring 4 of $v_2(p_T)$ with the for the $p+\text{Au}$ $\sqrt{s_{NN}} = 200$ GeV (left) and the ratio of the east and west $v_2$ measurements to the inclusive $v_2$ (right). . . . .	129
A.36 BBCS event plane measurement with default correction and BBC ring 5 of $v_2(p_T)$ with the for the $p+\text{Au}$ $\sqrt{s_{NN}} = 200$ GeV (left) and the ratio of the east and west $v_2$ measurements to the inclusive $v_2$ (right). . . . .	130
A.37 BBCS event plane measurement with inverse charge correction and BBC ring 5 of $v_2(p_T)$ with the for the $p+\text{Au}$ $\sqrt{s_{NN}} = 200$ GeV (left) and the ratio of the east and west $v_2$ measurements to the inclusive $v_2$ (right). . . . .	130



## Chapter 1

### Physics Overview

Due to the nature of discussing the thesis measurement in detail, a substantial number of acronyms and terms were used in this thesis. Although the acronyms and terms are defined in the text, a list of them is located in Appendix B.

In order to give the proper context for the measurement shown in this thesis, an overview of the physical theory relevant to the measurement is given in this chapter. We start with the SM (Standard Model of particle physics), narrow the focus down to QCD (Quantum Chromodynamics), and then narrow the focus even more to a specific state of matter governed by QCD known as the QGP (Quark Gluon Plasma). Properties of the QGP are discussed including energy loss and elliptic flow. A more comprehensive discussion on the topic of elliptic flow and small collision systems will be presented in Chapter 2.

#### 1.1 The Standard Model

The SM is the best understanding of the fundamental building blocks of reality and how they interact. The SM as we know it today has evolved over many years, including the unification of the electromagnetic and weak forces in the late 1960s [35]. The present day SM includes four fundamental forces, listed in Table 1.1, and the fundamental particles, listed in Figure 1.1.

The SM has the capability of making quantifiable predictions which have been shown to be in agreement with experimental measurements to high accuracy. The SM has endured decades of meticulous experimental testing without the need for major revisions, a notable exception being

Table 1.1: All four of the fundamental forces and the effective strengths of each relative to gravity. Gravity is not covered by the SM but is included for completeness.

Force	Current Theory	Relative Strength	Range [m]	Force Carriers
strong	Quantum Chromodynamics (QCD)	$10^{41}$	$10^{-15}$	gluon ( $g$ )
electromagnetic	Quantum Electrodynamics (QED)	$10^{38}$	$\infty$	photon ( $\gamma$ )
weak	Electroweak	$10^{25}$	$10^{-18}$	$Z^0, W^{+/-}$
gravity	General Relativity	1	$\infty$	graviton (hypothetical)

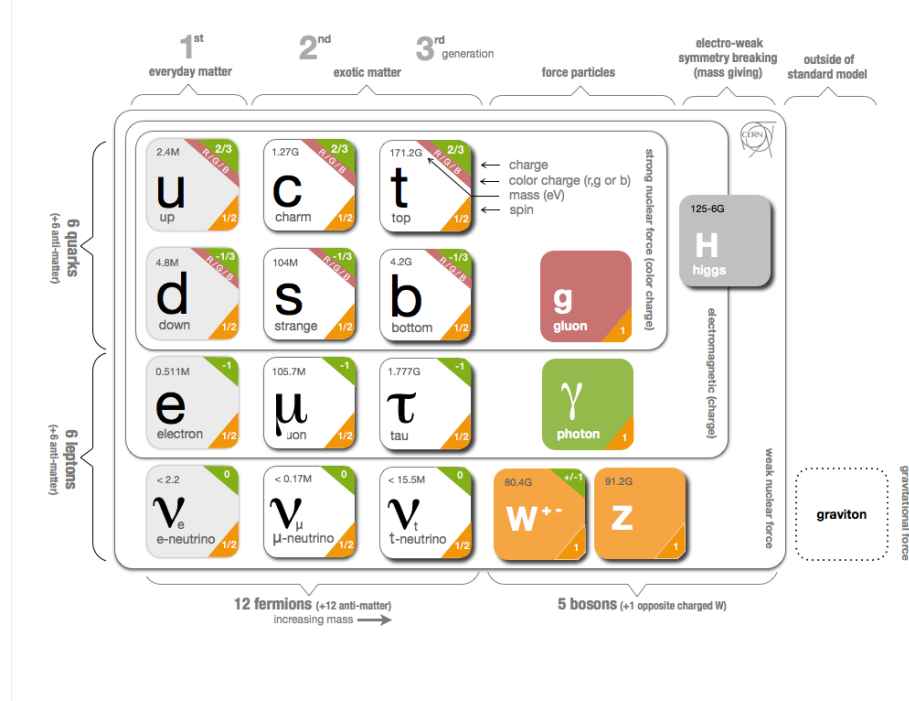


Figure 1.1: The fundamental particles of the SM arranged to highlight flavor (horizontal) and charge (vertical) patterns among the particles for the first three columns. The five particles on the right are the force carriers. All of these are thought to be the smallest discrete pieces of matter which make up everything else in the universe [5].

neutrino oscillations. The mathematical framework underpinning the SM is formally known as QFT (Quantum Field Theory), which combines the continuous nature of field physics with the discrete nature of quantum physics. The fundamental symmetries of the SM are given by the combination of the  $SU(3) \times SU(2) \times U(1)$  groups as defined in group theory. Each symmetry group represents the symmetry of each of the fundamental forces, in the SM such that  $SU(3)$ ,  $SU(2)$ , and  $U(1)$  represent the strong, weak, and electromagnetic forces respectively. As shown in Table 1.1, each of the fundamental forces has a quantized theory associated with it. The electromagnetic and weak

forces combine into a single theory at high-energy, known as the Electroweak Theory. No similar theory that has been experimentally verified has combined strong and electroweak as of the writing of this thesis.

Any given interaction described by the SM starts with an initial set of particles, a series of interactions between those particles (which is represented by an exchange of virtual particles), and then a set of final state output particles. Experimentally, the only information available to the experimenter is the set of input particles and output particles. The in-between step of the interaction of the particles is where QFT is used. Theoretical physicists use QFT to calculate the probabilities of each possible interaction diagram given a set of input particles or a set of output particles or both. To complicate things, there are infinite possible interaction diagrams for any given set of inputs and outputs; however, there are always leading diagrams which have the highest probability of occurring. Generally the simpler the interaction diagram, the higher the probability.

In order to make predictions about physical systems dominated by the strong force, like the heavy ion collision systems studied in this thesis, we turn to QCD.

### 1.1.1 Quantum Chromodynamics

Of the fundamental particles which make up the SM, the only ones which interact through the strong force are quarks and gluons. These particles have a unique quantum number named color charge, which can be one of three values, referred to as red (r), green (g), and blue (b), in an analogy to the three colors commonly used to form the basis of light in the visible spectrum. Like the electric charge in QED, each color has a negative value referred to as anti-red ( $\bar{r}$ ), anti-green ( $\bar{g}$ ), and anti-blue( $\bar{b}$ ), making six possible states for the quantum number in total. Gluons have two color charge quantum numbers, one charge and one anti-charge. This fact means gluons interact with themselves, which produces two important effects in QCD: confinement and asymptotic freedom.

In QED, electromagnetic fields decrease with distance away from a point charge. This functional form allows electromagnetically bound states to separate. However in QCD, the self interaction of the gluon means that as two quarks separate, the energy between them grows proportionally

to the distance between them. As a quark-antiquark ( $q\bar{q}$ ) pair separates, each quark in the pair has so much potential energy that quarks are pulled from the vacuum to bind to each quark to form two new pairs. The outcome of this effect is that solitary quarks can never be observed in a vacuum, by the time we try to observe them they will have found another particle in the vacuum with which to bind. This means that quarks are confined to zero color charge (or color neutral) bound states. Color neutral bound states are defined as a color and anti-color state (ex.  $r\bar{r}$ ,  $g\bar{g}$ ,  $b\bar{b}$ ), known as mesons, or a tricolor state (ex.  $rgb$  or  $\bar{r}\bar{g}\bar{b}$ ), known as baryons. The list of the two or three quarks that make up the color neutral bound state are known as valence quarks. Valence quarks determine the quantum number for the hadron, in contrast to sea quarks, which are  $q\bar{q}$  pairs made from gluon annihilation. Quarks and gluons found in hadrons are known as partons, and partons carry a fraction of the hadron's total momentum  $x$ . Partons can have any momentum fraction of the total momentum, but it is most probable that valence quarks have, on average, a large fraction of the total momentum whereas gluons and sea quarks are more likely to have a much smaller momentum fraction. Figure 1.2 shows the measured parton distribution functions in the proton, illustrating the difference of the average  $x$  for valence quarks in contrast to sea quarks.

Color neutrality can arise from other combinations of quarks; from combinations of quarks and gluons; or even arrangements of gluons with no valence quarks. The first mentioned combinations are theoretical color neutral states of four or more quarks, of which tetra and penta quarks have been observed [36]. The second and third mentioned combinations are known as exotic mesons or glueballs and there are experiments searching for their signatures.

Another related effect of the self-interaction of the gluon is known as the screening of bare color charges. Once again it is helpful to consider the familiar effects in QED. In QED, electrically charged pairs from the vacuum screen out the bare electric charge, causing the effective charge to decrease. This effect increases as the distance to the electric charge increases because there is a larger quantity of electrically charged pairs between the observer and the charge. Back to QCD,  $q\bar{q}$  pairs produce the same effect, providing a screening effect on the bare color charge, however short-lived the bare color charges are. Further complications arise when the color-carrying gluon

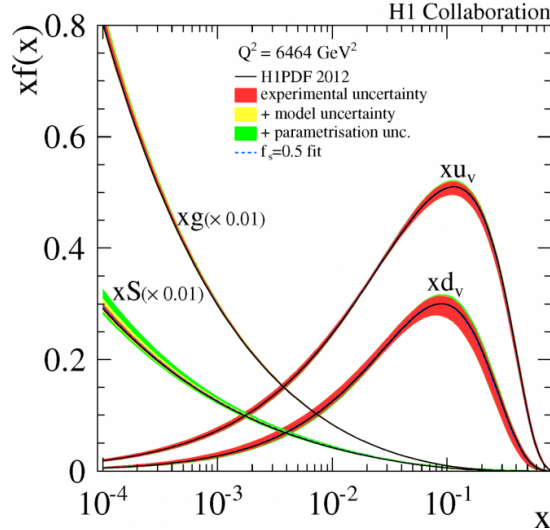


Figure 1.2: Parton distribution functions (PDF) of the momentum fraction  $x$  in the proton extracted from data taken by the H1 Collaboration. The curves  $xS$ ,  $xg$ ,  $xu_v$ , and  $xd_v$  correspond to PDFs of sea quarks, gluons, up valence quarks, and down valence quarks in the proton. The gluon  $g$  and sea  $S$  distributions are scaled by a factor 0.01. The uncertainties include experimental (inner) and model (middle) uncertainties and the parametrization variations (outer) [6].

in turn creates an anti-screening effect, which is the larger of the two effects. As one approaches a solitary color charge, the density of gluons becomes so large that the strong force counter-intuitively grows weaker. These screening effects alter the strong coupling constant known as  $\alpha_s$ ; Figure 1.3, which depicts the  $\alpha_s$  as a function of energy scale, shows the reduction of  $\alpha_s$  at large energies. This behavior is known as asymptotic freedom because the smaller  $\alpha_s$  is, the more quarks can move freely. Thus, there is an energy threshold such that the strong force is weak enough where perturbative calculations are valid which are carried out to orders in  $\alpha_s$ . The ability to make valid perturbative calculations for QCD is important for being able to make any in-depth QCD calculations of complex systems. Apart from perturbative QCD calculations, lattice QCD is a non-perturbative approach which is formulated on a lattice of space-time points. Although lattice QCD calculations are computationally complex, physical phenomena such as quark confinement can be treated numerically.

In addition to understanding the unique effects of QCD, understanding the phases of QCD matter is important. Figure 1.4 is a phase diagram for quark matter with temperature and net

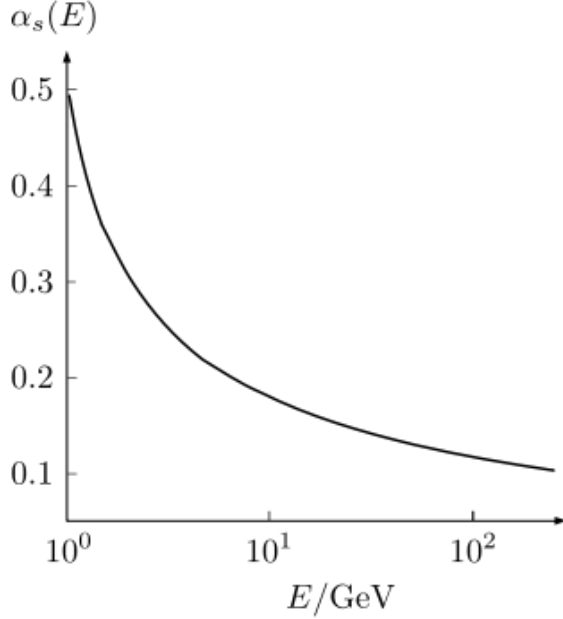


Figure 1.3: The strong coupling  $\alpha_s$  as a function of energy of the square root of the momentum transfer  $Q$  [7].

baryonic density on the axes. The type of quark matter that makes up the elements of normal matter is found in the figure under the heading of “Nuclear Matter,” which is the state of quarks and gluons for complex, relatively stable bound states known as nuclei. The “hadronic phase” indicates a state of quark matter where bound states of quarks form hadrons but those hadrons behave like a weakly coupled gas. At very large baryonic density, the “color superconductivity” phase is where the possible quantum states of quarks and gluons are so full that a neutron star is a possible example of such a state of matter. Finally, under extreme conditions of temperature and baryonic density, quarks may be deconfined and exist as solitary color charges in a plasma. This phase of matter, known as the QGP, provides a medium where screening effects are dominant and  $\alpha_s$  becomes small enough to allow quarks and gluons to move with relative freedom. Although the QGP has been observed by multiple experiments at RHIC (Relativistic Heavy Ion Collider) and LHC (Large Hadron Collider) facilities, the critical temperature at which the phase of quark matter is achieved is still unknown. One lattice QCD calculation estimates the temperature to be at 160–180 MeV or  $1.7\text{--}1.9 \times 10^{12}$  kelvin, which is much hotter than the center of our sun [37].

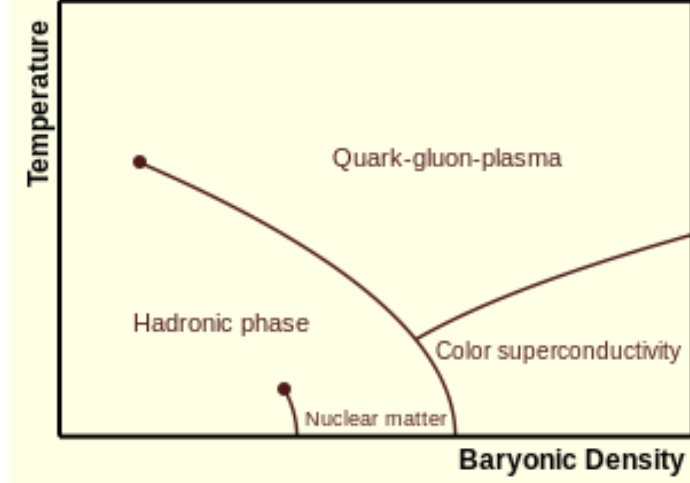


Figure 1.4: QCD phase diagram of temperature on the  $y$ -axis and net baryonic density on the  $x$ -axis [8].

Lattice QCD calculations have been done to examine the relationship of the number of massless degrees of freedom and the temperature of the medium, which provides insight to how the QGP and the early universe transition into normal matter. Figure 1.5 shows a curve of a quantity inversely proportional to the number of massless degrees of freedom. As the temperature drops, the less massive particles annihilate and disappear from the thermal universe, reducing the degrees of freedom. The points on Figure 1.6 are the numerical results from a lattice QCD calculation of the Equation of State (EoS). The  $y$ -axis for the points on this plot is the energy density divided by the temperature to the fourth power  $\frac{\epsilon}{T^4}$  which has been shown to be inversely proportional to the number of massless degrees of freedom [10]. It is noteworthy that the points increase around the transition at  $\sim 190$  MeV indicating the emergence of new degrees of freedom around the transition temperature of the medium.

## 1.2 Quark Gluon Plasma

The QGP is a new state of matter created in laboratories and is thought to be the same as the comprising the entire universe approximately one microsecond after the Big Bang [38]. Thus, studying the QGP and its properties in the laboratory can help cosmologists understand the

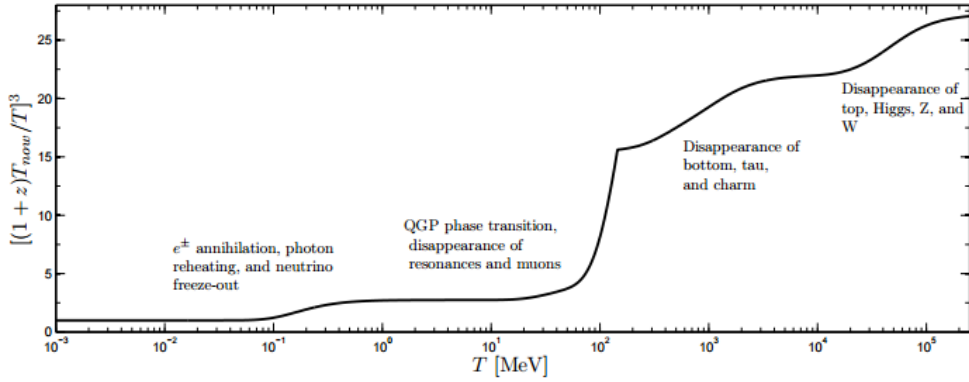


Figure 1.5: Disappearance of degrees of freedom through the evolution of the Universe in time and how this affects the fractional drop of temperature compared to red-shift [9].

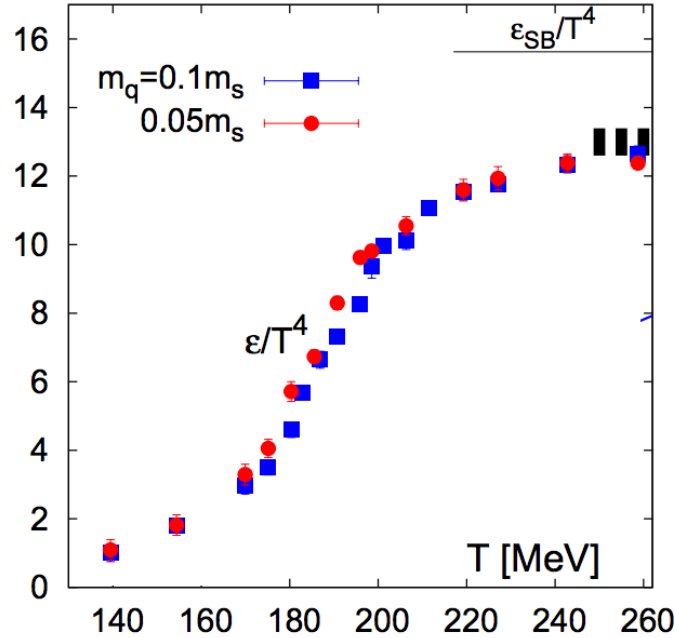


Figure 1.6: The energy density  $\epsilon$  divided by  $T^4$  vs temperature  $T$  at the physical value of the light quark mass [10].

state of the early universe.

The idea of hot hadronic matter was developed in the early 1950s by various physicists including Enrico Fermi [39]. This concept of applying statistical and hydrodynamical models to a strongly interacting particle ensemble ultimately evolved into the theory of the QGP. Since then,

systematic studies of hot hadronic matter systems have produced a greater understanding of the state of matter hypothesized to be the QGP and contributed to its approximate location on the nuclear matter phase diagram in Figure 1.4. Many unique properties about this new state of matter have been discovered: for example, the QGP behaves like a nearly perfect fluid and is opaque to color charges [40]. Enough research has been done to assemble a probable timeline of how the QGP evolves.

### 1.2.1 The QGP Evolution Timeline

The timeline overview of the QGP as made in the laboratory always begins with a high-energy collision (Au+Au for example), thus the QGP timeline is embedded in the laboratory timeline. The beginning of the QGP starts with initial state observable particles and ends with final state observable particles, although the final state particles may have been produced at different points during the QGP evolution. Although only lasting  $\sim 10^{-23}$  seconds or  $\sim 10$  fm/c, several distinct stages occur during this time period, and long after the evolution has ceased, the final state particles are detected in the experiment one quadrillion QGP lifetimes or one nanosecond later.

At the moment when heavy ions collide relativistically ( $\tau = 0$ ), they are length contracted down to flat disks in the lab frame, as seen in Figure 1.7. Then, the initial geometry resulting from the shape of the collision overlap region and fluctuations within the nuclei are transformed into the initial energy density of the medium ( $\tau \approx 1$  fm/c). At that moment, the hot hadronic matter is thought to be made up of deconfined quarks and gluons. The system then evolves hydrodynamically, expanding along the pressure gradients present in the initial energy density. At a certain point during this expansion, the medium has cooled enough to form baryons and mesons in a process called hadronization. It is important to note that the medium is still in thermal equilibrium at this point although it is no longer a QGP but instead a hadron gas. Once the medium has cooled down and expanded sufficiently, kinetic freeze-out occurs and the hadron gas becomes a group of particles which have ceased interacting ( $\tau \approx 10$  fm/c). It is this group of final state particles that can be detected much later. Although detectable particles escape the medium

at all times, the vast majority of particles detected are decoupled at kinetic freeze-out.

Even though all of these phases are of interest to the study of QGP, of particular interest to physicists is the thermal equilibrium phase when the QGP state is first achieved. It is during this phase where quarks are deconfined, the only phase where this occurs. In this environment, features of QCD can be studied, such as how color charges experience energy loss and to what degree collective behavior is observed.

As referred to in Figure 1.7, many types of particles are emitted during the QGP evolution, some of which are emitted before the kinetic freeze-out time. The most common type of particle produced from heavy ion collisions are baryons and mesons made of up, down, and strange quarks (pions, kaons, and nucleons), which are in abundant supply during and after the collision. Another particle produced from these collisions are photons. The QGP being an extremely hot ball of matter, blackbody radiation in the form of thermal photons are emitted and their spectrum can be used to estimate the temperature of the medium. These thermal photons escape the medium due to their lack of interaction with the strong force. Heavy quarks are produced primarily from initial hard parton-parton scatterings, “hard” meaning here that there is a large momentum transfer in the collision. These heavy quarks, such as bottom or charm quarks, often fragment into a shower of lower energy particles known as jets as they propagate through space.

### 1.2.2 Emergent Properties of the QGP

Now that the foundation of the QGP timeline has been established, properties of the medium can be discussed in context. Up to this point, the label of QGP has been applied to the state of matter produced from heavy ion collisions, but what evidence is there that this state of matter is a strongly coupled medium made of deconfined quarks and gluons?

Taking into account that the field of high-energy heavy ion collision physics is still evolving, several measured properties of this state of matter have come together to make the QGP the prevailing explanation. Among the best observations indicating QGP formation are particle energy loss and elliptic flow. The observation of hadrons at large  $p_T$  measured at much lower yields than

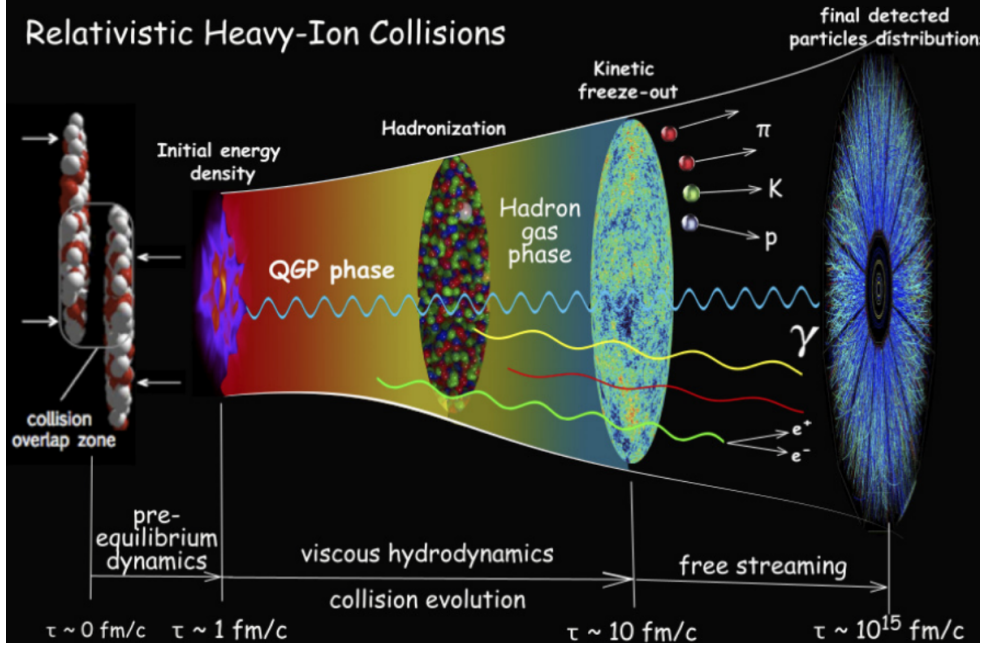


Figure 1.7: Relativistic heavy ion collision evolution timeline. Three distinct phases and their times are shown as well as the particles produced [11].

expected imply that the hadrons are experiencing energy loss when interacting with a strongly coupled medium. An elliptic symmetry in the angular distribution of final state particles when viewed with respect to the beam axis has been observed. The translation of initial geometry into long-range angular correlations indicates collectivity in a strongly coupled medium.

### 1.2.2.1 Particle Energy Loss

In order to study the new medium, it is useful to measure things about the QGP relative to a more well known collision system such as  $p+p$ . By measuring the relative number of hadrons produced at various transverse momentums in both  $p+p$  and heavy ion collisions, QGP medium effects can be teased out.

After the quarks are produced in  $p+p$  collisions, they will hadronize and freely travel to the experiment's detector. In heavy ion collisions, the quarks propagate through, and interact with, the QGP, exchanging energy and momentum with the medium along the way. The effect of energy loss on these quarks will modify their yield relative to the yield in  $p+p$  collisions. The nuclear

modification factor  $R_{AA}$  is the observable used to quantify this modification, which is defined for a given particle as:

$$R_{AA}(p_T) = \frac{dN_{A+A}/dp_T}{\langle N_{\text{coll}} \rangle \times dN_{p+p}/dp_T}, \quad (1.1)$$

where  $dN_{A+A}/dp_T$  and  $dN_{p+p}/dp_T$  are the yields of a given particle vs  $p_T$  (transverse momentum) in heavy ion collisions and  $p+p$  collisions, respectively, and  $\langle N_{\text{coll}} \rangle$  is the average number of binary collisions for a given class of events. In summary, the  $R_{AA}$  is a ratio for how many particles are produced for the same system with a normalization factor of  $\langle N_{\text{coll}} \rangle$  to account for the differences in system size. The  $\langle N_{\text{coll}} \rangle$  value is usually determined using Monte Carlo Glauber simulations and will be discussed in more detail in Chapter 2. If the particles do not interact with the medium, the  $R_{AA}$  should be equal to 1.0. A value above 1.0 is interpreted as an enhancement of particles and a value below 1.0 is interpreted as a suppression of particles.

Figure 1.8 shows a significant suppression in the  $R_{AA}$  vs  $p_T$  of  $\pi^0$  mesons produced in Au+Au collisions at  $\sqrt{s_{NN}} = 200$  GeV at RHIC for large and small sized QGP events, 0-10% centrality and 80–92% centrality events, respectively (centrality will be discussed in Chapter 2). This large suppression across all  $p_T$  of the  $\pi^0$  for central events as compared to peripheral events indicate energy loss of quarks due to the medium, which is consistent with a strongly coupled medium.

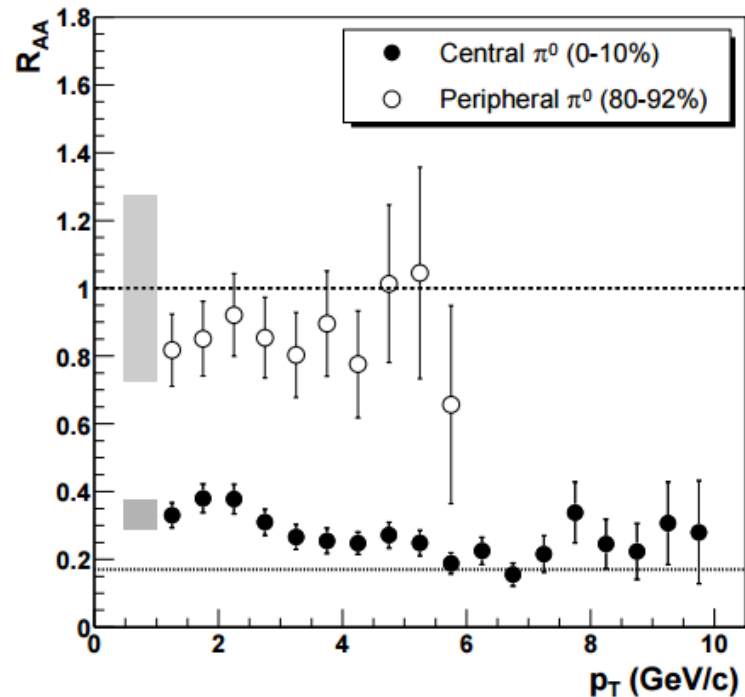


Figure 1.8: The  $R_{AA}$  vs  $p_T$  of  $\pi^0$  mesons produced in Au+Au collisions at  $\sqrt{s_{NN}} = 200$  GeV by PHENIX at RHIC for two different collision multiplicity classes [12].

### 1.2.2.2 Collective Flow and Azimuthal Anisotropy

Another signal of a strongly coupled medium is collective behavior amongst the constituent particles that make up the medium. By analyzing patterns in the spray of particles emitted from heavy ion collisions, systematic effects can be determined. Nominally there should be no preference in direction for final state particles from a heavy ion collision, the presence of such a preference indicates correlations among the particles in the medium, which can be measured by looking at the azimuthal anisotropy.

Consider the collision of two heavy nuclei as depicted in Figure 1.9. The overlap region between the two nuclei form an almond shaped region oriented to the plane of the initial collision geometry. After the collision the two nuclei remnants (the blue shapes) no longer participate and the yellow overlap region forms the QGP medium and starts to expand. This energy density distribution gives rise to a larger pressure gradient in the shorter direction. The larger the pressure gradient, the more momentum the particles will gain once the medium finishes evolving. This variation in the momentum of final state particles produces effects in the azimuthal (relative to the collision axis) distribution of particles. Therefore, by measuring the azimuthal anisotropy of the final state particles, long-range angular correlation like those present in Figure 1.9 can be measured. The initial state collision geometry being transformed into final state momentum anisotropy indicates collective behavior and elliptical flow of the particles.

In order to quantify the azimuthal anisotropy, the final state particle distribution is Fourier transformed:

$$C(\Delta\phi) \propto 1 + \sum_{n=1} 2c_n \cos(n\Delta\phi) \quad (1.2)$$

where  $C(\Delta\phi)$  is the correlation function defined by the distribution of the differences between the azimuth of particles from the event relative to other particles in the same event, and  $\sqrt{c_n} = v_n$  are flow coefficients. The flow coefficients  $v_n$  are proportional to the degree of anisotropy for each harmonic order  $n$ . A  $v_n$  of 0 would indicate there is no azimuthal anisotropy. More detailed information about the correlation function and other methods for quantifying the azimuthal

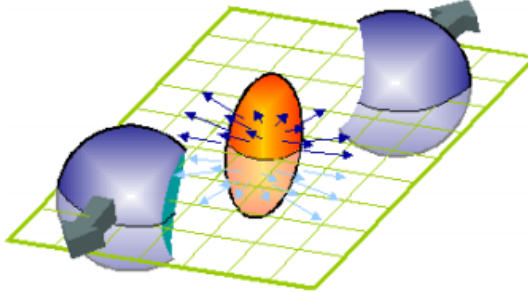


Figure 1.9: A diagram of a heavy ion collision. The blue shapes are the two colliding nuclei and the elliptical yellow shape is the collision overlap region which forms the medium. In the next instant of time the two nuclei would travel farther along the collision axis (into and out of the page) and the medium would expand along the direction of the arrows [13].

anisotropy are given in Chapter 2.

In addition to measuring the  $v_n$  for various systems, a relativistic hydrodynamic calculation can be compared to the data. Figure 1.10 shows  $v_n$  vs  $p_T$  for both RHIC and LHC energy heavy ion collisions for mid-peripheral events, such as those depicted in Figure 1.9. The very good agreement with hydrodynamic calculations curves suggests a medium which flows.

All of the discussion and results shown in this section have been referring to large collision systems such as Au+Au or Pb+Pb. Small collision systems such as  $p+A$ ,  $d+Au$ , or  $p+p$  were thought to be too small to produce a QGP, and thus were ideal as the control experiment to measure background effects of cold nuclei which may obscure the true signal of the QGP. However, recent results have shown that small collision systems show signs of QGP formation. Chapter 2 will delve into small collision system properties and measurements, as well as give a more in-depth discussion in calculating initial conditions and flow coefficients.

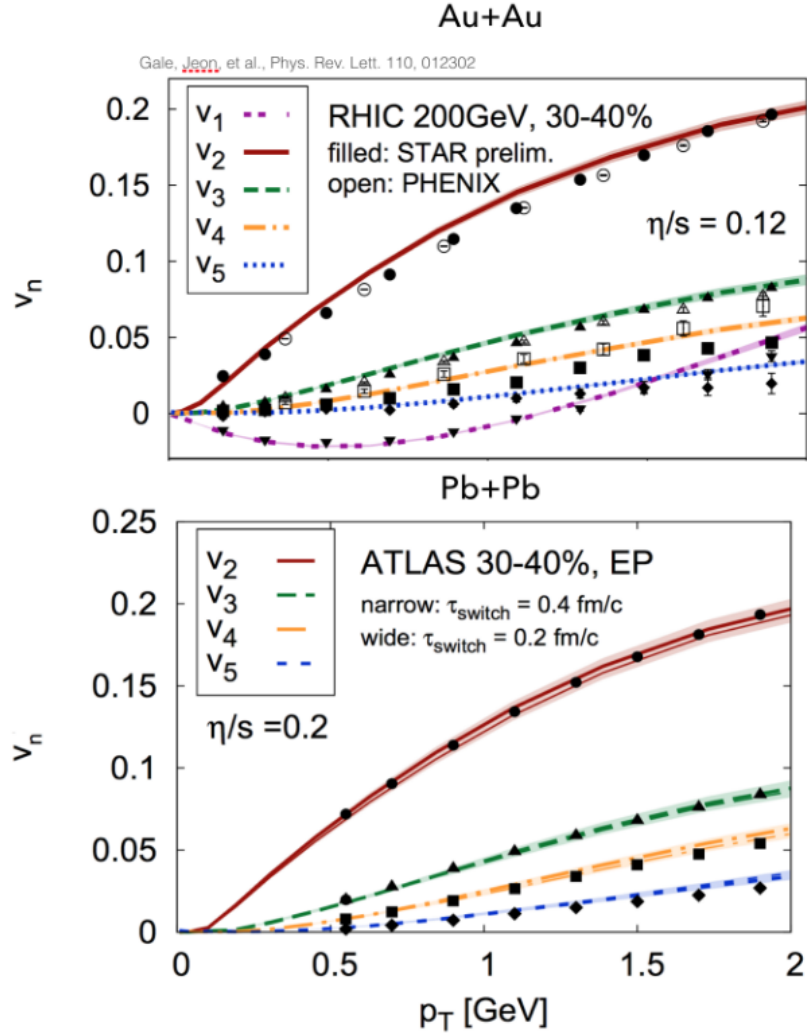


Figure 1.10:  $v_n$  vs  $p_T$  for RHIC Au+Au at  $\sqrt{s_{NN}} = 200$  GeV and for LHC Pb+Pb at  $\sqrt{s_{NN}} = 2.76$  TeV for mid-peripheral events for harmonic orders  $n$  up to five. The colored curves are the hydrodynamic calculations. The  $\eta/s$  is the viscosity parameter used in the calculations [14].

## Chapter 2

### Collectivity and Flow in QCD Systems

#### 2.1 A Conceptual Understanding of Collectivity and Flow

The observation of collectivity in matter can be a powerful indicator of fundamental properties in that matter. Collectivity means many discrete structures are interacting together to form a whole otherwise known as highly correlated behavior. In high energy heavy ion physics, a common interpretation of this behavior, although not the only interpretation<sup>1</sup> , is of a locally equilibrated medium with bulk properties instead of a group of individually weakly interacting constituent particles. In this case, the medium is a QGP and the bulk properties are that of a hydrodynamically described fluid: viscosity, density, temperature, etc. The term collectivity is often synonymous with the term hydrodynamic flow or simply “flow.” In this thesis, the terms will be used synonymously except in specific cases where the distinction is important.

It is important to note that although collectivity has a distinct signal, there are possible sources that can produce such a signal that do not involve collective behavior. These sources are called “non-flow” to differentiate them from sources of collectivity. When making measurements, non-flow must be taken into account as either a systematic uncertainty or as a systematic error correction. Sources of non-flow will be discussed more in Section 4.5.4.

To assist in the discussion of flow, we will briefly describe how it is measured. Generally, flow can be observed in heavy ion collisions by looking for long-range angular correlations between

---

<sup>1</sup> Although it is common to think of collectivity as hydrodynamic behavior, observations of collectivity do not necessarily imply any specific interpretation. Later we will discuss some alternative interpretations such as glasma correlations.

the spray of final state particles that come out of the collision. Long-range angular correlations in this case refers to correlations in particles with trajectories that have a large separation in pseudorapidity<sup>2</sup>  $\eta$ . When looking for correlations, this separation in  $\eta$  ensures that we are measuring something other than just local correlations, which are often due to non-flow.

Conceptually, the story of flow is that patterns in the initial conditions of the medium will be carried through the medium evolution and be observable in the final state particles. Figure 2.1 demonstrates the key events in the story: initial state geometry becomes transformed into a final state momentum anisotropy. The consideration of initial collision geometry will be a reoccurring theme when interpreting results in this thesis because the initial state geometry is one of the few independent variables over which we have experimental control.

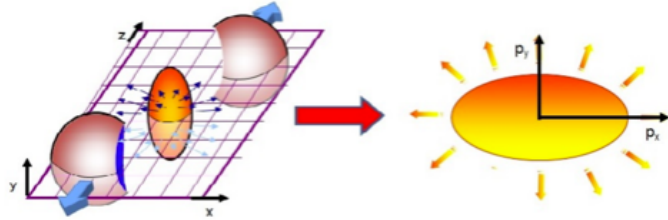


Figure 2.1: A diagram demonstrating the initial state geometry being transformed into the final state momentum anisotropy. The left depicts two spherical nuclei colliding parallel to the  $z$ -axis. The pair of nuclei leave behind an ellipsoidal shaped medium. This ellipsoid hydrodynamically evolves such that it expands along the steepest pressure gradient, which corresponds to the transverse direction. The right depicts the elliptical pattern present in the transverse momentum distribution of the final state particles after the medium has finished evolving [14].

### 2.1.1 Initial Conditions

Before proceeding to describing flow mathematically, it is useful to talk about the initial conditions of heavy ion collisions. When talking about collisions (also known as events) of circularly symmetric bodies, one of the most relevant parameters in characterizing collisions is known as the impact parameter. The impact parameter is the distance between the center of mass of each collision

<sup>2</sup> Pseudorapidity  $\eta$  is a commonly used variable in heavy ion physics which is related to the polar angle in spherical coordinates:  $\eta = -\ln [\tan (\frac{\theta}{2})]$ .

body; the larger the impact parameter, the more peripheral the collision. For heavy ion collisions, it is useful to consider peripheral collisions along with other types, as shown in Figure 2.2. The degree in which the colliding nuclei overlap is known as the “centrality.” A small value for centrality, for example 0-10%, corresponds to more central collisions, while a large value for centrality, for example 60-100%, corresponds to more peripheral collisions. The method for quantifying the event centrality is discussed in Chapter 3.

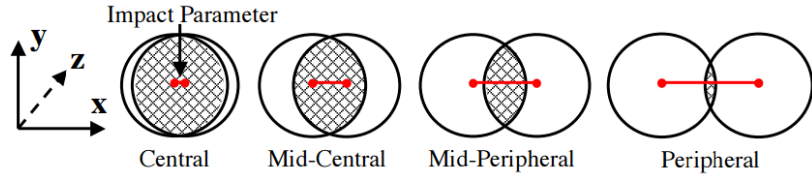


Figure 2.2: A diagram of the possible initial conditions of heavy ion collisions. The impact parameter is the red line. The language used in heavy ion physics is as follows: the larger the overlap between the colliding nuclei, the more central it is, the smaller the overlap, the more peripheral it is [15].

## 2.2 Mathematical Introduction to Measuring and Quantifying Flow

As discussed above, looking for long-range angular correlations is a way to measure flow. Measuring the azimuthal anisotropy is a way to quantify the extent of long-range angular correlation present in the medium evolution. Azimuthal anisotropy is the degree to which measured particles are non-uniform in the transverse plane. There are a number of ways to measure the azimuthal anisotropy. We will start by creating a correlation function.

### 2.2.1 Two-Particle Correlations

A correlation function is dependent on the difference in particles' trajectories, rather than the trajectories of the particles themselves. Let us consider the two-particle correlation function which uses pairs of particles from a collision event in order to create a correlation function. For each pair in an event, a  $\Delta\phi = \phi_1 - \phi_2$ , and a  $\Delta\eta = \eta_1 - \eta_2$ , value is obtained which makes up the

signal  $S(\Delta\phi, \Delta\eta)$  for a single event:

$$S(\Delta\phi, \Delta\eta) = \sum_{j=1}^{N_{\text{particles}}-1} \left( \sum_{i=j+1}^{N_{\text{particles}}} s(\phi_i - \phi_j, \eta_i - \eta_j) \right) = \sum_{k=1}^{N_{\text{pairs}}} s(\Delta\phi_k, \Delta\eta_k), \quad (2.1)$$

where  $s(\phi_i - \phi_j, \eta_i - \eta_j) = s(\Delta\phi_k, \Delta\eta_k)$  is a single pair in an event,  $N_{\text{particles}}$  is the number of particles in an event, and  $N_{\text{pairs}}$  is the number of combinatoric pairs in an event. This pair counting scheme ensures that no pair will be double counted and that a particle cannot form a pair with itself.

Ideally, this  $S(\Delta\phi, \Delta\eta)$  would be the correlation function; however, there are artificial correlations due to detector acceptance and other sources that distort this distribution. In order to correct for these effects, a mixed event background distribution  $M(\Delta\phi, \Delta\eta)$  is created, whereby pairs are produced by particles from two different events. The correlation function can be defined as follows:

$$C(\Delta\phi, \Delta\eta) = \frac{S(\Delta\phi, \Delta\eta)}{M(\Delta\phi, \Delta\eta)} \frac{N_{\text{pairs}}^{\text{Mixed}}}{N_{\text{pairs}}^{\text{Signal}}}, \quad (2.2)$$

where the correlation function normalization scheme used here is the ratio of the number of mixed pairs  $N_{\text{pairs}}^{\text{Mixed}}$  to signal pairs  $N_{\text{pairs}}^{\text{Signal}}$  in the event. Substantial variations in this  $C(\Delta\phi, \Delta\eta)$  are usually seen as long-range angular correlations, which can be attributed to collectivity.

In practice, correlation functions often combine particles from two different  $p_T$  ranges. The first  $p_T$  range corresponds to the “trigger” particles and the second range to the “associated” particles. In this scheme, the pair function is  $s(\phi_i^t - \phi_j^a, \eta_i^t - \eta_j^a)$  where the  $t$  superscript indicates trigger particles with a given  $p_T$  range and the  $a$  superscript indicates associated particles with a given  $p_T$  range.

Two examples of 2-D two-particle correlation functions; one for  $p+p$  at  $\sqrt{s} = 7$  TeV with no multiplicity selection, and one for Pb+Pb at  $\sqrt{s_{NN}} = 2.76$  TeV high multiplicity events are shown in Figure 2.3. The trigger and associated  $p_T$  ranges are given in the figure caption. Plotting the correlation function in terms of both  $\Delta\phi$  and  $\Delta\eta$  allows one to see the full extent and location of correlations for the collision system. These two correlations were selected to showcase the two

extremes of typical correlation functions.

An important feature in the left plot is the large strength of correlations at  $(\Delta\phi, \Delta\eta) = (0,0)$ , which is known as the nearside<sup>3</sup> “jet peak.” As mentioned in Chapter 1, jets are a spray of particles in a cone shape; therefore, the jet peak is at  $(0,0)$  because all the particles within the jet have a similar trajectory. The jet peak has been truncated in the figure. Another important feature is what is known as the “away-side ridge” located at  $\Delta\phi = \pi$  and extending very far in the  $\Delta\eta$  variable. This feature arises when back-to-back dijets are produced; all of the particles from one of the jets will be roughly  $\pi$  radians apart in trajectory with respect to the other jet and spread out in  $\Delta\eta$ . Apart from these main features which come from jets and dijets, there are no other major sources of correlations between particles for minimum bias  $p+p$  events, such that  $p+p$  events are taken to be the representation of the non-flow background. Minor sources of additional non-flow are in pure decays and Coulomb interactions. Thus, correlation function features present in regular  $p+p$  events are taken to be present at some level in the correlation function of every heavy ion collision system.

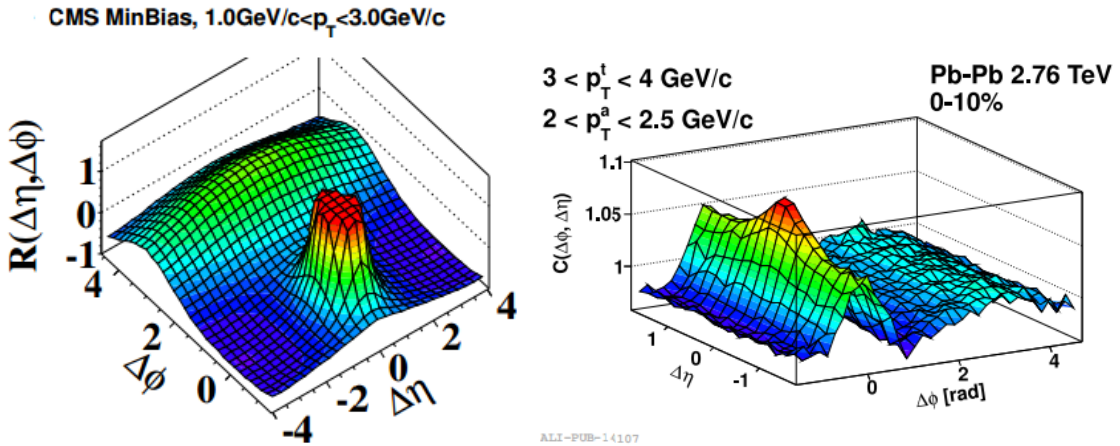


Figure 2.3: The left plot is 2-D two-particle correlation function for  $p+p$  collisions at  $\sqrt{s_{NN}} = 7$  TeV for hadrons with the same trigger and associated  $p_T$  range of  $1.0 \text{ GeV}/c < p_T < 3.0 \text{ GeV}/c$  for all events measured by CMS[16]. The left plot is 2-D two-particle correlation function for Pb+Pb collisions at  $\sqrt{s_{NN}} = 2.76 \text{ TeV}$  0-10% centrality events for trigger hadrons with  $3 < p_T^t < 4 \text{ GeV}/c$  and associated hadrons with  $2 < p_T^a < 2.5 \text{ GeV}/c$  measured by ALICE [17].

<sup>3</sup> For correlation functions,  $\Delta\phi \sim 0$  is known as “nearside” and  $\Delta\phi \sim \pi$  is known as “away-side.”

Conversely, the right panel of Figure 2.3 depicts the correlation function of high multiplicity Pb+Pb events, which exhibit characteristics of flow. While the non-flow features of the nearside jet peak and the away-side peak are present, a new feature known as the “nearside ridge” is approximately located at  $(\Delta\phi, \Delta\eta) = (0, |\Delta\eta| > 1.0)$ . This ridge exists in contrast to the lack of any correlations in the  $p+p$  correlation function at that location. It should be noted that the away-side jet ridge has also been modified. The nearside ridge and the away-side ridge modification are due to particles with long-range angular correlations. Thus, by quantifying the magnitude of these effects, the degree to which flow is present in the system can be measured.

### 2.2.2 Flow Harmonics

At this point, it is useful to narrow our focus to the region of the correlation function which has long-range angular correlations by taking a projection in  $\Delta\phi = |\phi_1 - \phi_2|$  away from the jet peak at  $\Delta\eta = 0$ . This 1-D two-particle correlation function slice contains the azimuthal anisotropy which should correspond to the degree of flow present in the system. Figure 2.4 depicts this correlation function  $C(\Delta\phi)$  for central Pb+Pb events. In order to quantify the azimuthal anisotropy,  $C(\Delta\phi)$  is cosine Fourier expanded:

$$C(\Delta\phi) \propto 1 + \sum_{n=1} \, 2c_n \cos(n[\Delta\phi]), \quad (2.3)$$

where  $v_n$  are known as flow coefficients or flow harmonics and  $n$  is the harmonic order [41]. The colored curves in Figure 2.4 are the first five components of the Fourier decomposition and their amplitudes show their relative strength. The green curve, which peaks at  $\Delta\phi = 0$  and  $\pi$ , corresponds to the second order harmonic, which is related to the second order flow coefficient  $v_2$ . The reason  $v_2$  is singled out is because it corresponds to elliptic flow and because it is the observable measured in this thesis. In order to extract  $v_2$  from this, one must calculate  $c_2$  defined as:

$$c_2^{t,a} = \langle \cos(2(\phi^t - \phi^a)) \rangle, \quad (2.4)$$

where  $\langle \rangle$  is defined as the average over all events and all particle pairs and where  $\phi^t$  and  $\phi^a$  are the azimuthal angles of the trigger and associated particles, respectively. If the trigger and associated

particles sets are the same then  $\sqrt{c_2} = v_2$ ; however, if the trigger and associated particle sets are not the same then  $c_2^{t,a} = v_2^t \times v_2^a$ , where  $v_2^t$  is the  $v_2$  for the set of trigger particles alone and the same with  $v_2^a$ . This ability to resolve  $c_2$  into the two distinct  $v_2$  components is only true if factorization [42] holds, which only occurs when the non-flow component of the measurement is small. This coefficient  $v_2$  directly characterizes the elliptic flow of the number of particles emitted along the direction of the steepest pressure gradient in the initial ellipsoid shown in Figure 2.1.

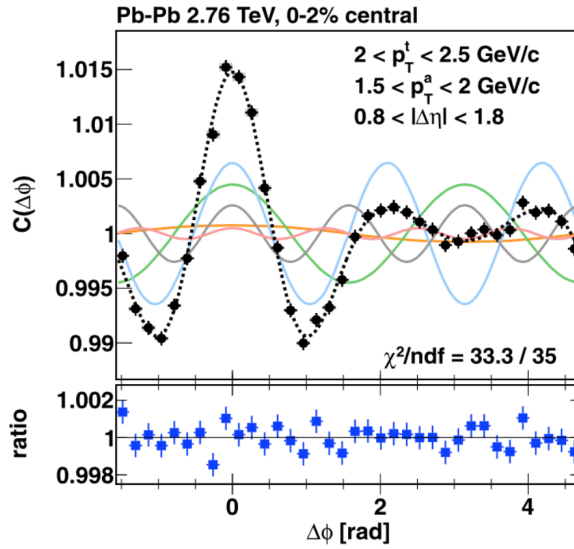


Figure 2.4: The 1-D correlation function in Pb+Pb at  $\sqrt{s_{NN}} = 2.76$  TeV for the most central events for trigger hadrons with  $2 < p_T^t < 2.5$  GeV/c and associated hadrons with  $1.5 \text{ GeV/c} < p_T^a < 2$  GeV/c. The 1-D two-particle correlation function is a projection in  $0.8 < |\Delta\eta| < 1.8$  from the 2-D correlation function, the 2-D correlation function being similar to that of the right panel of Figure 2.3. The black dotted points are the values of the correlation function and the colored lines are the first five cos Fourier decomposition components. The black dotted line is the sum of these five components [17].

### 2.2.3 Cumulants

Although two-particle correlations are useful, four-particle correlations or more can be used to better understand the flow measurement. In a multi-particle cumulant treatment,  $c_n\{k\}$  measures the  $n$ th harmonic from groups of  $k$  particles while explicitly subtracting correlations from  $< k$  particles. In this formulation, two-particle cumulants are treated the same way as in two-particle

correlation functions:

$$v_2\{2\} = \sqrt{c_2\{2\}} = \sqrt{\langle \cos[2(\phi_1 - \phi_2)] \rangle}, \quad (2.5)$$

whereas four-particle cumulants are defined as:

$$v_2\{4\} = (-c_2\{4\})^{1/4} = (2 \langle \cos[2(\phi_1 - \phi_2)] \rangle)^2 - \langle \cos[2(\phi_1 + \phi_2 - \phi_3 - \phi_4)] \rangle)^{1/4}, \quad (2.6)$$

where the term with four  $\phi$  indices corresponds to the four-particle correlation and the term with two  $\phi$  indices corresponds to the subtracted off two-particle correlation term. Multi-particle cumulants are well defined for larger groupings of particles,  $v_2\{6\}$ ,  $v_2\{8\}$ , and up. Comparing  $v_2$  measured by two and four-particle cumulants is useful when estimating the level of fluctuations present in the system, something which will be discussed more in Section 2.4.3.

#### 2.2.4 Event Plane Formulation

Another mathematical treatment for determining flow coefficients involves measuring a mathematical object known as an “event plane.” This is what is used in this analysis. Conceptually, the event plane method is an attempt to measure the participant plane angle, which defines the plane to which the orientation of the initial state collision geometry is aligned. Figure 2.5 is a geometric diagram defining the reaction plane angle  $\Psi_{PP}$ .

The event plane method uses final state particles to calculate the event plane angle from the data. A different event plane angle is defined for each harmonic, and is denoted as  $\Psi_n$  where  $n$  is the harmonic number. For an event with  $N$  particles, define the  $n$ th flow vector  $\vec{Q}^n$  as follows:

$$Q_x^n = \sum_{i=1}^N (w_i \cos(n\phi_i)) \quad (2.7)$$

$$Q_y^n = \sum_{i=1}^N (w_i \sin(n\phi_i)) \quad (2.8)$$

$$Q_w^n = \sum_{i=1}^N (w_i) \quad (2.9)$$

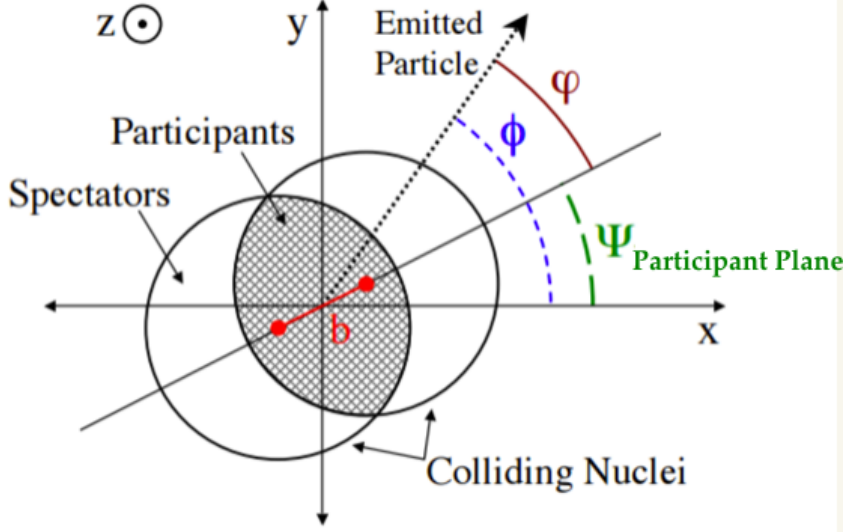


Figure 2.5: Diagram showing from the point of view of the beam of several variables used to characterize events. The spectators are the nucleons that do not participate in the collision, as opposed to the participants that do participate in the collision. The impact parameter is denoted as  $b$  and  $\Psi_{PP}$  is the reaction or participant plane angle.  $\phi$  is the standard azimuthal angle and  $\varphi = \phi - \Psi_{PP}$ . Adapted from [15].

where  $i$  is the  $i$ th particle in the event,  $\phi_i$  is the azimuthal angle of the particle,  $w_i$  is the weight factor, and  $n$  is the harmonic number. We define the  $n$ th order event plane as  $\Psi_n = \arctan\left(\frac{Q_y}{Q_x}\right)$ .

Once the event plane has been calculated, the flow harmonics ( $v_n$ ) are defined as

$$v_n = \frac{\langle\langle \cos(n(\phi - \Psi_n)) \rangle\rangle}{Res(\Psi_n)}, \quad (2.10)$$

where  $\langle\langle \rangle\rangle$  indicates that  $\cos(n(\phi - \Psi_n))$  is averaged over all particles in the same event, and the resulting  $v_n$  must be averaged over many events [43].

The event plane resolution is calculated using the standard 3-sub event method [43]. The strategy of this method is to measure  $\Psi_n$  with three different detectors in the same event, in order to better constrain the overall measurement of  $\Psi_n$ . The event plane resolution is defined as

$$Res(\Psi_n^A) = \sqrt{\frac{\langle\langle \cos(n(\Psi_n^A - \Psi_n^B)) \rangle\rangle \langle\langle \cos(n(\Psi_n^A - \Psi_n^C)) \rangle\rangle}{\langle\langle \cos(n(\Psi_n^B - \Psi_n^C)) \rangle\rangle}}, \quad (2.11)$$

where A, B, and C are three detectors measuring the same event. In this context, the term “sub-event” refers to the specific subset of particles measured by a given detector [41].

## 2.3 An Overview of Heavy Ion Collectivity Models

Throughout the discovery phase of the Quark Gluon Plasma and beyond into precision measurements, simulations based on theoretical descriptions of heavy ion collisions have been developed and have been successful in describing and predicting physics results. From the initial state of the colliding nuclei to the final state particles produced, every phase of heavy ion collisions is modeled. First the initial condition models will be discussed and then the medium evolution models will be discussed. It is necessary when calculating observables like  $v_n$  to choose an initial state model and a medium evolution model to chain together. The output of the initial state model will be the input to the medium evolution model; therefore, even if the medium evolution model describes the physics well, an initial state model that does not do so would cause the final  $v_n$  calculation to be inconsistent with the data.

### 2.3.1 Initial Condition Models

Initial condition models use a variety of methods to simulate the colliding nuclei. These models calculate quantities for characterizing initial collision conditions, such as the number of participating nucleons ( $N_{part}$ ), the impact parameter ( $b$ ), and the eccentricity ( $\varepsilon_n$ ). The  $N_{part}$  is the total number of neutrons and protons from the nuclei that suffer at least one inelastic collision, and is related to the size of the medium produced. The  $\varepsilon_n$  categorizes the  $n$ th order anisotropy in the initial collision geometry which is given by:

$$\varepsilon_n = \frac{\sqrt{\langle r^2 \cos(n\phi) \rangle^2 + \langle r^2 \sin(n\phi) \rangle^2}}{\langle r^2 \rangle} \quad (2.12)$$

where  $r$  is the radius of the participant nucleon, relative to the center of mass. This quantity is important because  $v_n \propto \varepsilon_n$  in the limit of ideal hydrodynamics [44].

A key part in simulating the initial conditions of heavy ion collisions is understanding event-to-event quantum fluctuations. One crucial source of fluctuations is the fluctuations of the nuclear wavefunctions where the distribution of nucleons within a nucleus fluctuates on an event-by-

event basis. The fluctuations of the nuclear wavefunctions are taken into account in all initial condition models. However, there are also fluctuations at the nucleon level such that the color charge distributions vary in each nucleon and for each event. These sources of fluctuations, combined with Lorentz contraction of the colliding nuclei, result in “lumpy” transverse distributions of color charge in each event. There are sophisticated models using the simple constituent quark model with the three color charge centers in the nucleon [32]. The degree of this event-by-event lumpiness is determined on average by the nuclear saturation scale  $Q_s$ , which corresponds to distances smaller than the size of the nucleon. QCD predicts event-by-event fluctuations in the multiplicities and the rapidities of gluon produced in the collisions [19].

### 2.3.1.1 Monte-Carlo Glauber

There are two main Glauber models: the so called “optical” Glauber model which assumes a smooth density described by a Fermi distribution in the transverse direction with respect to the collision axis; and the Monte Carlo-based Glauber model where individual nucleons are randomly distributed on an event basis and collision properties are determined by averaging over multiple events. The optical form of Glauber does not locate nucleons at specific spatial coordinates like the Monte Carlo form of Glauber. One benefit of the Monte Carlo Glauber (MC-Glauber) approach for quantities like  $N_{part}$  is its simplicity and ability to simultaneously simulate experimentally observable quantities, such as the charged particle multiplicity distribution.

The MC-Glauber model calculation is performed in two steps [45]:

- (1) the positions of the nucleon in each nucleus are randomly sampled from a probability distribution, which is described below,
- (2) the two nuclei are collided, with the assumption that the nucleons travel parallel to the beam axis (known as the Eikonal approximation), where each nucleon is labeled as being wounded (participating) or spectator.

The radial probability function, which is uniform in azimuthal and polar angles, is obtained

from nuclear color charge densities measured in low-energy electron scattering experiments [46].

The nuclear color charge density is described a Fermi distribution:

$$\rho(r) = \rho_0 \frac{1}{1 + e^{\frac{r-R}{a}}} \quad (2.13)$$

where  $\rho_0$  is the nucleon density,  $R$  is the radius of the nucleus, and  $a$  is the skin depth [45]. Equation 2.13 is normalized to produce the probability distribution. The impact parameter is determined randomly from a distribution  $dN/db \propto b$  up to some large maximum  $b \approx 2R$ .

The inelastic nucleon-nucleon cross section ( $\sigma_{NN}$ ), which is a function of the collision energy, is extracted from  $p+p$  collisions. At the RHIC energy of  $\sqrt{s_{NN}} = 200$  GeV,  $\sigma_{NN} = 42$  mb, and at the LHC energy of  $\sqrt{s_{NN}} = 2.76$  TeV,  $\sigma_{NN} = 72$  mb [18]. The ball diameter is defined as:

$$D = \sqrt{\frac{\sigma_{NN}}{\pi}}. \quad (2.14)$$

Two nucleons from the two nuclei are considered as collided if their separation in the transverse plane is less than the ball diameter. An example Au+Au collision event is show in Figure 2.6. MC-Glauber combined with negative binomial distributions is used to match the charged particle multiplicity distribution in order to map  $N_{part}$  to centrality classes. Details for this procedure are given in Section 3.2.9.

As stated earlier, an important initial condition quantity in simulating flow is the  $\varepsilon$  of the event. MC-Glauber simply calculates the moments of the participants themselves for each event. The eccentricity  $\varepsilon_2$  can be calculated along the axis of the participant distribution  $\varepsilon_2$ :

$$\varepsilon_2 = \frac{\sqrt{(\sigma_x^2 - \sigma_y^2)^2 + 4(\sigma_{xy}^2)^2}}{\sigma_x^2 - \sigma_y^2} \quad (2.15)$$

where  $\sigma_x^2$  and  $\sigma_y^2$  are the respective  $x$  and  $y$  positional variances for participating nucleons and  $\sigma_{xy}^2$  is the covariance of  $x$  and  $y$  for participating nucleons.

### 2.3.1.2 IP-Glasma

Another initial state model is known as IP-Glasma which uses the Color Glass Condensate (CGC) framework. CGC is a theory that describes high energy scattering in QCD as a many-

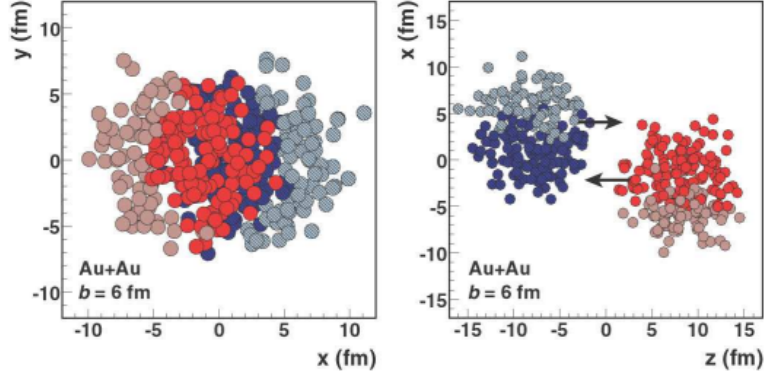


Figure 2.6: Glauber Monte Carlo event (Au+Au  $\sqrt{s_{NN}} = 200$  GeV with impact parameter  $b = 6$  fm) viewed in the transverse plane and along the beam axis in the left and right panels, respectively. The darker color disks correspond to the participating nucleons [18].

body system of weakly coupled partons that is non-perturbative because of the large quantity of partons [47]. This model calculates the initial conditions by incorporating the impact parameter dependent saturation model (IP-Sat) and the Classical Yang-Mills (CYM) description of Glasma. Glasma is formed when two sheets of CGC are collided at high energies. Calculating initial state dynamics as Glasma is thought to be an *ab initio* approach, although some of the parameters of the model are fixed by diffractive  $e+p$  Deep Inelastic Scattering (DIS) data [19]. The IP-Glasma computation starts by sampling the positions of the constituent nucleons from a Fermi distribution, the same way MC-Glauber begins. Then the saturation scale  $Q_{s,(p)}^2(x, b)$  is obtained from IP-Sat cross section for each nucleus, where  $b$  is the impact parameter relative to each participant nucleon's center. Once the saturation scale and the color charge density are obtained, random color charges are sampled from a transverse lattice [19].

A benefit of the IP-Glasma model is that it explicitly includes multiple types of quantum fluctuations, including fluctuations of color charges within the nucleons. It is useful to compare the calculations of IP-Glasma to MC-Glauber in order to gain a greater understanding of both.

### 2.3.1.3 Comparison between IP-Glasma and MC-Glauber

Figure 2.7 depicts the energy density distributions calculated by the IP-Glasma and MC-Glauber models. It is apparent from the “lumpiness” of both of these distributions that these models capture the complex internal structure of the nuclei at the moment of collision. However, the MC-Glauber distribution is much smoother than the IP-Glasma distribution due to the fact that the IP-Glasma distribution incorporates fluctuations at a much finer length-scale, given by  $1/Q_s(x)$ , which creates the spiky structures in the energy distribution. Apart from the differences in the length-scale of fluctuations between the models, MC-Glauber includes the energy distribution from every participant nucleon in the collision event, no matter how glancing its individual collision is, with the same parameters of width. Thus, the procedure of the MC-Glauber model for incorporating participating nucleons is less sophisticated than a model like IP-Glasma. Note that for MC-Glauber, the width of a nucleon’s energy density has been chosen to be 0.4 fm for all nucleons to match the MC-Glauber model to the data, despite the fact there are no *ab initio* calculations that derive such a number.

### 2.3.2 Medium Evolution Models

Once an energy density distribution is calculated from the initial condition models, it used as the input to a medium evolution model. The most commonly used medium evolution model is the relativistic hydrodynamic model.

#### 2.3.2.1 Hydrodynamic Modeling

In the context of heavy ion collisions, relativistic hydrodynamics is a macroscopic model used to simulate the evolution of a strongly coupled QGP medium. It is based on the foundational physical principles of conservation of momentum, energy, and net charge current which are written

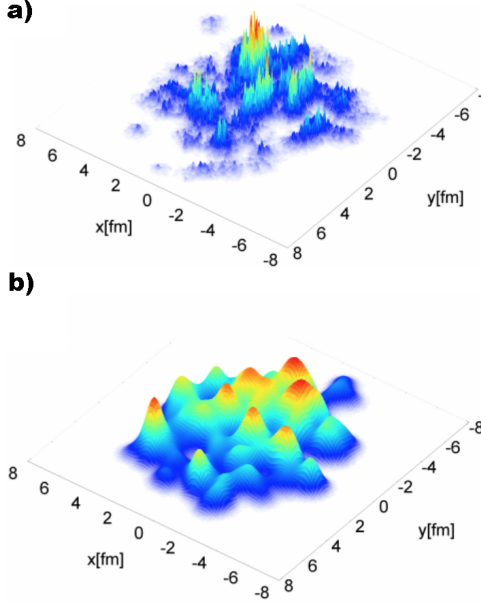


Figure 2.7: Initial energy density distributions (arbitrary units) in the transverse plane in two different heavy-ion collision events for IP-glasma (top) MC-Glauber (bottom) models [19].

as:

$$\partial_\mu T^{\mu\nu}(x) = 0, \quad (2.16)$$

$$\partial_\mu N^\mu(x) = 0, \quad (2.17)$$

where  $T^{\mu\nu}$  is the energy momentum tensor and  $N^\mu$  is the net baryon charge current. Ideal hydrodynamics requires that the medium is locally equilibrated, such that we have the perfect fluid energy momentum tensor as  $T^{\mu\nu} = (e+p)u^\mu u^\nu + pg^{\mu\nu}$  where  $e$  is the relativistic rest energy density,  $p$  is the fluid pressure,  $g^{\mu\nu}$  is a space-time metric, and  $u^\mu$  is the four-velocity of the fluid. Also, the charge current becomes  $N^\mu = n_0 u^\mu$  where  $n_0$  is the net baryon density. After asserting an equation of state (EoS)  $p = p(n_0, e)$ , the system is closed and the equations can be solved numerically.

Viscous hydrodynamics is similar to ideal hydrodynamics except that viscous hydrodynamics applies to a wider variety of systems, such as imperfectly locally equilibrated systems. In order to account for the lack of equilibrium, several new variables must be introduced:  $\pi^{\mu\nu}$  is the shear

stress tensor,  $\Pi$  is the bulk pressure,  $\eta$  is the shear viscosity,  $\zeta$  is the bulk viscosity,  $V^\mu$  is the baryon flow, and  $\tau_\pi$  and  $\tau_\Pi$  are the corresponding relaxation times. At RHIC and LHC energies, the net baryon density  $n_0$  is nearly zero and  $v^\mu$  is assumed to be zero. By choosing a proper EoS, an initial flow velocity, and an initial entropy/energy density at time  $\tau_0$ , the medium evolution can be simulated for time  $\tau > \tau_0$ . Note that in order to simulate very early stages of the QGP formation, modifications to this hydrodynamic formulation must account for pre-equilibrium conditions [48]. An example of a viscous hydrodynamic evolution is shown in Figure 2.8 for a collision of  ${}^3\text{He} + \text{Au}$ .

In order to relate the hydrodynamic simulation with observable particles distributions, the final state hadrons must be obtained. Purely hydrodynamic simulations emit hadrons directly from a decoupling surface of the fluid. The momentum distributions of the hadrons are calculated using the Cooper-Frye hadron cascade formula [49], which is followed by a resonance decay procedure to produce final state hadrons. This decoupling or freeze-out surface where the particles no longer interact can be defined by a constant temperature. The constant temperature of decoupling,  $T_{dec}$  is generally set to 150-170 MeV, depending on the hydrodynamic inputs [50].

To numerically simplify the hydrodynamic calculations, an exclusively longitudinal trajectory  $v_z = z/t$  along the beam axis (known as the Bjorken approximation) is assumed. This approximation corresponds to an invariance in longitudinal boosts and reduces the (3 spatial + 1 temporal) dimension hydrodynamics to (2 spatial + 1 temporal) dimension hydrodynamics. This approximation has shown that taking into account longitudinal variance minimally affects the flow calculations at mid-rapidity [48].

### 2.3.2.2 Hybrid Models: SONIC and superSONIC

Here we detail two specific hybrid models, noting that many viable hydrodynamic models have been developed [8]. A hybrid model combines the hydrodynamic calculations of the expanding QGP with a microscopic Boltzmann calculation of the medium. A Monte Carlo random sampler is used to convert the hydrodynamic output into individual hadrons which are then propagated via hadronic cascades.

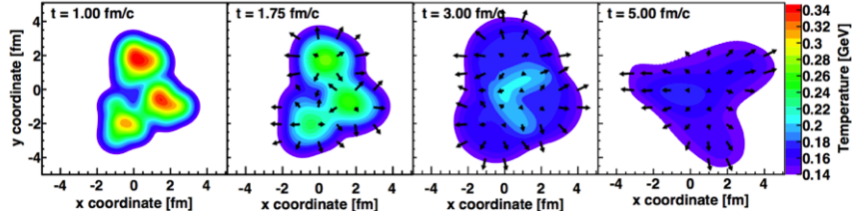


Figure 2.8: An example time evolution of a  ${}^3\text{He} + \text{Au}$  event from the initial state to final state. The color scale indicates the local temperature and the arrows are proportional to the velocity of the fluid cell from which the arrow originates [1].

The “Super hybrid mOdel simulatioN for relativistic heavy-Ion Collisions” (SONIC) combines pre-equilibrium dynamics with hydrodynamics [33] and a late-stage hadronic cascade [51]. In effect, SONIC has a small number of parameters, specifically those parametrizing the properties of the colliding nuclei, equation of states as input from lattice QCD, and shear and bulk viscosities in the QGP. As discussed when describing initial conditions models, fluctuations play a large role in determining the hydrodynamic flow. In order to study the effects of fluctuations in simulation, SONIC is an event-by-event simulation that is created by inputting fluctuating initial conditions, evolving each system separately, and then averaging the results.

SuperSONIC is the next generation of the SONIC model, differing from SONIC by incorporating pre-equilibrium dynamics with a calculation in the framework of the AdS/CFT correspondence [52]. The SONIC and superSONIC models agree well with the data within uncertainties.

### 2.3.3 AMPT

A Multi-Phase Transport (AMPT) model combines partonic and hadronic scattering in a single model. AMPT is the culmination of many models together. It is in an alternative to the hydrodynamic approach of medium evolution by using partonic strings instead of fluid cells as the building blocks of the model. The use of partonic strings preserves discrete particle information throughout the simulation. Despite the fact that AMPT is not a hydrodynamic model, it still is consistent with substantial flow coefficients, as will be shown in Chapter 5.

AMPT consists of four main components: the initial conditions, partonic interactions, the conversion from the partonic to the hadronic matter, and hadronic interactions. AMPT uses the Heavy Ion Jet Interaction Generator (HIJING) for producing the initial conditions, Zhang's Parton Cascade (ZPC) for simulating the scatterings of partons, the Lund parton string fragmentation model for hadronization, and A Relativistic Transport (ART) model for modeling the scatterings of hadrons. The HIJING model is used to convert the initial energy to produce hard scattered partons and soft strings, such that excited strings are converted to partons with string melting. Then ZPC is used to calculate the hard and soft scatterings between the partons. An implementation of the Lund string fragmentation modify the excited strings to hadrons. The ART model calculates the scatterings between the hadrons [53].

## 2.4 A Review of Flow Measurements in Small Collision Systems

As noted at the end of Chapter 1, small collision systems have long been considered too small to create hot and dense matter. These systems were utilized as control experiments which measure how the presence of a nucleus would effect the production of particles relative to  $p+p$  collisions. These so called “cold nuclear matter” (CNM) effects were isolated when colliding very low  $Z$  nuclei, such as a deuteron or proton, with a large nucleus.<sup>4</sup> Some generally accepted CNM effects are: gluon saturation, which is where a maximum is reached in the gluon density; and the Cronin effect, which is the broadening of the transverse momentum of emitted particles distribution due to multiple scatterings of initially colliding partons [54].

### 2.4.1 Nearside Ridge in Small Systems

In 2010, the CMS collaboration published a paper observing a nearside ridge in high multiplicity 7 TeV  $p+p$  events in the two-particle correlation function for dihadrons as shown in the left Figure 2.9. The aforementioned nearside ridge is located at  $\Delta\phi = 0$  and at  $|\Delta\eta| > 2$  in the figure.

---

<sup>4</sup> A side note: the convention in the field of heavy ion physics is to label any such small system collisions as  $p+A$  and any large system collisions as  $A+A$

The ridge is significant in the correlation function in high multiplicity  $p+p$  event in contrast to the correlation to any multiplicity  $p+p$  events at the same  $\sqrt{s}$ , as shown in Figure 2.9 (right).

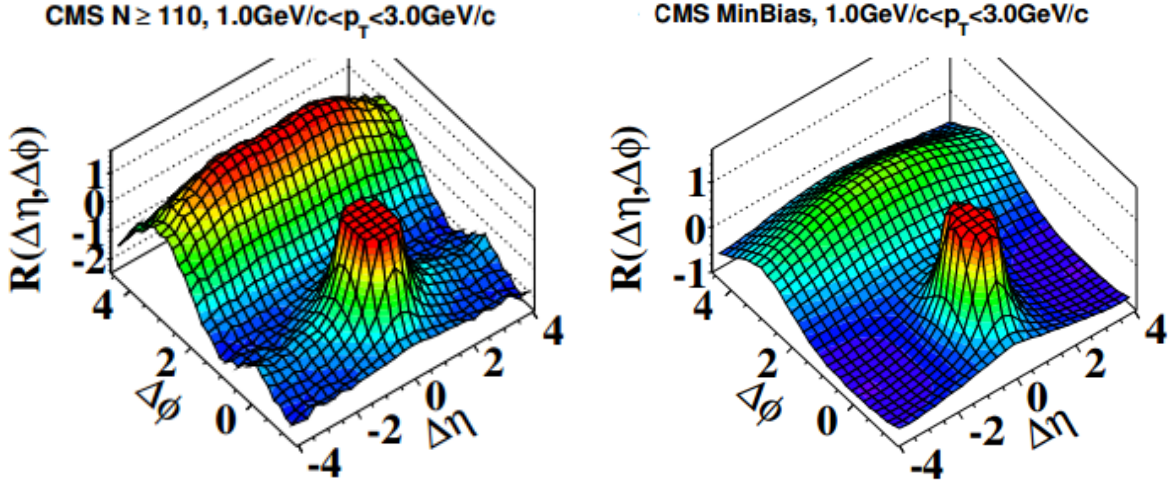


Figure 2.9: 2-D two-particle correlation function for  $p+p$  collisions at  $\sqrt{s} = 7$  TeV for hadrons with  $1.0 < p_T < 3.0$  GeV/c in high multiplicity events, with greater than 109 charged particles, and for any multiplicity of events are shown in the left and right panels, respectively [16].

What this discovery showed was that collectivity-like effects could be observed in small collision systems for high-multiplicity events. Thus,  $p+\text{Pb}$  at  $\sqrt{s_{NN}} = 5.02$  TeV events were also analyzed to find flow and a nearside ridge was observed in 0-20% central events. It became apparent over the course of making these measurements that the non-flow contribution to the signal would be much larger for  $p+p$  and  $p+A$  events than that of  $A+A$  events and so perhaps these were not related to flow. However, a procedure to reduce the non-flow component in the flow measurement is demonstrated in Figure 2.10. The procedure measures the same two-particle correlation functions for central and peripheral events, in this case 0-20% central and 60-100% central and then subtracts the central correlation function by the peripheral one. The assumption is that the level and shape of the non-flow is mostly consistent across centrality classes, whereas the flow is centrality dependent, such that there is virtually no flow in the peripheral correlation function. Thus, by subtracting the central correlation function by the peripheral, only the common components to both will be subtracted out, which are the non-flow components. As seen in panel three in Figure

2.10, the subtracted correlation function has no dominating jet peak at (0,0) and the nearside and awayside ridges are distinct and clear, with a signal dominated by elliptic flow [20].

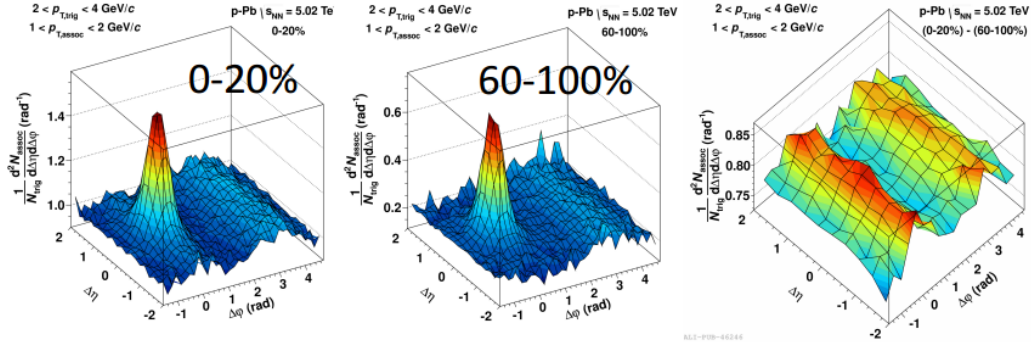


Figure 2.10: 2-D two-particle dihadron correlation function for  $p+Pb$  collisions for 0-20% and 60-100% centrality events as measured by the ALICE detector in the left and middle panel, respectively. The rightmost panel shows the subtraction of the left panel by the middle panel to remove non-flow effects [20].

#### 2.4.2 Mass Ordering in $v_2$

A key observation in the determination of collective flow is a mass ordering in the strength of the flow coefficients. This is due to a common velocity field in the fluid which then results in a larger momentum boost for heavier particles. The left panel of Figure 2.11 depicts the observed mass ordering of particles in  $Pb+Pb$  10-20% centrality events. In the low  $p_T$  region of 0–2 GeV, there is an ordering in the magnitude of  $v_2$  for hadrons:  $\pi^\pm > K^\pm > p+\bar{p}$  and so on for other heavier particles. The  $\pi^\pm v_2$  is the largest while the  $\pi^\pm$  mass is the smallest. Assuming an elliptic flow is present, the steep pressure gradients will efficiently modify the magnitude of  $p_T$  for heavy hadrons more than for light hadrons, leading to a reduction in the number of heavy hadrons available at low  $p_T$  to produce a low  $p_T v_2$  [55]. Thus, the mass ordering observation is taken to be evidence that the system is creating a medium such that particles will flow in predictable ways.

The right panel of Figure 2.11 shows a similar plot to the left panel of that figure except for the system  $p+Pb$   $\sqrt{s_{NN}} = 5.02$  TeV. As in the  $Pb+Pb$  system, the  $p+Pb$  dataset exhibits the

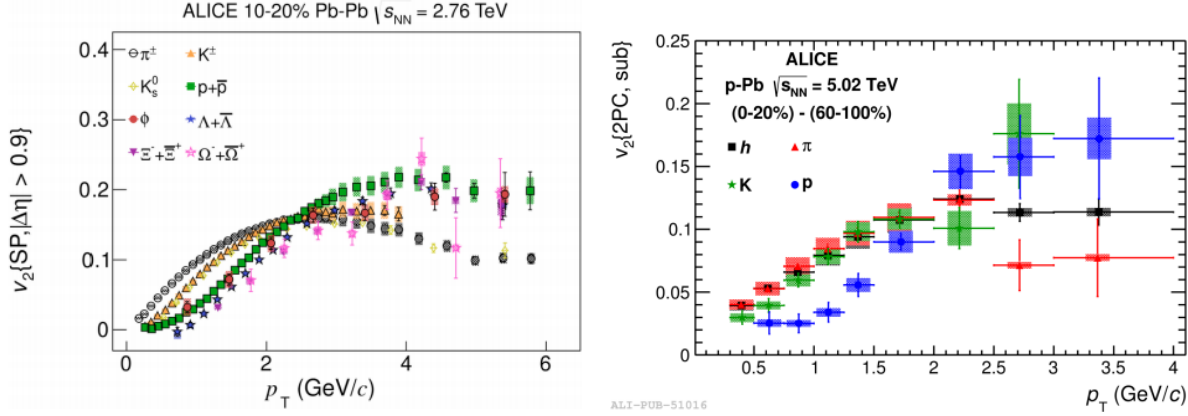


Figure 2.11:  $v_2(p_T)$  for different particles (see legend) in Pb-Pb  $\sqrt{s_{NN}} = 2.76$  TeV 10-20% events as measured by the ALICE detector (left) [21] and the  $v_2(p_T)$  for different particles (see legend) in p-Pb  $\sqrt{s_{NN}} = 5.02$  TeV for 0-20% events that were subtracted by peripheral 60-100% events (right) [20]. The  $\Delta\eta$  gap at minimum is 0.9 units. The  $v_2$  is extracted directly from the two particle correlation function shown in Figure 2.10.

same mass ordering, as well as similar shapes of each  $v_2(p_T)$  curve. Thus, the mass ordering effect that is observed in A+A is also observed in small systems, such as p+A. An important note for the result on the right panel is that a central minus peripheral subtraction was done, as demonstrated in Figure 2.10, whereas the result in the left panel needed no such peripheral subtraction. This means it is difficult to compare directly with the A+A result in magnitude, although the similarity of the ordering and the shape of the curves is enough of a comparison to indicate collectivity in the small system.

#### 2.4.3 Multi-Particle Cumulants and Fluctuations

The effects of event-to-event fluctuations in the elliptic flow measurement have been studied in small systems. In this context, fluctuations are differences in the initial collision geometry  $\varepsilon_2$  from one event to the next and so  $v_2$  is different from one event to the next. Fluctuations in  $\varepsilon_2$  can arise from fluctuations in the impact parameter within a centrality class of events and from fluctuations of the initial positions of the participant nucleons [56].

In order to better understand the effect of fluctuations in our small systems measurements,

$v_2$  was measured in different ways such as  $v_2\{2\}$  and  $v_2\{4\}$ , which are given by Equations 2.5 and 2.6, respectively. The quantity  $v_2\{2\}$  is the same as the two-particle correlation  $v_2$ , shown in Figure 2.11, while the quantity  $v_2\{4\}$  is a four-particle correlation. This paper referenced here [56], defines a fluctuation term similar in form to standard deviation that is related to flow coefficients defined:

$$\sigma_v^2 \equiv \langle v^2 \rangle - \langle v \rangle^2, \quad (2.18)$$

where  $v$  is the flow coefficient relative to the participant plane. This fluctuation term is related to  $v_2\{2\}$  and  $v_2\{4\}$  as

$$v\{2\}^2 = \langle v^2 \rangle = \langle v \rangle^2 + \sigma_v^2, \quad (2.19)$$

and

$$v\{4\}^2 = (2 \langle v^2 \rangle^2 - \langle v^4 \rangle)^{1/2} \approx \langle v \rangle^2 - \sigma_v^2. \quad (2.20)$$

Thus,  $v_2\{2\}$  measures the true elliptical flow plus fluctuations, whereas  $v_2\{4\}$  measures the true elliptical flow minus fluctuations. By measuring both  $v_2\{2\}$  and  $v_2\{4\}$  for the same dataset, an estimate of the size of the fluctuations can be obtained. The difference between the two and four particle cumulants should be  $\approx$  twice the size of the fluctuations.

Figure 2.12 shows the measurement of multi-particle cumulants in  $p+p$ ,  $p+\text{Pb}$ , and  $\text{Pb}+\text{Pb}$  by the CMS collaboration at the LHC [22]. A key part of this plot is noticing the significant difference between  $v_2\{2\}$  and  $v_2\{4\}$  in high multiplicity  $p+\text{Pb}$  and  $\text{Pb}+\text{Pb}$  events, indicating the presence of measured flow fluctuations and thus the expected geometry fluctuations. In the  $p+\text{Pb}$  and  $\text{Pb}+\text{Pb}$  there is an apparent multiplicity threshold, approximately around  $N_{trk}^{offline} = 75$ , below which a class of peripheral events have a different kind of behavior than the high multiplicity events.

It is also interesting to note that for both systems, the  $v_2\{4\}$ ,  $v_2\{6\}$ , and  $v_2\{8\}$ , are in excellent agreement. This excellent agreement indicates that  $p+\text{Pb}$  is similar to  $\text{Pb}+\text{Pb}$  in that it is an N-body correlation, not a two-body decay or back-to-back jets which produces correlations between smaller numbers of particles. There is also excellent agreement for  $p+p$ . Although these

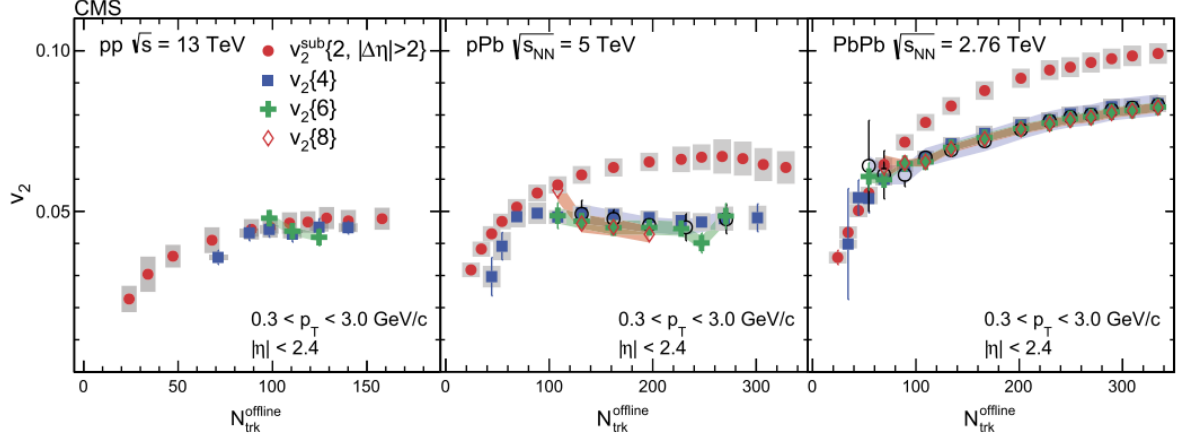


Figure 2.12: Elliptic flow measurements made using the 2nd, 4th, 6th, and 8th multi-particle cumulants, where the 2nd multi-particle is subtracted by peripheral events. Also the Lee Yang zero method non-flow elimination method is shown. These quantities are plotted vs the event multiplicity measured as  $N_{trk}^{offline}$ , which is the number of charged particle tracks observed during the offline analysis averaged over  $0.3 \text{ GeV}/c < p_T < 3.0 \text{ GeV}/c$  and over  $|\eta| < 2.4$ . The left panel is  $v_2^{sub}\{2, |\Delta\eta| > 2\}$ ,  $v_2\{4\}$ , and  $v_2\{6\}$  in  $p+p$  collisions at  $\sqrt{s} = 13 \text{ TeV}$ . The middle panel  $v_2^{sub}\{2, |\Delta\eta| > 2\}$ ,  $v_2\{4\}$ ,  $v_2\{6\}$ , and  $v_2\{8\}$ , in  $p+\text{Pb}$  at  $\sqrt{s_{NN}} = 5 \text{ TeV}$  collisions. The right panel is  $v_2^{sub}\{2, |\Delta\eta| > 2\}$ ,  $v_2\{4\}$ ,  $v_2\{6\}$ , and  $v_2\{8\}$  in  $\text{Pb}+\text{Pb}$  collisions at  $\sqrt{s_{NN}} = 2.76 \text{ TeV}$ . The error bars correspond to the statistical uncertainties, while the shaded regions correspond to the systematic uncertainties [22].

types of processes are present, all particles feel the effects of the initial geometry.

#### 2.4.4 Measurements Made at RHIC

Flow measurements in small systems have also been made at the lower energy accelerator, RHIC. Small collision systems,  $d+\text{Au}$ ,  ${}^3\text{He}+\text{Au}$ , and  $p+\text{Au}$  at  $\sqrt{s_{NN}} = 200 \text{ GeV}$  per nucleon were taken at RHIC in 2008, 2014, and 2015, respectively. The 2008  $d+\text{Au}$  dataset was intended to measure cold nuclear matter effects; however, RHIC experiments such as PHENIX had the capability to go back and measure  $v_2(p_T)$ . PHENIX was able to measure  $v_2$  for  $d+\text{Au}$  and for  ${}^3\text{He}+\text{Au}$  for the 0–5% most central events, as shown in Figure 2.13. A substantial  $v_2$  is observed for both  $d+\text{Au}$  and  ${}^3\text{He}+\text{Au}$  events with a strong  $p_T$  dependence, which is similar to that seen in  $p+\text{Pb}$  at the LHC. Instead of subtracting the non-flow component, as was done in Figure 2.10, the non-flow is incorporated as a systematic uncertainty. In addition to the  $v_2$  measurement, a substantial  $v_3$  is measured for the

${}^3\text{He}+\text{Au}$  dataset. This measurement is significant because the observation of more than one flow indicates the system is exhibiting complex behavior. A single flow harmonic could be explained by a variety of causes, whereas two flow harmonics from the same system narrow the range of possible explanations.

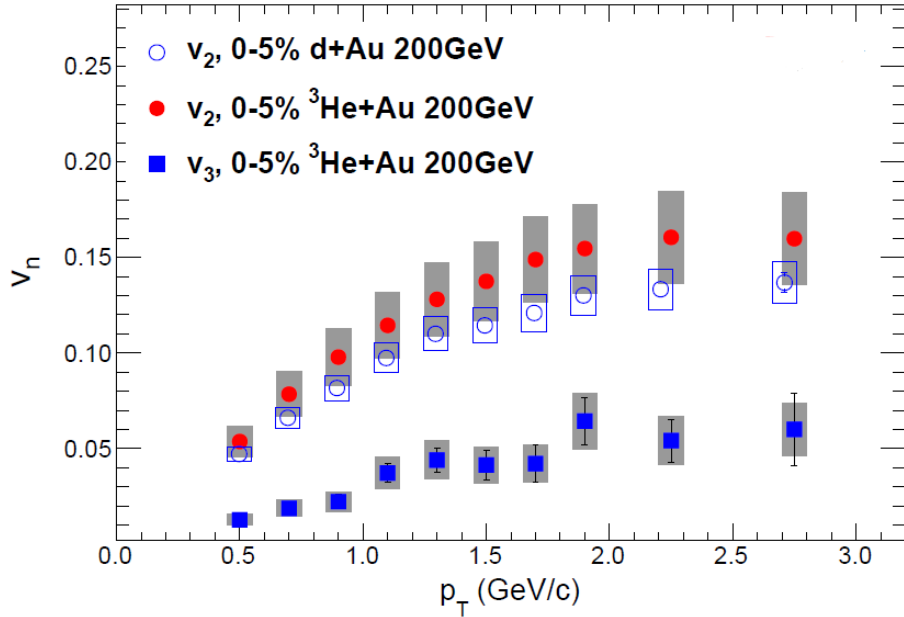


Figure 2.13:  $v_n(p_T)$  measured for  $d+\text{Au}$  and  ${}^3\text{He}+\text{Au}$  at  $\sqrt{s_{NN}} = 200$  GeV for 0-5% central events.  $v_2$  was measured for both systems and  $v_3$  was measured for  ${}^3\text{He}+\text{Au}$ . The grey boxes correspond to systematic uncertainties [23].

In addition to measuring the  $v_2(p_T)$  for all hadrons,  $v_2$  has been measured for  $\pi^\pm$  and  $p+\bar{p}$ , as seen in Figure 2.14. A very similar mass ordering in  $v_2(p_T)$  for different hadrons that was observed for  $p+\text{Pb}$  at  $\sqrt{s_{NN}} = 5.02$  TeV in Figure 2.11, was also observed for  $d+\text{Au}$  and  ${}^3\text{He}+\text{Au}$  at  $\sqrt{s_{NN}} = 200$  GeV. In the low  $p_T$  region,  $p_T < 1.5$  GeV/c, the  $v_2$  for  $\pi^\pm$  is greater than the  $v_2$  for  $p+\bar{p}$ . An interesting note here is that the low  $p_T$  region only goes up to 1.5 GeV/c, whereas the  $p+\text{Pb}$  dataset shows a low  $p_T$  mass ordering region of up to 2 GeV/c. The reason for this is probably due to the difference in center of mass energy, and larger radial flow at the higher energy.

It is necessary to note that throughout all of these measurements in small systems, a skepticism to the interpretation that the measurements are hydrodynamic flow has persisted. There are

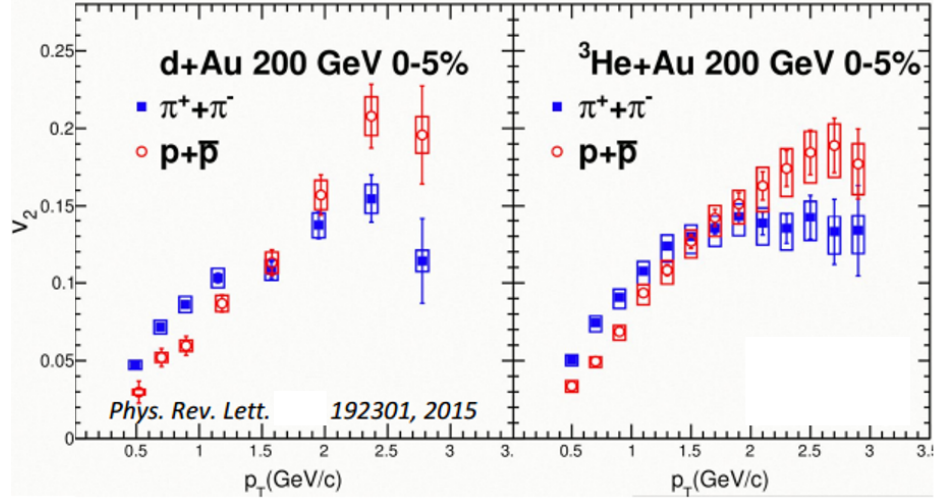


Figure 2.14:  $v_2(p_T)$  for  $d$ +Au and  ${}^3\text{He}+\text{Au}$  at  $\sqrt{s_{NN}} = 200$  GeV 0-5% centrality events for  $\pi^\pm$  and  $p+\bar{p}$  separately measured by PHENIX. The boxes correspond to the systematic uncertainty [23].

alternative explanations to the apparent flow measured in small systems that do not involve the creation of a medium. Examples of these alternative examples explanations include: initial state effects from glasma diagrams [57], color recombination [58], and partonic scattering in transport models [59]. In order to further the discussion on the distinction between a medium and a non-medium explanation, three different small collision systems, each with unique initial conditions, were run at RHIC. Those three systems are  $d$ +Au,  ${}^3\text{He}+\text{Au}$ , and finally  $p+\text{Au}$ , with intrinsic elliptical, triangular, and circular initial geometries. The constraints that a set of measurements from all three systems would place upon explanatory models would help distinguish which theory best describes small systems. This thesis is the completion of that set of three measurements, by measuring  $v_2$  in the  $p+\text{Au}$  dataset.

## Chapter 3

### Experiment Setup

#### 3.1 RHIC

The Relativistic Heavy Ion Collider (RHIC) is a superconducting charged hadron collider located at Brookhaven National Lab (BNL) in Upton, NY, United States. RHIC is capable of accelerating heavy ions such as Au (gold) or Cu (copper) nuclei to energies of  $\sim 100$  GeV per nucleon. RHIC is also capable of accelerating lighter ions such as protons, deuteron, and helium to  $\sim 100$  GeV per nucleon and  $\sim 250$  GeV per proton, in the case of  $p+p$ . The machine has demonstrated the ability to reliably create the QGP matter.

There are two major detector experiments currently operating in interaction regions around the RHIC ring: PHENIX (Pioneering High Energy Nuclear Interaction eXperiment) and STAR (Solenoidal Tracker at RHIC). Figure 3.1 shows the locations of the experiments and the accelerator chain. A typical schedule for RHIC is to operate the accelerator for 32 cryo-weeks every year in what is called a “Run.” There have been 16 Runs so far but the relevant Run for this thesis was the 15th Run taken in 2015 which ran proton colliding with gold ions ( $p+\text{Au}$ )  $\sqrt{s_{NN}} = 200$  GeV for part of its running. Specific details about this dataset are found in Section 3.2.8.

The RHIC ring is at the end of a chain of smaller accelerators that are used to “feed” the ions into the RHIC ring, where they are accelerated (or decelerated in some circumstances) to the desired collision energy. For heavy ions such as Au, the process of production and acceleration is listed in detail below [60].

- (1) A pulsed sputter Au ion source generates negative ions in the Tandem Van De Graaff.

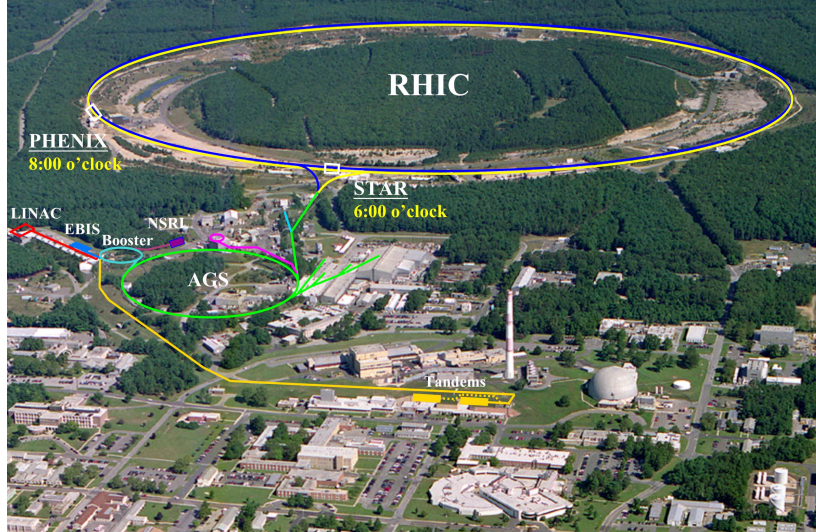


Figure 3.1: An aerial view of the accelerator chain in BNL starting at the Tandems (in gold) and ending at the RHIC ring (in blue and yellow for the two counter-circulating beams). STAR and PHENIX can be seen at two of the interaction regions. The ring is 2.38 miles in circumference [24].

- (2) The ions are passed through an electron stripping foil to achieve a positive  $+12 e$  charge and accelerated to  $\sim 1$  MeV per nucleon.
- (3) The ions pass through bending magnets and another foil to further strip electrons and filter charge, yielding a positive  $+32 e$  charge state.
- (4) The ions are sent to the Booster Synchrotron, which accelerates them to 95 MeV per nucleon and leaves them at a positive  $+77 e$  charge.
- (5) The ions enter the Alternating Gradient Synchrotron (AGS) in bunches of 24 around the ring. The ions are debunched and rebunched into four bunches and then accelerated to 10.8 GeV per nucleon.
- (6) The bunches then exit the AGS one at a time, where their Au ions are stripped of their two remaining electrons, yielding a final charge state of positive  $+79 e$ . Finally, the bunches are transferred to their respective buckets in RHIC.

For protons, the process instead begins at the Linear Accelerator (LINAC) facility. The

protons are then sent through the chain of accelerators in a similar way to the heavy ions until reaching RHIC in either a polarized or unpolarized spin state.

Once the ions have reached RHIC, they will enter one of two independent rings, blue or yellow, each circulating in an opposite direction. The ions in the rings are deflected and focused by 1,740 superconducting magnets using niobium-titanium conductors. Once the ions are focused and accelerated to the desired parameters around the RHIC, the ions are deflected into the six interaction regions where the blue and yellow rings intersect to produce collisions. It is at these interaction regions where the major experiments have set up their detectors, with STAR at the 6 o'clock position and PHENIX at the 8 o'clock position.

The period of time that collisions continue is known as a "fill," and the average length of a fill is eight hours. As the fill wears on, the collision rate substantially decreases as the density of ions in the machine decreases. Once the collision rate has been reduced sufficiently, it is more efficient to start the fill over at a higher collision rate.

### 3.2 PHENIX

PHENIX, the Pioneering High Energy Nuclear Interaction eXperiment, came online in 2000 along with RHIC and is located at the 8 o'clock interaction region along the RHIC ring. PHENIX is one of the two major RHIC experiments along with STAR, the Solenoidal Tracker At RHIC. The PHENIX detector philosophy differs from STAR in that PHENIX has a small acceptance but very good PID (particle identification) capabilities and very high rate capabilities.

PHENIX's detectors throughout the years include the Drift Chamber (DC), the Pad Chambers (PC), the Ring Imaging Cherenkov (RICH) Detector, the Hadron Blind Detector (HBD), the Time Expansion Chamber (TEC), the Time of Flight (TOF), the Electromagnetic Calorimeter (EMCAL), the Muon Tracker (MuTr), the Muon Identifier (MuID), the Muon Piston Calorimeter (MPC), the Muon Piston Calorimeter Extension (MPC-EX), the Beam-Beam Counter (BBC), the Zero Degree Calorimeter (ZDC), the Forward Calorimeter (FCAL), the Multiplicity and Vertex Detector (MVD), the Reaction Plane Detector (RPD), the Resistive Plate Chambers (RPC), the

Silicon Vertex Detector (VTX), and the Forward Silicon Vertex Detector (FVTX). Figure 3.2 depicts the approximate size and position of each of the detectors that are installed in PHENIX as of 2015.

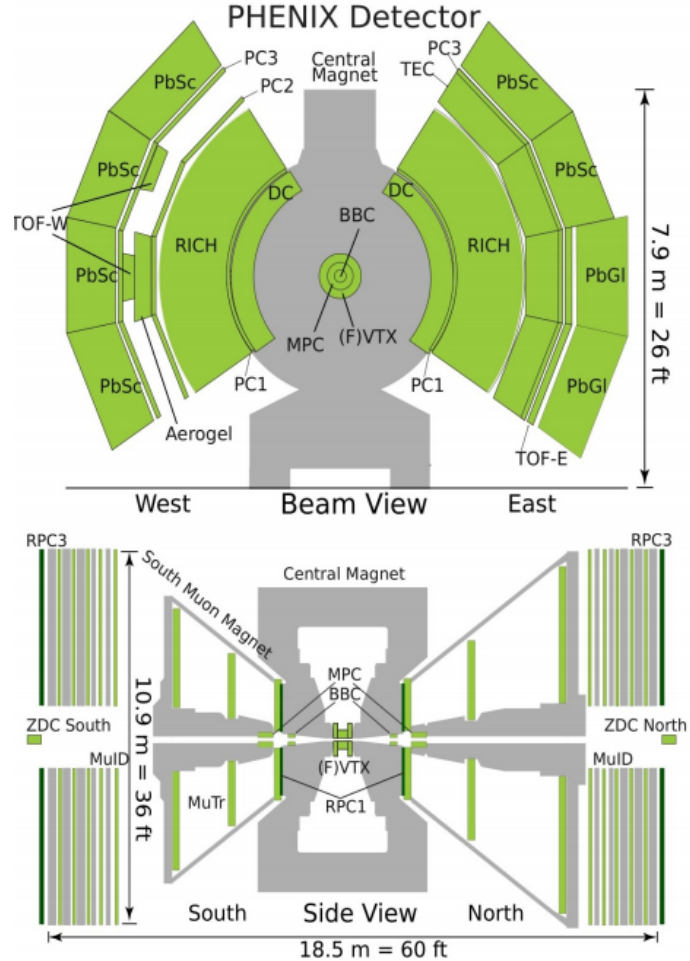


Figure 3.2: A cross-section diagram of the PHENIX detector from the incoming beam's perspective (top) and a cross-section diagram of the PHENIX detector from the side (bottom). The central arm detectors are not shown in the bottom diagram [25].

For this thesis, the relevant detectors in 2015 are the DC, PC, RICH, BBC, and FVTX. The DC, PC, and RICH are located in the mid-rapidity region relative to the collisions and are a part of what are referred to as the Central Arms (CA), and the BBC and FVTX are located in the forward (and backward) rapidity region relative to the collisions and are a part of what is referred to as the (Forward Arms) [27].

PHENIX makes use of the three powerful magnets in order to bend charged particles' trajectories: the Central Magnet (CM), the North Muon Magnet (MMN), and the South Muon Magnet (MMS).

PHENIX has a state-of-the art Data Acquisition System (DAQ) which is capable of writing 750 MB/s of information to disk. More details about the PHENIX DAQ are found in Section 3.2.7.

For reference, Figure 3.3 depicts the PHENIX coordinate system relative to the RHIC ring. References to the cardinal directions or  $x$ ,  $y$ , or  $z$  are defined in relation to this figure.

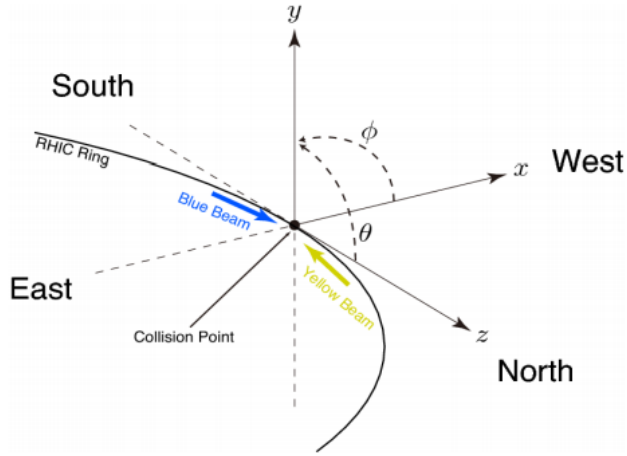


Figure 3.3: The PHENIX coordinate system. The origin is in the middle of the PHENIX detector at the collision point. North and south are parallel to the beam axis. East and west are transverse to the beam axis. Central detectors have a west and an east arm on either side of the beam. Forward detectors have a north and a south arm relative to the origin.

### 3.2.1 PHENIX Magnet System

The CM has two circular coils which can be configured in the same direction ( $++$  or  $--$ ), the opposite direction ( $+-$  or  $-+$ ), or with the inner magnet off ( $+0$  or  $-0$ ). The magnets can also be run in the “zero-field” configuration for alignment purposes. Figure 3.4 shows the magnetic field lines and strength produced by the PHENIX magnets. The magnetic field lines at mid-rapidity,  $|Z| < 0.3\text{m}$  on the plot, have a peak strength of  $\sim 0.9\text{ T}$  near the beam pipe and extend out to  $R \approx 2\text{ m}$ , just before the DC. The right panel of Figure 3.4 depicts the magnetic field strength as a

function of distance from the center of PHENIX. For any of the possible CM magnet configurations, the magnetic field strength is very small for  $r > 2$  m.

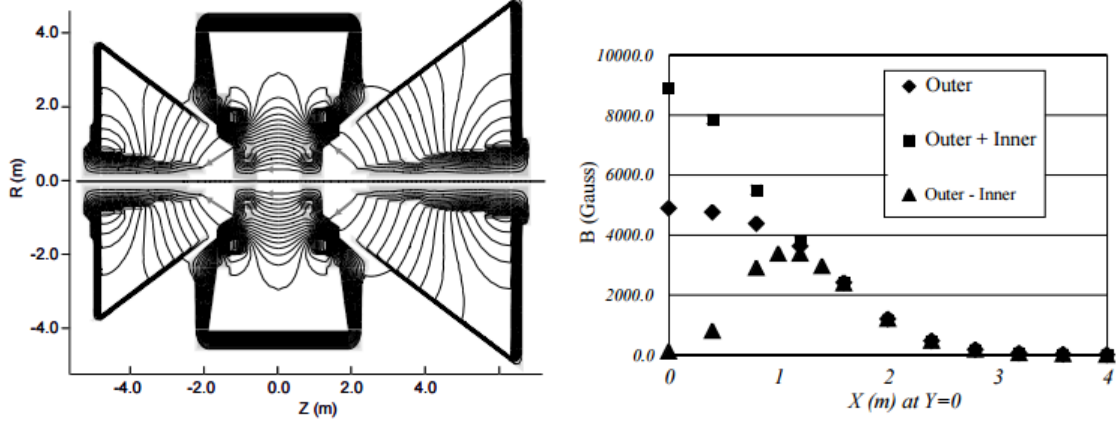


Figure 3.4: PHENIX magnetic field lines from the MMS, CM, and MMN, (left) and the total magnetic field strength from the CM vs the radial distance from the center of PHENIX at  $\phi = 0$ (right) [26].

### 3.2.2 Beam Beam Counter

The BBC is a forward detector used to determine the event start time, vertex, centrality, and event plane. The BBC is composed of two mirror image arrays, a South and a North Arm, that surround the beam pipe 144 cm on opposite sides of the nominal collision point just behind the Central Magnet, covering  $3.0 < |\eta| < 3.9$  and  $2\pi$  radians in azimuth. Each BBC arm is made of 64 elements composed of a 3-cm quartz Cherenkov radiator connected to a 2.5 cm diameter Hamamatsu R6178 mesh dynode PMT (photomultiplier tube), as shown in Figure 3.5. The outer and inner diameters of the BBC, with respect to the beam axis, are 30 cm and 10 cm, respectively.

The BBC is used to mark the event start time for the entire PHENIX detector by averaging the emitted particles arrival time at each BBC arm. The timing difference between each arm provides an estimate of the collision's z-vertex by

$$z = c \frac{T_S - T_N}{2}, \quad (3.1)$$

where  $T_S, T_N$  are the particle's average arrival times for each arm and  $c$  is the speed of light.

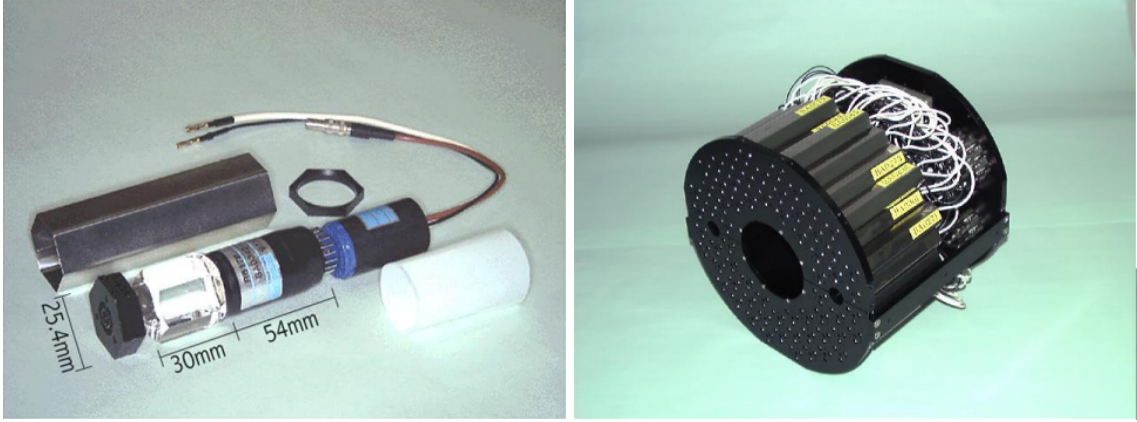


Figure 3.5: Photographs of the BBC detector. The left is of a single detector element consisting of a quartz radiator and a PMT. The right is of one of the BBC arms, consisting of 64 detector elements [27].

For  $p$ +Au collisions at  $\sqrt{s_{NN}} = 200$  GeV, the BBC has a timing resolution of  $\sigma_t \sim 50$  ps and a corresponding  $z$ -vertex resolution of  $\sim 1.0$ – $2.0$  cm, depending on the event charged particle multiplicity. A coarser estimate of the vertex is used during triggering, to select events of interest. Specific details about triggers are in Section 3.2.7.

The BBC also provides the centrality classification, as described in Section 2.1.1, of a collision event in PHENIX. Details of how BBC data is used to compute the centrality are given in Section 3.2.9.

Additionally, the BBC is used to calculate the event plane in the event, which is described in Section 4.2.

### 3.2.3 Forward Vertex Detector

The FVTX is a PHENIX detector upgrade that became operational in 2012. The FVTX provides charged particle tracking, collision vertex determination, and event plane determination [25]. The FVTX consists of two identical endcaps covering a combined pseudorapidity range of  $1 < |\eta| < 3$  and full azimuth coverage. Each endcap has four stations of silicon mini-strip sensors with a pitch of  $75 \mu\text{m}$  arranged in the radial direction around the beam pipe. The basic unit of construction is a wedge that has silicon strip sensors and associated read-out chips. The inner most

layer (on each side) of the FVTX has a smaller radius. Figure 3.6 is a photograph of the FVTX disks and an engineering drawing of the FVTX and its support structure. The FVTX is used in this thesis to calculate the event plane, as discussed in Section 4.2.

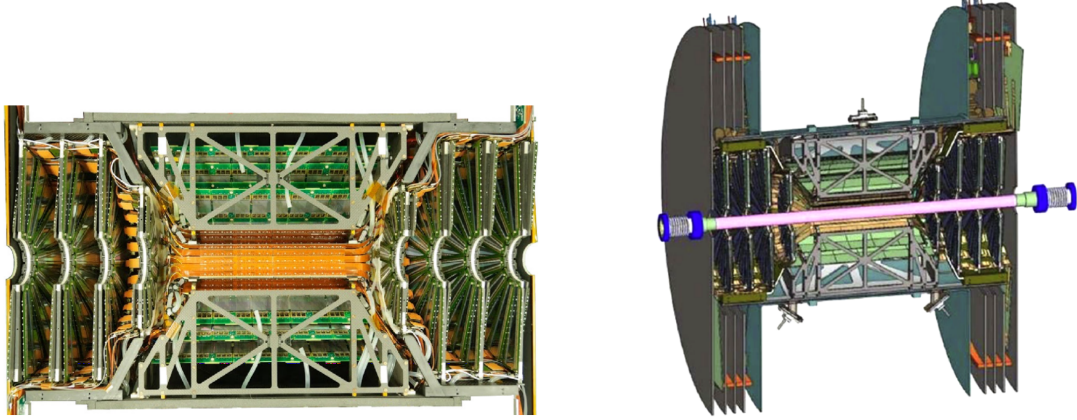


Figure 3.6: A photograph of half of the FVTX. In the cutaway, one sees the half disks on either end of the picture (left) and a schematic of the FVTX at a slightly different angle (right). The FVTX is only 20 cm in the  $z$  direction from the PHENIX coordinate system origin (the center of each picture) [25].

### 3.2.4 Drift Chamber

The DC covers an pseudorapidity acceptance of  $|\eta| < 0.35$  and is composed of two gas multi-wire proportional chambers in each of the central arms. The DC is used to measure particle trajectories in the  $r\phi$  plane and their momentum. The DC is located  $\sim 2$  m from the  $z$ -axis, placing it in a very small residual magnetic field from the CM. Apart from the VTX, the DC is the first detector encountered by a particle produced at mid-rapidity.

As a charged particle passes through the DC volume, a gas mixture of 50% Ethane and 50% Argon are ionized to create free electrons. These electrons cause a chain reaction of ionizations which are measured by an anode wire. The DC is designed in such a way that the drift velocities of the electrons are predictable enough to relate time and position together.

Each of the two identical DC arm is cylindrical design and covers 2.5 m along the beam direction and is 0.4 m deep (in radius) as seen in the left panel in Figure 3.7. Each arm is divided

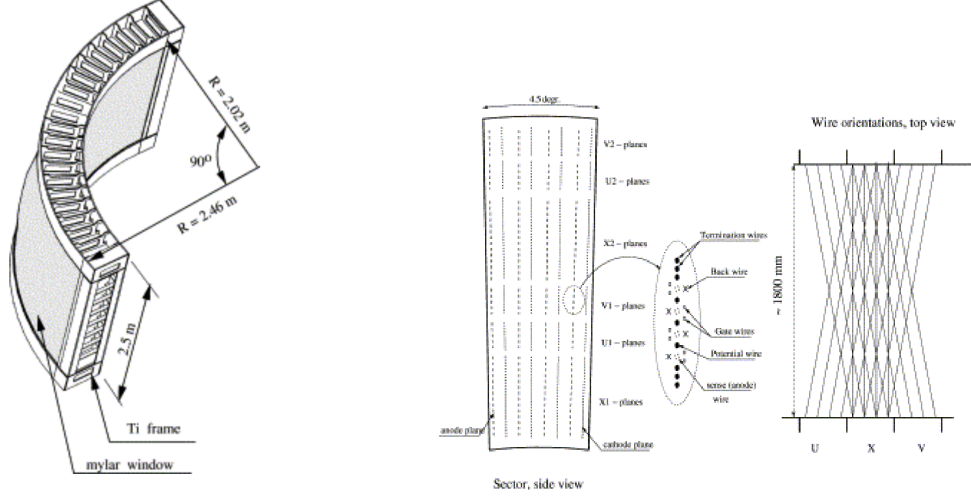


Figure 3.7: A diagram of the DC titanium frame that encloses the detector (left) and a diagram of the X, U, and V wires in the DC [27].

into 20 equal sectors covering 4.5 degrees in  $\phi$ . Each sector contains six types of wire modules stacked radially and labeled  $X1$ ,  $X2$ ,  $V1$ ,  $V2$ ,  $U1$ ,  $U2$ . The X wires run parallel to the beam to provide precise  $\phi$  measurements while the U and V wires are set at small angles of about six degrees relative to the X wires to provide information about the  $z$  position of the track. A diagram of the wire layout in each sector is shown in the right panel in Figure 3.7. In total, the DC consists of about 6,500 anode wires with 13,000 readout channels. The resolution for a single wire is  $165\text{ }\mu\text{m}$  in  $r\text{-}\phi$ , a single wire efficiency better than 99%, and a spatial resolution of 2 mm in the  $z$  direction.

### 3.2.5 Pad Chambers

The PCs are multi-wire proportional chambers composed of three separate layers of detectors measuring precise hit positions in the PHENIX tracking system which have the pseudorapidity acceptance as the DC. PC1 is the innermost layer and is located in both the east and west arms directly outside of the DC, providing a measurement of the  $x, y, z$  position at the back plane of the DC. PC2 is the second layer and is located near the RICH only in the west arm. PC3 is the outer layer and is located in both arms. PC3 gives a second space point on the straight line trajectories of the tracks through the detector, outside of the CM magnetic field as shown in Figure 3.4. PC1

hits are used in this analysis as an input to the pattern recognition to reduce the track background.

### 3.2.6 Ring Imaging Cherenkov Detector

The RICH detector is located directly behind the PC1 and produces the primary electron identification for PHENIX in the CA. The RICH is composed of two identical detectors in the CA. Each detector contains 48 mirror panels that focus Cherenkov light onto PMTs. The RICH is filled with radiator gas,  $\text{CO}_2$ , for the  $p+\text{Au}$  running. The RICH provides  $e/\pi$  (electron to pion) discrimination below the  $\pi$  Cherenkov threshold of  $\sim 4.5$  GeV/c. Figure 3.8 shows the energy over momentum  $E/p$  distribution in  $\text{Au}+\text{Au}$   $\sqrt{s_{NN}} = 200$  GeV collisions. The  $E$  comes from the EMCAL and the  $p$  comes from the DC tracks. When RICH hits are required in conjunction with DC tracks, a electron signal peak can be seen near  $E/p = 1.0$ , as expected for electrons depositing their full energy in the EMCAL.

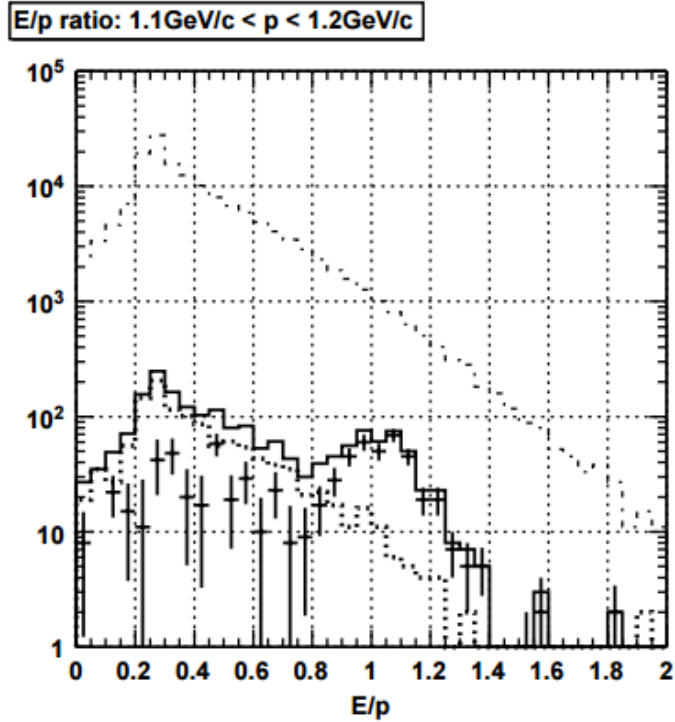


Figure 3.8: Ratio of energy to momentum for all Drift Chamber tracks (dashed-dotted line), and tracks associated with RICH hits (solid line) in  $\text{Au}+\text{Au}$   $\sqrt{s_{NN}} = 200$  GeV collisions. The  $p$  range is  $1.1 - 1.2$  GeV/c [28].

### 3.2.7 PHENIX Data Acquisition System

PHENIX makes use of a fast DAQ to manage the transfer and collation of hundreds of kB of event data (per event) from over two dozen independent detector subsystems at a rate of over 6 kHz. This amounts to writing to disk hundreds of MB/s, a data writing rate that the PHENIX DAQ consistently achieves for months of constant use.

The collection of a Granule Timing Module (GTM), Front End Modules (FEM), and a Data Collection Modules (DCM) is known as a “granule” and is the minimal combination of DAQ hardware sufficient for data collection, as shown in Figure 3.9. The output data of each detector subsystem is managed by a granule. Pipelined Field Programmable Gate Arrays (FPGA) with carefully controlled dead time are used to calculate the trigger decisions. The FPGAs are fed information from the experiment. Once the FPGAs compute the trigger decision, the trigger signals are monitored by the GTM. If the trigger decision is positive, the GTMs instruct the FEMs to release their data from their buffers and send them to the DCM of their granules. If the decision is negative, the FEMs are instructed to dump the data. Once the FEM is instructed to send its data downstream, it goes to the DCM and then is sent to the Event Builder (EvB).

#### 3.2.7.1 Triggering

PHENIX runs 32 distinct triggers simultaneously. Each of the triggers has a scale down number to control the relative bandwidth each trigger receives. To understand the PHENIX triggers, it is useful to learn about the beam clock.

The PHENIX trigger is tied to the clock of the blue beam, one of the two counter circulating rings of which RHIC is comprised. The clock rate is fixed at 9.38 MHz and is tied to the rate at which RHIC overlaps bunches of ions in the interaction regions. Every time a bunch of ions from the blue ring overlap with a bunch of ions from the yellow ring, there is a blue clock trigger. This clock is stable by necessity of the precision required to run a complex accelerator like RHIC.

One critical trigger that is used in this analysis is the minimum bias trigger. As the name

suggests, the trigger seeks to mark the detection of an ion collision while reducing to a minimum the bias to the type of the collision. To achieve this, data from the BBC are used. Although what constitutes a minimum observation varies with collision species, the BBC minimum bias trigger is generally defined as  $>0$  PMTs in each arm above threshold. Not only is this condition a good indication that a ion collision occurred, it is also the minimum information necessary to calculate the collision vertex position using the BBC. The vertex information is important because it is used to select collisions that occur in the narrow range of acceptance of the current PHENIX detector configuration. This range is  $-10 \text{ cm} < z < 10 \text{ cm}$ . For completeness, PHENIX takes BBC minimum bias triggers with z vertex cuts of 30 cm, 10 cm, and with no vertex cut. The collection of all these triggers is what is considered to be the PHENIX minimum bias trigger.

In Run 15, a high multiplicity trigger was implemented to enhance event statistics for events producing the largest number of particles (i.e. the most central, violent collisions). This trigger was given a large fraction of the bandwidth and consisted of requiring at least 35 out of 64 PMTs in the south arm (Au-going direction) of the BBC. More details about this trigger are located in Section 3.2.8.

Table 3.1: An example 2015  $p+\text{Au}$  at  $\sqrt{s_{NN}} = 200 \text{ GeV}$  trigger configuration and parameters. A trigger's scale down number reduces its rate by  $1/(1+\text{scale down})$ .

Trigger Name	Scale down	Trigger rate	Vertex cut	Part of minimumbias
Clock	196077	45 Hz	N/A	no
<i>BBC(&gt; 0 PMTs) narrowvtx</i>	100	695 Hz	10cm	yes
<i>BBC(&gt; 0 PMTs)</i>	2083	88 Hz	30cm	yes
<i>BBC(&gt; 0 PMTs) novertex</i>	3959	94 Hz	<i>no cut</i>	yes
<i>BBC(&gt; 35 PMTs)</i>	1	1640 Hz	10cm	no

### 3.2.7.2 Event Builder

Following the PHENIX DAQ data path, after a positive trigger decision has been sent to each of the granules, the granules' data packets are sent from that granule's FEM to the DCM and then to the event builder. It is the event builder's job to associate each granule's data packet from the same collision event into one bundle of data known as an event. The event builder consists of

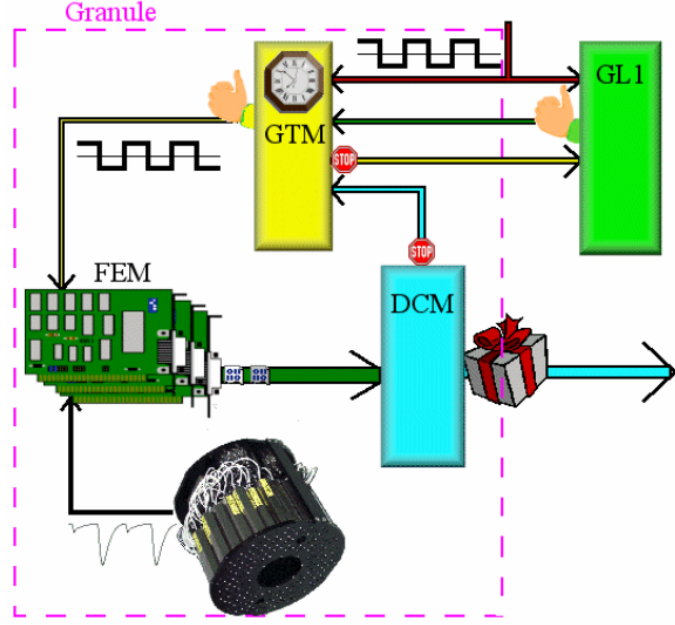


Figure 3.9: Diagram of a granule. Granules are the building blocks of the PHENIX DAQ. Each detector subsystem has at least one granule. This granule shows the BBC.

Sub Event Buffers (SEB), Assembly Trigger Processors (ATP), an Event Builder Controller (EBC), and a Gigabit Ethernet Switch for the communication management. The EvB transfers the data to long-term storage at the RHIC Computing Facility. Figure 3.10 shows a diagram for how these components are connected.

Granules send the data packets to the specific SEB assigned to that granule. The EBC receives global trigger information and assigns each ATP a specific collision event. The ATP then requests the data from all of the SEBs for the specific event assigned to it by the EBC. Once the ATP is successful, it writes the assembled event to disk and the EBC instructs the SEBs to flush the buffer for that event.

### 3.2.8 Run 15

Run 15 is the RHIC running period in the year 2015, which marks the fifteenth in consecutive years of RHIC running since the year 2000. Run 15 began in January 2015 and ended in June of 2015. There were approximately eleven weeks of good physics data taken, approximately five weeks

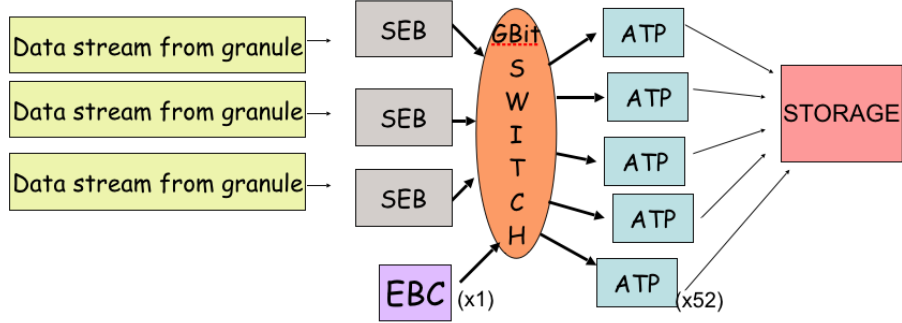


Figure 3.10: Diagram of the event builder.

of polarized  $p+p$  collisions at  $\sqrt{s} = 200$  GeV, approximately five weeks of polarized  $p+\text{Au}$  collisions at  $\sqrt{s_{NN}} = 200$  GeV, and approximately one week of research viable  $p+\text{Al}$  collisions  $\sqrt{s_{NN}} = 200$  GeV. Of interest to this thesis are the  $p+p$  and  $p+\text{Au}$  datasets.

Table 3.2: Some relevant RHIC parameters from Run 15.

Collision Species	$p+p$	$p+\text{Au}$	units
Total Particle Energy	100.2	$103.9 + 100.0$	GeV/nucleon
Ions per Bunch	225	$225 + 1.6$	number $\times 10^9$
Number of Bunches	111	111	number
Luminosity Average Per Fill	$6,300 \times 10^{28}$	$45 \times 10^{28}$	$\text{cm}^{-2}\text{s}^{-1}$
Total Delivered Luminosity	382	1.27	$\text{pb}^{-1}$
Average Fill Lifetime	8	7	hours

In addition to providing the minimum bias as trigger for Run 15, the BBC was used to implement a high-multiplicity trigger in order to enhance the amount of the top 5% highest multiplicity events. The high-multiplicity trigger requires at least 35 of the 64 BBC south arm PMTs to be above threshold in a given event to be satisfied. The relevant BBC arm for  $p+\text{Au}$  is the south arm since that is the Au-going direction so the multiplicity is much higher. The central trigger enhancement can be seen in Figure 3.11.

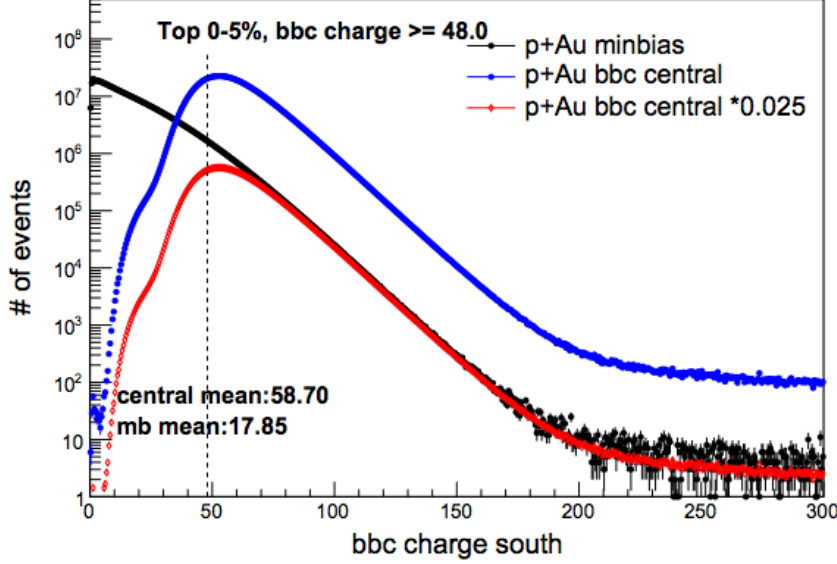


Figure 3.11: The distribution of BBC charges in  $p+Au$  at  $\sqrt{s_{NN}} = 200$  GeV events for different triggers. The black curve is the distribution of charges for the minimum bias trigger. The blue and red curves are the distributions of charges for the high multiplicity trigger. The red curve being scaled by a factor of 1/40 to show agreement with the black curve. The definition of the top 5% more central events are BBC south charges  $\geq 48.0$ . The plot shows the large enhancement of the number of 0-5% centrality events that are gained using the high multiplicity trigger compared to the number of 0-5% centrality from the minimum bias trigger alone.

### 3.2.8.1 Beam Collision Geometry

For the 2015  $p+Au$  collisions at  $\sqrt{s_{NN}} = 200$  GeV running, the RHIC's blue and yellow beams were not in perfect accordance to the PHENIX coordinate system. This was manifested in two separate ways. First of all, the collision vertex is significantly offset from the  $z$ -axis to which all of the PHENIX detectors are aligned. This is a typical situation in PHENIX datasets but it must be addressed. The other effect, and the more significant of the two, comes from the fact that the beams are colliding at an angle of 3.6 mRad in the  $x$ - $z$  plane, as illustrated in Figure 3.12.

The reason for this is because of the accelerator ring magnet requirements for running  $p+Au$  at  $\sqrt{s_{NN}} = 200$  GeV at RHIC. It is highly desirable to have the beams at equal energy per nucleon, and since the proton and the Au have different  $Z/A$  ratios, the magnets require different settings to control the beams. The final  $DX$  magnet constrains both beams and moves them to cross at

the interaction region in the middle of PHENIX. The beam angle is needed to offset the beams in the DX magnet field [61].

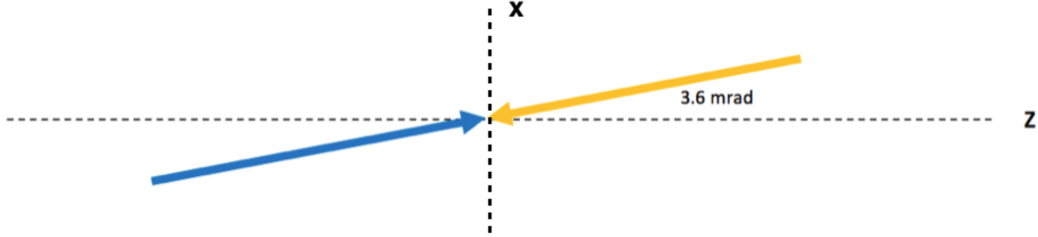


Figure 3.12: A vector diagram illustrating the yellow and blue beam angle confirmation relative to the PHENIX coordinate system.

The average collision vertex location in  $x$  and  $y$  is known as the beam center. The beam center varies over the course of data taking but its values on average are  $(x, y) = (0.206, 0.065)$  cm. The distribution of vertices in  $z$  from collision events can be seen in Figure 3.13. Due to the fact that the beams are colliding at an angle in the  $x$ - $z$  plane, the  $x$ -component of the beam center will have a  $z$ -vertex dependence with a slope of -0.0036 cm of  $x$  per 1 cm of  $z$ . Apart from how the beam angle effects the beam center values, it also violates the expectation of a uniform  $\phi$  distribution of particles with respect to PHENIX detectors. PHENIX detectors are designed and aligned, with respect to the PHENIX coordinate system, with the expectation of geometric symmetry. A significant beam collision angle with respect to PHENIX detectors would be equivalent to PHENIX detectors being tilted, which would violate geometric symmetry. The physics analysis described in this thesis is sensitive to these beam geometry effects. A discussion on how to account for these effects will be in Chapter 4.

### 3.2.9 Centrality Determination

The centrality determination is done by adding up all BBC South (BBCs) (Au-going direction) PMT charges for every event and then splitting up that distribution into equivalent centrality bins. This procedure, which is the same used for  $d$ +Au, as documented in Ref [29], is used to

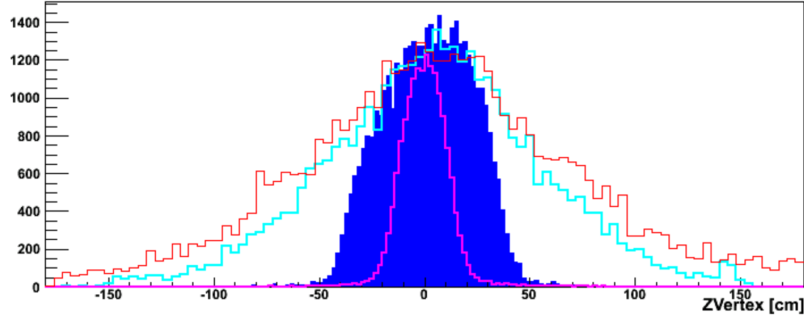


Figure 3.13: The BBC  $z$ -vertex distribution in a typical  $p$ +Au run for different triggers as described in Table 3.1. The teal curve is the BBC( $>0$  PMTs) novertex trigger, the blue is the BBC( $>0$  PMTs), and the magenta is the BBC( $>0$  PMTs) narrowvertex.

associate a centrality bin with the number of binary collisions from Monte Carlo Glauber (MC-Glauber), as discussed in Section 2.3.1.1. An example of such a MC-Glauber event for  $d$ +Au is seen in Figure 3.14.

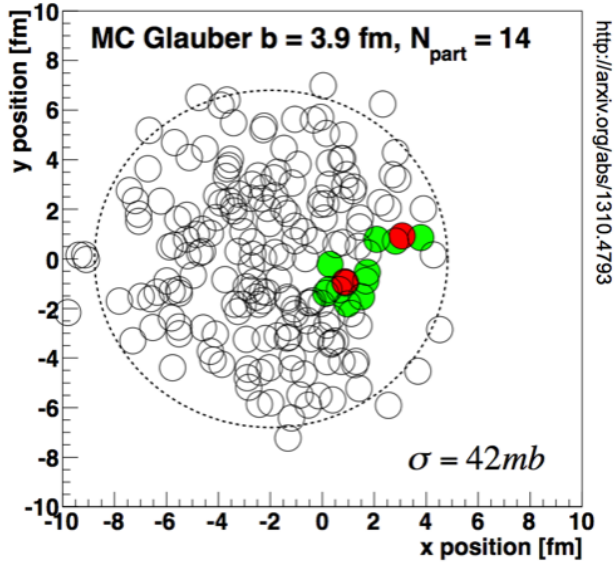


Figure 3.14: A Monte Carlo Glauber  $d$ +Au event display. Each circle is a nucleon and filled circles are nucleons with at least one collision. The red nucleons are from the projectile (deuteron) and the green nucleons are participants from the target (gold) [29].

In this procedure, the total BBC charge is assumed to be proportional to the number of binary collisions in a  $p$ +Au collision. Fluctuations in nucleon positions are described probabilistically via

the Negative Binomial Distribution (NBD) as defined:

$$\text{NBD}(x; \mu, \kappa) = \left(1 + \frac{\mu}{\kappa}\right) \frac{(\kappa + x - 1)!}{x!(\kappa - 1)!} \left(\frac{\mu}{\mu + \kappa}\right)^x \quad (3.2)$$

where  $\mu$  and  $\kappa$  are the mean and positive exponent parameters. The NBD was chosen for this situation due to the linear scaling of the NBD parameters, i.e. randomly sampling from  $n$   $\text{NBD}(\mu, \kappa)$  becomes  $\text{NBD}(n\mu, n\kappa)$ . We fold the MC-Glauber with the NBD such that the charge distribution is described as

$$P(x) = \sum_{n=1}^{N_{COL}^{\text{max}}} \text{Gl}(n) \times \text{NBD}(x; n\mu; n\kappa), \quad (3.3)$$

where  $x$  is the BBCs charge and  $\text{Gl}(n)$  is the event normalized Glauber distribution [29]. The two parameters  $\mu$  and  $\kappa$  are fit to the experimental BBCs charge distribution, as shown in Figure 3.15. This figure shows good agreement between the data and the MC-Glauber + NBD fit. The best fit NBD parameters are  $\mu = 3.14$ ,  $\kappa = 0.47$ .

There is a deviation at small BBCs charge because the minimum bias trigger is inefficient due to the fact that a PMT must be hit in both the BBC south and north. The bottom panel of Figure 3.15 is the ratio of the data to the theory curve and shows that the agreement is good at a charge of 10 and greater. This ratio is fit to determine the minimum bias trigger efficiency as it “turns on.” This fit has good agreement with the turn-on curve which can be integrated to determine that the minimum bias trigger is  $84\% \pm 4\%$  efficient. By combining the calculated  $p+\text{Au}$  cross section with the 84% trigger efficiency, we determine the total inelastic  $p+\text{Au}$  cross section  $\sigma = 1.76$  b. Thus, centrality is defined as a percentage of the total inelastic cross section.

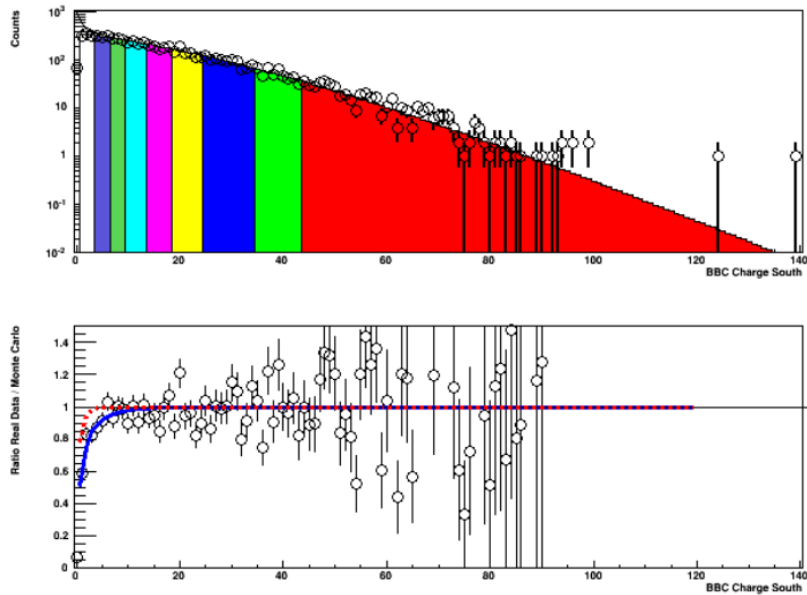


Figure 3.15: Real data for BBCs charge shown as open circles and MC-Glauber + NBD (top). The colors correspond to the various percentiles relative to the total inelastic  $p + \text{Au}$  cross section, from right to left: 0–5%, 5–10%, 10–20%, 20–30%, 30–40%, 40–50%, 50–60%, 60–70%, and 70–84%. The blue and red curves correspond to the minimum bias trigger efficiency in all inelastic collisions and inelastic collisions producing a particle at mid-rapidity, respectively (bottom).

## Chapter 4

### Analysis

This chapter contains an extensive discussion of the data analysis techniques in the physics measurement. First we describe the building blocks of the  $v_2$  measurement, then we examine the event plane analysis techniques and the sources of systematic uncertainty.

#### 4.1 The Building Blocks of the Measurement

Prior to any analysis, the raw data collected by various PHENIX subsystems must be reconstructed into well-defined software objects encapsulating information of the particles that traversed the detector. Although we have already discussed the subsystems used in this analysis in Chapter 3, this section provides in-depth information on central arm tracks, FVTX clusters, and BBC photomultiplier tubes (PMTs), and the physics variables they contain. Figure 4.1 displays the coordinate system for PHENIX.

##### 4.1.1 Central Arm Tracks

Central Arm (CA) tracks are the representation of charged particles emitted from the heavy ion collision that are detected by detectors in the PHENIX central arms. There are two central arms, each one covering an acceptance of  $\pm 0.35$  in pseudorapidity and a total azimuth acceptance of  $\frac{\pi}{2}$ . The relevant detectors in the CA for this analysis include the Drift Chamber (DC), the Pad Chambers (PC) and the Ring Imaging Cerenkov (RICH) detector. As discussed in Chapter 3, the DC provides momentum information; the PC provide track quality metrics; and the RICH provides

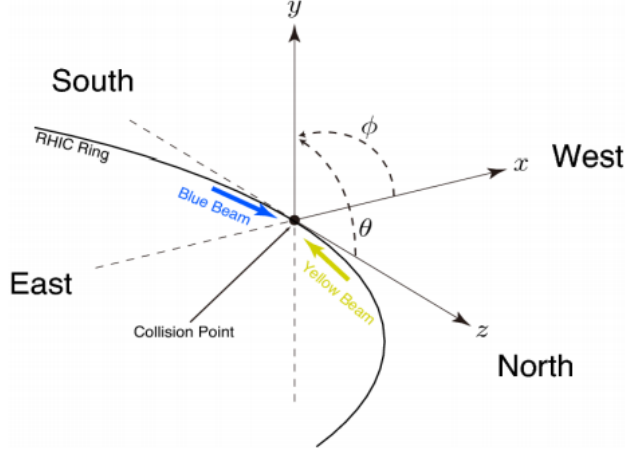


Figure 4.1: Reference coordinate system for the PHENIX detector. The origin is set at the collision point, around which the detector is centered. The beam runs parallel to the (longitudinal)  $z$ -axis, where the direction of positive  $z$  is defined as **north**. The **east** and **west** directions are defined as perpendicular to the longitudinal direction, where the direction of positive  $x$  is defined as **west**.

electron identification.

The main physical parameter of CA tracks is the momentum vector  $\vec{p} = (p_x, p_y, p_z)$  of the particles, defined at the collision vertex. This analysis uses tracks with momentum  $0.2 \text{ GeV}/c < |p_T| < 3 \text{ GeV}/c$ , a  $p_T$  range where the momentum resolution is good, as shown in the left panel of Figure 4.2. The right panel of Figure 4.2 shows the  $p_T$  distribution of CA tracks up to  $10 \text{ GeV}/c$ : a smooth linearly falling distribution on a log scale with a small number of fake tracks at high  $p_T$ . The azimuthal angle and pseudorapidity of the track are calculated from the components of its momentum vector, as follows:

$$\phi = \arctan\left(\frac{p_y}{p_x}\right), \quad (4.1)$$

$$\eta = \text{arsinh}\left(\frac{p_z}{p_T}\right). \quad (4.2)$$

In addition to momentum, CA tracks provide a number of other parameters that can be used to ensure the quality of tracks and isolate a sample corresponding to charged hadrons. These include  $zed$  in the DC,  $d\phi$  and  $dz$  in the PC,  $n0$  in the RICH, and the general track quality calculated from DC and PC information. These variables are defined as follows:

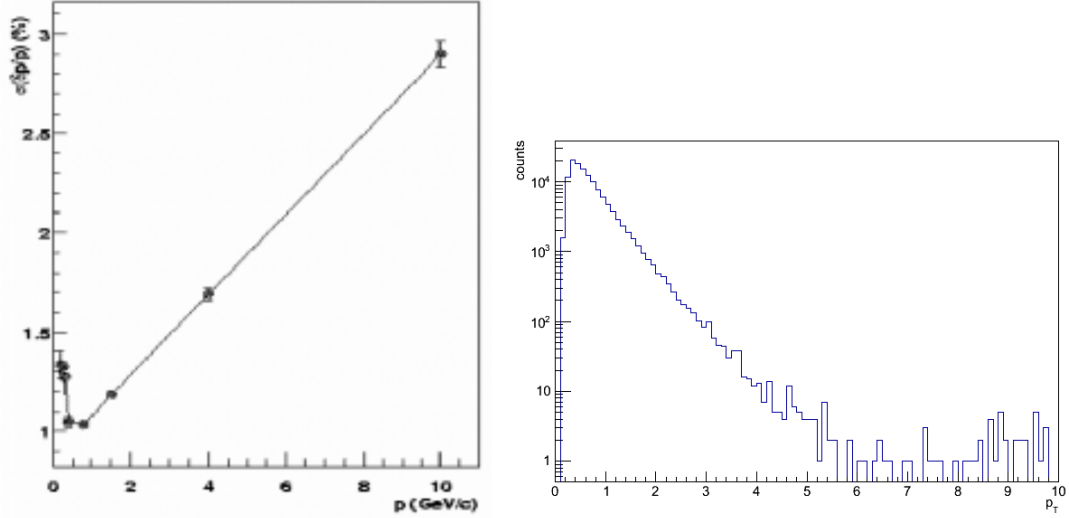


Figure 4.2: Momentum resolution  $\sigma_p/p$  as a function of the reconstructed track momentum,  $p$  for simulated single-particle events [30] (left) and the transverse momentum  $p_T$  distribution of CA tracks in  $p+Au$  events at  $\sqrt{s_{NN}} = 200$  GeV. High  $p_T$  tracks ( $p_T > 5$   $\text{GeV}/c$ ) observed correspond to unsubtracted background (right).

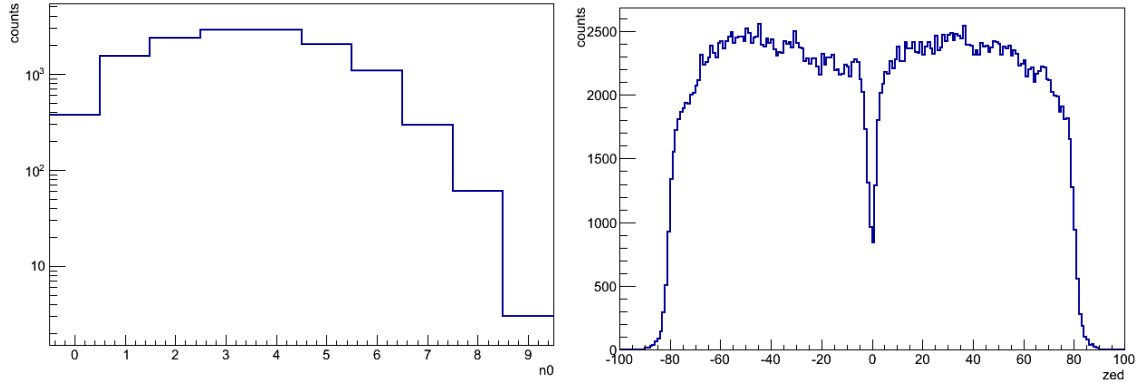


Figure 4.3: The distribution of (left)  $n_0$ , i.e., the number of PMTs fired in the RICH, and (right)  $zed$ , i.e., the longitudinal position of tracks in the DC, for CA tracks in 0–5% central  $p+Au$  events at  $\sqrt{s_{NN}} = 200$  GeV. The structure observed in the  $zed$  distribution corresponds to a gap in the detector acceptance.

- the  $zed$  variable corresponds to the longitudinal position of the track in the DC, as shown in Fig. 4.3 (right panel);
- the  $d\phi$  and  $dz$  variables quantify the distance between a track projection and its associated

hits in the PC. In order to make standard cuts on these variables, their distribution must be calibrated to a standard Gaussian in a procedure known as signalization, described in subsection 4.1.1.1;

- the  $n0$  variable, used for electron identification, corresponds to the number of PMTs fired in the RICH that match the DC track projection, as shown in Fig. 4.3;
- the track quality category, which is based on the PC1 and DC wire hits used as well as DC wire momentum information, defined in Tables 4.1 and 4.2.

Table 4.1: Quality categorization of CA tracks, as a function of PC1 and DC wire hits. The quality parameters used in this analysis are 31 and 63 to maximize information available. Table from Ref [3].

Quality	PC1 found	PC1 unique	UV found	UV unique
17,18,19	1	0	0	0
21,22,23	1	0	1	0
29,30,31	1	0	1	1
49,50,51	1	1	1	0
61,62,63	1	1	1	1

Table 4.2: Quality categorization of CA tracks, as a function of DC wire momentum information. The quality parameters used in this analysis are 31 and 63 to maximize information available. Table from Ref [3].

Quality	X1 used	X2 used
17,21,29,49,61	1	0
18,22,30,50,62	0	1
19,23,31,51,63	1	1

The quality cuts Table 4.3 summarizes the CA track cuts used in this analysis to reduce the track background.

Table 4.3: CA Track cuts for each relevant variable and their units.

variable	cuts	units
$p_T$	$0.02 < p < 10.0$	GeV/c
zed	$ zed  < 75$	cm
PC3 $d\phi$	$ d\phi  < 2.0$	radians $\times 10^9$
PC3 $dz$	$ dz  < 2.0$	cm
$n_0$	$n_0 < 1$	count
quality	63 or 31	N/A

#### 4.1.1.1 Sigmalization of PC Variables

The goal of PC variables  $d\phi$  and  $dz$  is to provide criteria to determine if the  $\phi$  orientation and  $z$ -direction of the track match between the third layer of the PC and the DC. The sigmalization is done in the minimum bias sample and is valid for all other centrality selections. We did the sigmalization procedure for tracks in different transverse momentum bins, separately in the east and west arms, and for positive and negative particles. The  $d\phi$  and  $dz$  distributions were fitted with a double-Gaussian function (one Gaussian for the signal and one Gaussian for the background) and then the parameters were interpolated as a function of  $p_T$ . Fig. 4.4 a) shows a fit to the sigmalized  $d\phi$  distribution, and Fig. 4.4 b) shows a fit to the sigmalized  $dz$  distribution for tracks with  $1.0 < p_T < 1.1$  (GeV/c) in both the west and east arms as well as both positively and negatively charged particles. Then we fit the signal Gaussian mean and sigma to a polynomial function. Once these variables had been sigmalized, we selected only the tracks within a  $\pm 2\sigma$  cut.

#### 4.1.2 FVTX Clusters

The FVTX consists of four silicon layers in each of the north and south directions, covering an acceptance of  $1 < |\eta| < 3$  and spanning the full azimuth. FVTX clusters correspond to the spatial location where charged particles hit one of the silicon layers. Each cluster is expected to correspond to a single charged particle in the case of  $p$ +Au collisions, because of the low multiplicity relative to Au+Au collisions. These clusters have a spatial resolution in  $r$  and  $\phi$  of 50  $\mu\text{m}$  and 0.14 radians, respectively, and have an RMS along the  $z$ -direction that corresponds to the width of an

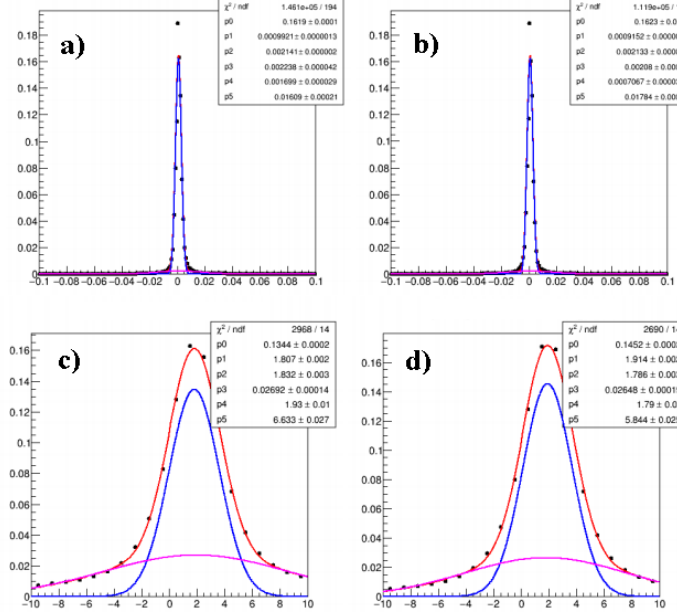


Figure 4.4: The PC3 matching  $d\phi$  fit in range  $1.0 \text{ GeV}/c < p_T < 1.1 \text{ GeV}/c$  for positive a) and negative b) hadrons and the  $dz$  signalization for positive c) and negative d) hadrons. The blue and pink lines are single Gaussian fits to the signal and background, respectively, which are combined in the red line.

FVTX layer, of  $\frac{200}{\sqrt{12}} \mu\text{m}$  [25]. Due to the  $p+\text{Au}$  collision system's inherent asymmetry, the majority of particles are produced in the Au-going (south or backward) direction. Taking into account this asymmetry, only the clusters from the south arm are used for calculations in this analysis. In a typical 0–5% centrality event, there are on average  $\sim 1500$  FVTX clusters in the south arm alone. Average hit distributions are shown in Figure 4.5. The clusters are used for calculating the event plane.

#### 4.1.3 BBC PMTs

The BBC provides information on the position, time of arrival, and number of charged particles that hit the BBC's quartz radiator material. The BBC acceptance is  $3.1 < |\eta| < 3.9$  and spans the full azimuth. The resolution of the detector in  $x$  and  $y$  is 5 cm, corresponding to the diameter of a BBC PMT. In addition to spatial information, the BBC provides charge information,

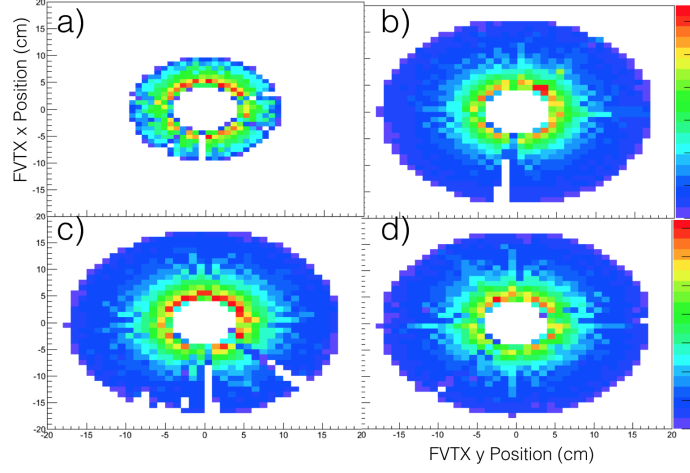


Figure 4.5: Distribution of FVTX clusters in  $x$  and  $y$  for layers 1, 2, 3, and 4 for panels a), b), c), and d), respectively. The color scale corresponds to the number of counts.

calibrated so that a value of 1.0 corresponds to a single charged particle hitting the detector (i.e. one minimum ionizing particle traversing the quartz). Figure 4.6 shows the layout of the PMTs for the BBC. As discussed in section 3.2.2, the information regarding arrival time and particle charge can be used to calculate the  $z$ -vertex of the collision.

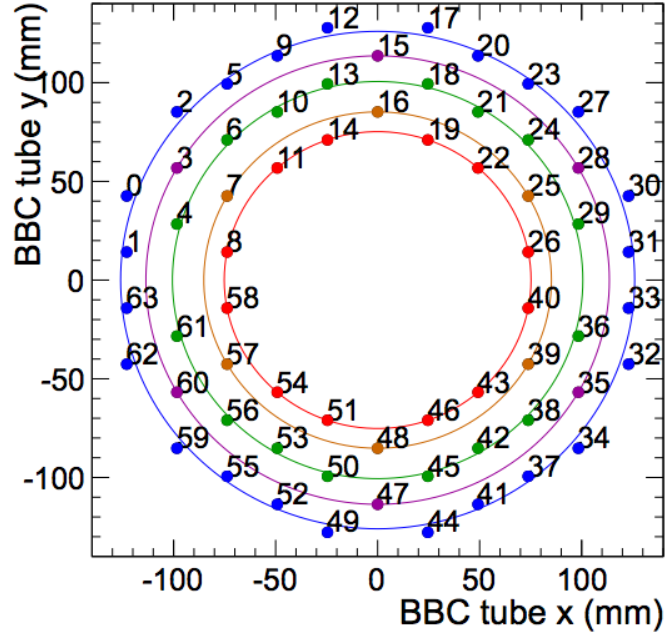


Figure 4.6: Diagram showing the positions of the PMTs for the south BBC detector. Rings shown with the same color indicate PMTs at an approximate common radius.

## 4.2 The Event Plane Method

Details of the event plane method were given in Chapter 2 Section 2.2.4. The goal of this thesis is to measure  $v_2$ , which is related to collective behavior as evidenced by correlations among particles. These correlations exist relative to the orientation of the collision. The event plane method measures the azimuthal anisotropy in final state particles. The event plane method uses final state particles to calculate the event plane angle from the data. A different set of final state particles are used to define the event plane in the FVTX or BBC and measure the  $v_2$  in the CA.

For this analysis, the event plane is calculated separately for each of the forward detectors mentioned above, i.e., the BBC and the FVTX. We only use the south (Au-going) side of each detector, referred to here as the BBCS and the FVTXS. For the FVTXS, the Q-vector is calculated in each event as

$$Q_x = \sum_{i=1}^{N_{\text{cluster}}} (\cos(n\phi_i)) \quad (4.3)$$

$$Q_y = \sum_{i=1}^{N_{\text{cluster}}} (\sin(n\phi_i)) \quad (4.4)$$

$$\phi_i = \arctan \left( \frac{y_{\text{cluster}}^i}{x_{\text{cluster}}^i} \right) \quad (4.5)$$

where  $N_{\text{cluster}}$  is the number FVTXS clusters in that event and  $x_{\text{cluster}}^i$  and  $y_{\text{cluster}}^i$  are the  $x$  and  $y$  components of the  $i$ th FVTXS cluster in that event. At this point, this Q-vector is calculated with no cluster dependent weight factor because each cluster is taken to be the representation of one particle in each layer.

For the BBCS, the Q-vector is calculated in each event as

$$Q_x = \sum_{i=1}^{N_{\text{PMT}}} (w_i \cos(n\phi_i)) \quad (4.6)$$

$$Q_y = \sum_{i=1}^{N_{\text{PMT}}} (w_i \sin(n\phi_i)) \quad (4.7)$$

$$Q_w = \sum_{i=1}^{N_{\text{PMT}}} (w_i) \quad (4.8)$$

$$\phi_i = \arctan \left( \frac{y_{\text{PMT}}^i}{x_{\text{PMT}}^i} \right) \quad (4.9)$$

where  $w_i$  is the scaled charge collected on the PMT and  $N_{\text{PMT}}$  is the number of PMTs that fired (above threshold) in each event.

Finally, the  $v_n$  are calculated using a combination of the BBCS or FVTX Q-vectors and the CA tracks as

$$v_n = \frac{\left\langle \left\langle \cos(n(\phi^{CA} - \Psi_n^{BBCS,FVTXS})) \right\rangle \right\rangle}{\text{Res}(\Psi_n^{BBCS,FVTXS})}. \quad (4.10)$$

In this analysis, we are concerned only with measuring the second-order harmonic  $v_2$ .

#### 4.2.1 Event Plane Resolution Calculation

As mentioned above, the event plane resolution is calculated using the standard 3-subevent method [43]. The strategy of this method is to measure  $\Psi_2$  with three different detectors in the same event with the expectation that all three are measuring the same event plane angle. The event plane resolution is defined as

$$\text{Res}(\Psi_2^A) = \sqrt{\frac{\langle \cos(2(\Psi_2^A - \Psi_2^B)) \rangle \langle \cos(2(\Psi_2^A - \Psi_2^C)) \rangle}{\langle \cos(2(\Psi_2^B - \Psi_2^C)) \rangle}}, \quad (4.11)$$

where A, B, and C are three detectors measuring the same event. Here, the term “subevent” refers to the specific subset of particles measured by a given detector [43].

In this analysis, the three detectors used to provide the required three subevents are the FVTX-south, the BBC-south, and the CA, which span pseudorapidity acceptances of  $-3 < \eta < -1$ ,  $-3.9 < \eta < 3.1$ , and  $|\eta| < 0.35$ , respectively. Figure 4.7 shows the event-by-event relative difference

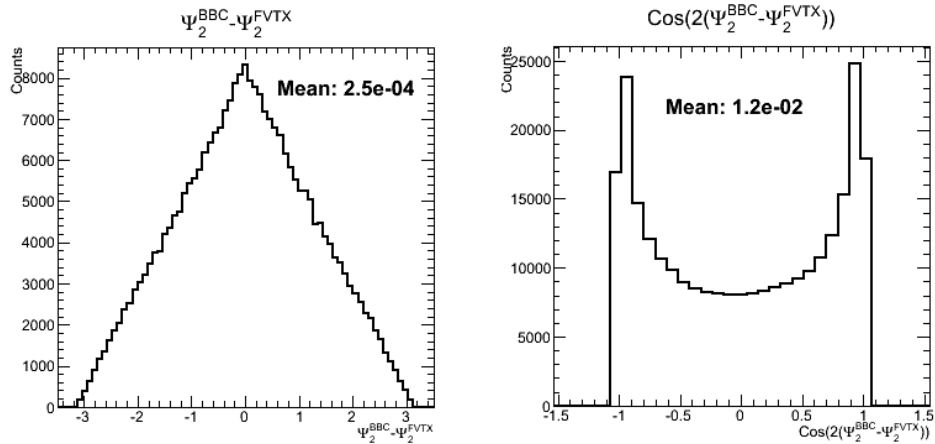


Figure 4.7: Intermediate steps involved in calculating the event resolution. Raw difference between the event plane angles for two different detectors (left). This distribution is triangular because it is the result of the cross-correlation of two nearly uniform distributions,  $\Psi_2^{\text{FVTXS}}$  and  $\Psi_2^{\text{BBCS}}$ . The cosine of two times the difference between the two event plane angles. The average of this distribution is used in Equation 4.11 (right).

of  $\Psi_2^{\text{BBCS}}$  and  $\Psi_2^{\text{FVTXS}}$ . Unlike the BBCS and the FVTXS, the CA detector does not have full azimuthal acceptance coverage. Therefore, the event plane angle cannot be reliably calculated with this detector for events whose event plane points outside of the acceptance. In order to solve this problem, we calculate the event plane resolution using a different, yet mathematically equivalent formulation that does not make use of  $\Psi^{\text{CA}}$ , as given below for the  $\Psi^{\text{FVTXS}}$ :

$$Res(\Psi_n^{\text{FVTXS}}) = \sqrt{\frac{\langle\langle \cos(n(\Psi_n^{\text{FVTXS}} - \phi^{\text{CA}})) \rangle\rangle \langle\langle \cos(n(\Psi_n^{\text{FVTXS}} - \Psi_n^{\text{BBCS}})) \rangle\rangle}{\langle\langle \cos(n(\phi^{\text{CA}} - \Psi_n^{\text{BBCS}})) \rangle\rangle}}, \quad (4.12)$$

where there is a double average over each CA track and each event.

Table 4.4: The event plane angle resolutions for the FVTXS and the BBCS for the second and third order harmonics.

Detector	$n = 2$	$n = 3$
FVTXS	0.216	0.010
BBCS	0.052	0.010

#### 4.2.2 Event Plane Flattening Calibration

In order for the event plane to be useful in making a  $v_n$  measurement, the event plane angle must be calibrated such that its distribution is uniform. For the event plane method, a physical assumption is made that the true distribution of  $\Psi_n$  angles will be uniform since physically there is no preferred orientation of the collision. If the measured  $\Psi_n$  distribution is not flat, we attribute that behavior to variations in the efficiency of detecting charged particles as a function of  $\phi$ . Thus, the event plane calibration procedure seeks to correct for these non-uniformities in acceptance, and restore the  $\Psi_n$  distribution to the physical expectation of uniformity. We employ a procedure to re-center and flatten the measured non-uniform  $\Psi_n$  distribution.

Figure 4.8 shows an example of  $\Psi_2$  distributions for the BBCS at the different stages of the calibration. The raw  $\Psi_2$  (shown in red) has a significant deviation from uniformity which needs to be corrected. The flattening calibration attempts to correct for this lack of uniformity by shifting the  $\Psi_2$  value of each individual event by an amount corresponding to the deviation of the overall distribution for all events. Although this procedure results in a uniform  $\Psi_2$  distribution, applying too large of a correction arising from an exceedingly distorted initial distribution can lead to systematic effects on the  $v_2$  measurement, which will be discussed in the next section. Therefore, it is important to address any systematic effects that would affect the uniformity of the  $\Psi_2$  distribution.

The flattening calibration requires two steps to completely flatten the  $\Psi_n$  distribution. The first step of the calibration is to re-center the mean of the raw  $\Psi_n$  distribution. The second step is to Fourier transform the re-centered distribution and use the transformation to shift the  $\Psi_n$  values to a uniform distribution. With flattening, each  $\Psi_n$  is transformed to  $\Psi_n + \Delta\Psi_n$ .  $\Delta\Psi_n$  is defined as

$$\Delta\Psi_n = \sum_{i=1}^N \left( \frac{2}{i} (\sin(i\Psi) F_i^{\cos}(f(\Psi_n)) - \cos(i\Psi) F_i^{\sin}(f(\Psi_n))) \right), \quad (4.13)$$

where  $N$  is the number of components,  $F_i^{\cos}(f(x))$  is the  $i$ th component of the cosine Fourier transform of  $f(x)$ , and  $f(\Psi_n)$  is the  $\Psi_n$  distribution. For this analysis,  $N = 12$  is a sufficient

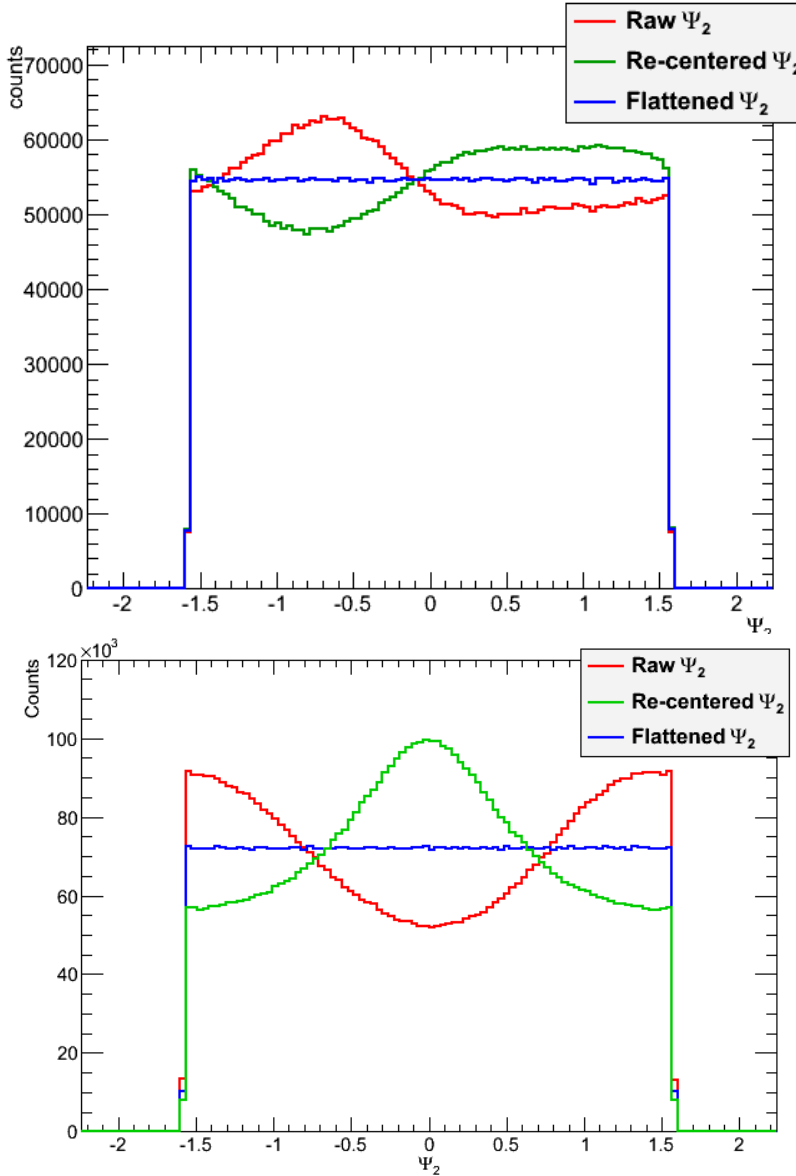


Figure 4.8: This is the  $\Psi_2$  distribution projected over all z-vertex bins at different steps during the calibration. The top is from the FVTX south and the bottom is from the BBC south. The range of the  $\Psi_2$  resolution is from  $-\frac{\pi}{2}$  to  $\frac{\pi}{2}$  because of the periodicity. The raw (in red)  $\Psi_2$  distribution has a sinusoidal shape. The re-centered (in green)  $\Psi_2$  distribution moves the mean. The flattened (in blue)  $\Psi_2$  distribution spreads out the counts so that there is uniformity. Each calibration step preserves the integral.

number of components to flatten the  $\Psi_n$  distribution. The re-centering and flattening calibration is done in separate 30 z-vertex bins since the detector acceptance in  $\phi$  will vary with z-vertex.

### 4.3 East West $v_2$ Discrepancy

As discussed in the previous section, distortions in the raw  $\Psi_2$  distribution can cause distortions in the measurement of  $v_2$ . In this section, we discuss how the beam alignment affects the raw  $\Psi_2$  distribution and how it can be corrected.

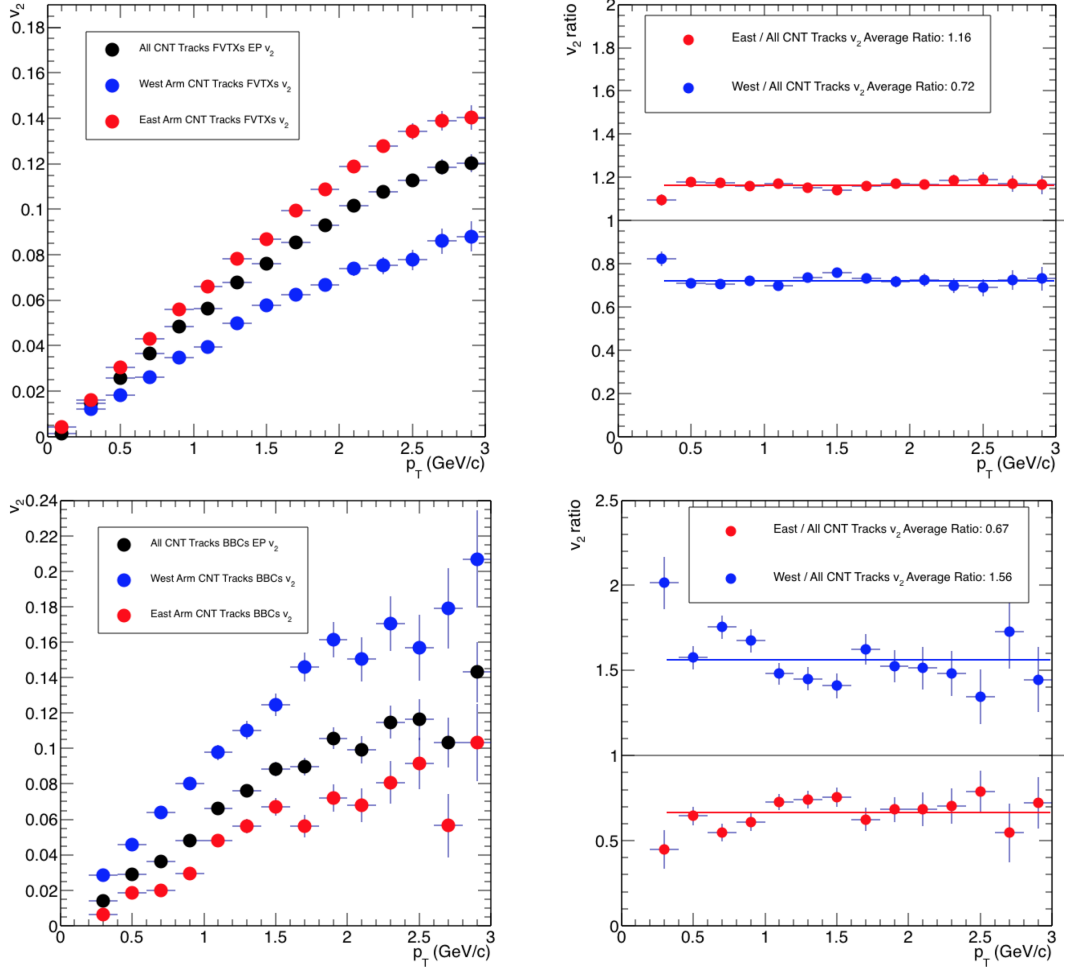


Figure 4.9: First attempt at measuring  $v_2(p_T)$  with the event plane as calculated with the FVTXS (top left) and the BBCS (bottom left) in the  $p+\text{Au}$  at  $\sqrt{s_{NN}} = 200$  GeV dataset, using the default resolution as shown in Table 4.4. The black points show  $v_2$  measured using all CA tracks. The blue and red points show  $v_2$  measured using only tracks in the west and east arms, respectively. The ratios are fit with a constant, whose value is shown in the legend.

As shown in Figure 4.9,  $v_2$  is different when measured using tracks in the west ( $-1 < \phi < 1$ ) and east arm ( $2 < \phi < 4$ ) of the CA. This is a systematic effect explained by the colliding beams

not being parallel to the longitudinal axis of PHENIX. When examining beam alignment effects on the  $v_2$  measurement, we can quantify the east-west  $v_2$  asymmetry by calculating  $R_{v_2}$  which is calculated by:

$$R_{v_2} = \frac{\int v_2^{\text{east}}(p_T) dp_T}{\int v_2^{\text{west}}(p_T) dp_T}. \quad (4.14)$$

In Figure 4.9,  $R_{v_2^{\text{FVTXS}}}$  can be extracted by taking the ratio of the numbers in the legend of the upper right plot and  $R_{v_2^{\text{BBCS}}}$  can be extracted the same way for the numbers in the bottom right plot's legend. The  $R_{v_2^{\text{FVTXS}}} = 1.61$  while the  $R_{v_2^{\text{BBCS}}} = 0.43$ , indicating large east west asymmetry in both measurements, although the difference in the BBCS is bigger. It is interesting to note that the splitting of the east and west  $v_2$  measurements goes in opposite directions for the BBCS as compared to the FVTXS. To understand where the discrepancy in these  $v_2$  measurements comes from, we examine the effects of the beam alignment on the  $v_2$  measurement.

#### 4.4 Correcting for the Effects of Beam Alignment

As discussed in Section 3.2.8.1, due to the nature of running  $p+\text{Au}$  at  $\sqrt{s_{NN}} = 200$  GeV at RHIC, the beam geometry was not in accordance with the PHENIX coordinate system. First of all, the collision vertex is significantly offset from the z-axis to which all of the PHENIX detectors are aligned. The other beam geometry effect, and the more significant of the two effects, comes from the fact that the beams are colliding at an angle of 3.6 mRad in the x-z plane as shown in Figure 4.10 [61]. The reason a non-ideal beam geometry creates an east west  $v_2$  measurement difference is because of the assumption that the ideal event plane angle is azimuthally isotropic during the event plane flattening calibration. In the translated and rotated frame where the beams are aligned with the z-axis the event plane distribution would be uniform, but in the lab frame the event plane distribution in  $\phi$  would have regions of enhancement and reduction. The event plane flattening calibration algorithm restores a non-uniform distribution to a uniform one; however, if the true event plane distribution is non-uniform then forcing the measured distribution to be uniform produces a systematic offset.

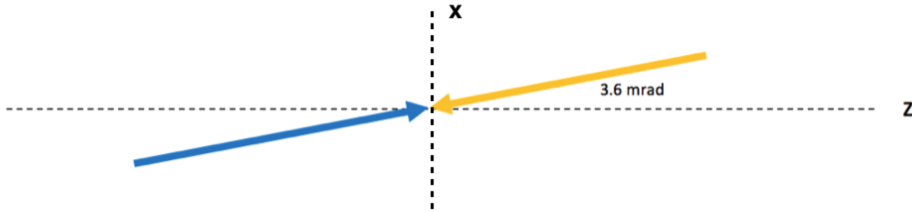


Figure 4.10: Diagram illustrating the angle at which the yellow and blue beams collide relative to the longitudinal  $z$ -axis of the detector. The yellow beam corresponds to the Au (south-going) beam, and blue corresponds to the proton (north-going) beam. Due to the nature of running  $p$ +Au collisions at  $\sqrt{s_{NN}} = 200$  GeV at RHIC, the beams collide at an angle of 3.6 mrad.

We correct for the offset of the collision vertex by shifting the origin of the PHENIX global coordinate system to the true collision vertex. To correct for the effect of the beam angle, we apply a global rotation of the PHENIX coordinate to align its longitudinal axis with that of the beams. In practice, these transformations are accomplished by individually applying a global rotation and translation to every CA track, FVTX cluster, and BBC PMT.

As shown in Figure 4.11, applying these corrections prior to calculating  $v_2$  reduces the magnitude of the east-west discrepancy. The new  $R_{v_2^{\text{FVTXS}}} = 1.43$ , and  $R_{v_2^{\text{BBCS}}} = 0.66$ , are reduced from the east-west difference measured without any corrections. However, even after rotating the PHENIX global coordinate system to be in alignment with the beam axis when calculating  $\Psi_2$ , there is a residual effect from the beam rotation, which still affects the  $v_2$  measurement.

To explain this effect, consider a cylindrical disk with a hole in the middle, centered about the  $z$ -axis (in analogy to the shape of the FVTX and the BBC), as shown in the left plot of Figure 4.12. In this geometry, all points along a ring of constant radius are at the same pseudorapidity. However, if one were to tilt that disk, the pseudorapidity of points along that ring would be  $\phi$  dependent. The tilt of the disk changes its pseudorapidity acceptance and its extent. Now consider that it is not the disk that is tilted but rather the beam orientation that is tilted. The previous statements about the effect on the  $\eta$  range being  $\phi$  dependent still apply.

The combination of the  $\eta$  acceptance changing and the  $\eta$  distribution of charged particles

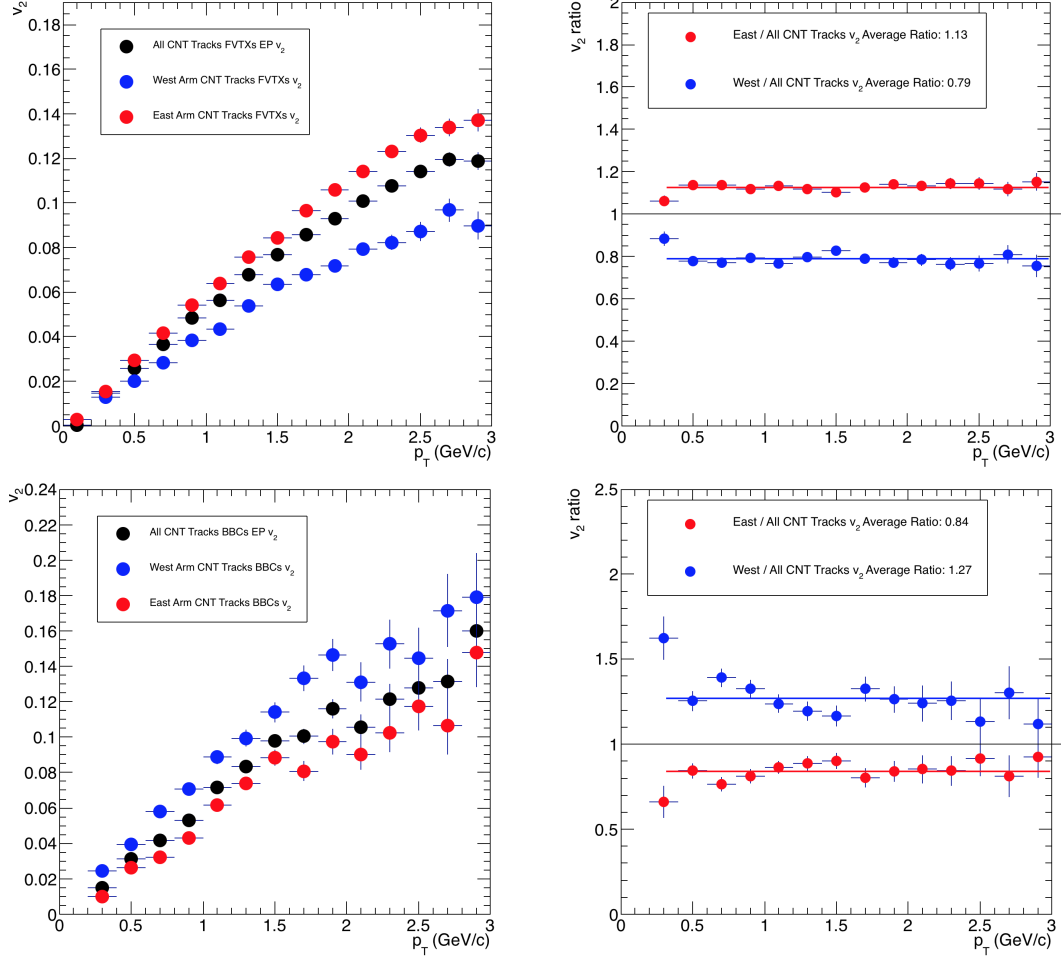


Figure 4.11: A corrected measurement of  $v_2(p_T)$  with the FVTXS (top two panels) and the BBCS (bottom two panels) event plane for the  $p+Au$   $\sqrt{s_{NN}} = 200$  GeV. The default resolution as shown in Table 4.4 is used. The plotting conventions are the same as described in the caption of Figure 4.9.

not being flat means that the average number of charged particles going through the disk would be systematically  $\phi$  dependent, as illustrated in Figure 4.12 (right). If the average charged particle distribution is not uniform in  $\phi$ , the event plane distribution will not be either. This results in the flattening procedure creating systematic effects such as the east-west  $v_2$  asymmetry.

In order to correct for this effect, an additional weight factor is introduced for FVTX clusters and BBC PMTs during the event plane calculation. This factor is such that hits in  $\phi$  regions with systematically fewer particles are given a larger weight, and correspondingly, hits in  $\phi$  regions with systematically more particles are weighted less. The introduction of this weighting as defined below

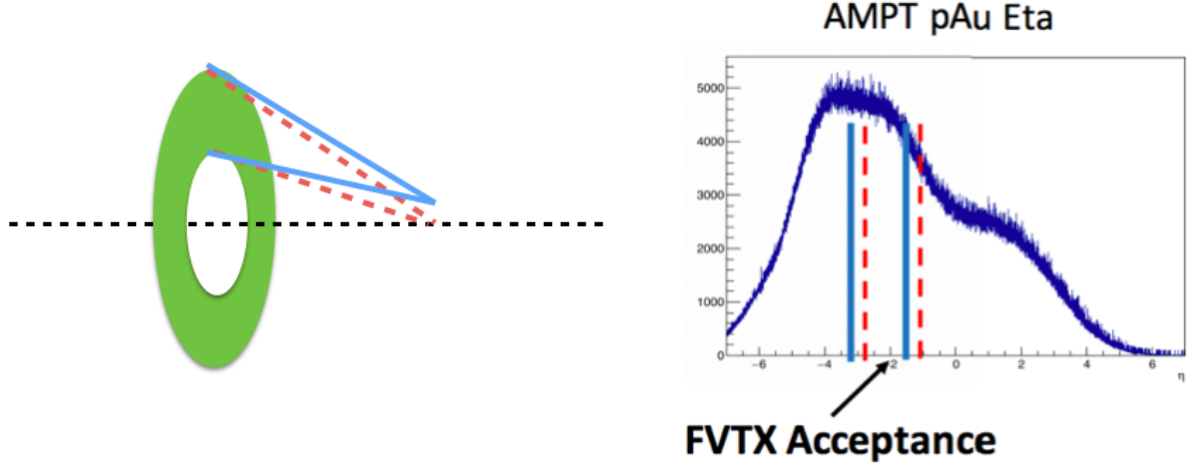


Figure 4.12: (left) Cartoon diagram illustrating  $\eta$  acceptance shift due to a beam offset in one of the FVTXS layers. (right) Pseudorapidity distribution of charged particles from the AMPT Monte Carlo generator for  $p+Au$   $\sqrt{s_{NN}} = 200$  GeV, showing the shift in  $\eta$  acceptance.

does not formally change the event plane calculation, as a weight factor is already implemented in its construction. The modified weight factor is:

$$w_i = w_i^D F(\phi, z_{\text{vertex}}) \quad (4.15)$$

where  $w_i^D$  is the default weighting associated with the detector element, and  $F(\phi, z_{\text{vertex}})$  is the multiplicative weighting to correct for the beam geometry.  $F(\phi, z_{\text{vertex}})$  is dependent on  $z_{\text{vertex}}$ , in addition to  $\phi$ , because  $\eta$  is dependent on the collision vertex.

#### 4.4.1 Analytic Correction Method

One can analytically calculate this  $\phi$  dependent weight factor using the geometry of the FVTXS and BBCS as well as using the  $\eta$  distribution of charged particles. Unfortunately, the  $\eta$  distribution of charged particles in  $p+Au$   $\sqrt{s_{NN}} = 200$  GeV has not been measured by an experiment, so we must rely on models that cannot be fully checked. We can simulate 0–2 fm impact parameter  $p+Au$  at  $\sqrt{s_{NN}} = 200$  GeV events in AMPT and determine the simulated  $dN_{ch}/d\eta$  as shown in the right panel of Figure 4.12.

The left panel of Figure 4.13 shows the  $\phi$  dependence of the  $\eta$  acceptance with a beam angle

(solid line) and without a beam angle (dotted line). By taking the ratio of the  $\eta$  acceptance with a beam angle to the  $\eta$  acceptance without a beam angle, for each  $\phi$  angle we calculate the correction factor shown in the right panel of Figure 4.13. This correction factor is the multiplicative weight factor  $w_i$  as defined in the previous section.

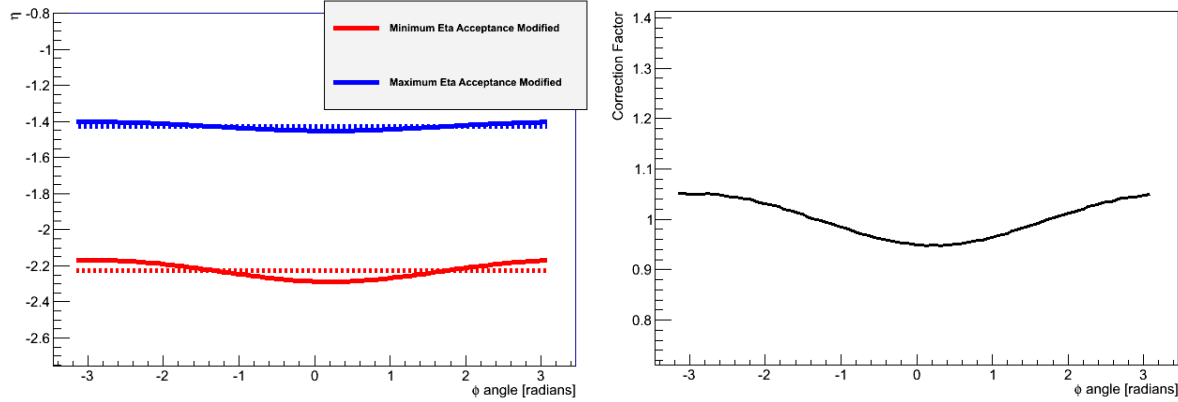


Figure 4.13: The modification of the  $\eta$  acceptance as a function of  $\phi$  for the FVTX first layer (left) and the calculated correction factor from this modification (right).

#### 4.4.2 FVTX Inverse Phi Weighting

Another way to determine the weight factor is to use a data driven method of measuring the extent to which each  $\phi$  region in a detector has systematically more or less particles. Then an inverse weighting based on this measurement is applied to the  $\phi$  regions to correct the  $\phi$  distribution of the detector to uniformity.

For the FVTX implementation of this, first the rotation and offset correction are applied. Then, the weight factor is determined by plotting all hits in a cylindrical disk detector vs  $\phi$ , normalizing this distribution to one, and then inverting it. Applying this weight factor to the data will produce uniform hit distributions in  $\phi$  in each of the detectors to which it is applied. This will, in turn, make the event plane distribution more uniform when measured in those detectors, thus correcting for the effect. The added benefit of using this method is that it also corrects for efficient and inefficient  $\phi$  regions in the detector. In order to get rid of significant hot or cold  $\phi$  regions,

$\phi$  regions with weight factors greater than 1.5 or less than 0.5 are set to 0.0. This correction is done for each FVTX layer, in  $z$ -vertex bins, and on a run-by-run basis. The multiplicative weight function  $F(\phi, z_{\text{vertex}})$  for the FVTX disks is defined as

$$F(\phi, z_{\text{vertex}}, \text{layer}) = \frac{\langle N_{\text{cluster}}(z_{\text{vertex}}, \text{layer}) \rangle}{N_{\text{cluster}}(\phi, z_{\text{vertex}}, \text{layer})}, \quad (4.16)$$

where  $N_{\text{cluster}}(\phi, z_{\text{vertex}}, \text{layer})$  is the number of FVTX clusters as a function of  $\phi$ ,  $z_{\text{vertex}}$ , and FVTX layer and  $\langle N_{\text{cluster}}(z_{\text{vertex}}, \text{layer}) \rangle$  is the  $\phi$  average of the number of clusters. The weighting can be seen in Figure 4.14. A comparison between the FVTX weighting and the analytic correction is shown in Figure 4.15. The good agreement indicates the validity of the weighting.

#### 4.4.3 BBC Charge Weighting

For the BBC, we used another data driven method to correct for the non-uniform particle distribution. Using the distribution of particles in the BBC from the 2015  $p+p \sqrt{s} = 200$  dataset as a baseline, we applied an inverse weighting much like the method described in the previous section. In the  $p+p$  dataset, there was no issue with beams colliding at an angle and the average charge across all 64 PMTs in the BBCS is uniform. In this method, the multiplicative weight function  $F(\text{PMT}, z_{\text{vertex}})$  for the BBCS is defined as:

$$F(\text{PMT}, z_{\text{vertex}}) = \frac{\langle N_{\text{Charge}}^{p+p}(z_{\text{vertex}}) \rangle}{\langle N_{\text{Charge}}^{p+\text{Au}}(\text{PMT}, z_{\text{vertex}}) \rangle}, \quad (4.17)$$

where  $\langle N_{\text{Charge}}^{p+p, p+\text{Au}}(\text{PMT}, z_{\text{vertex}}) \rangle$  is the event averaged charge as a function of PMT and  $z_{\text{vertex}}$  for the  $p+p$  and  $p+\text{Au}$  datasets, respectively. This weight function is shown in Figure 4.16 and is applied directly to the event plane calculation using Equations 4.9 and 4.15. Although the weight function could be defined as a function of  $\phi$  like in the FVTX case, the positions of the PMTs in the BBC are fixed and it is more direct to take the ratio between PMTs.

One effect of using this weighting method is that it will make the distribution of particles in the BBC in  $\phi$  and  $\eta$  uniform. This can be illustrated by looking at Figure 4.17. It is apparent that the  $p+p$  average charge is much more uniform than the  $p+\text{Au}$  average charge as a function of  $\phi$  and

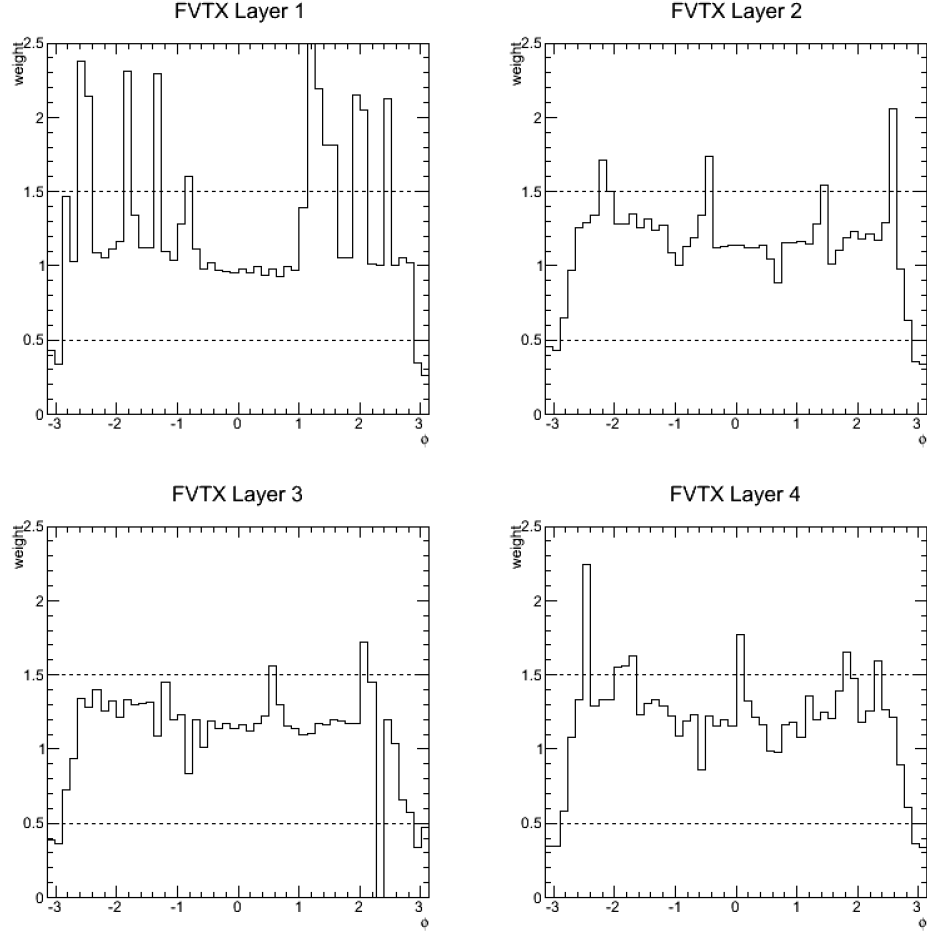


Figure 4.14: These four panels show the FVTX  $\phi$  dependent cluster weighting when calculating the FVTX event plane for each layer separately for events when a collision vertex in  $z$  is around 0. There are some  $\phi$  regions where weight factor is outside of the dotted line bounds. This indicates that either there was a severe deficit or excess of clusters measured in the region. Later, we will examine the effect of keeping these regions or cutting them out on the  $v_2$  measurement.

ring. After applying the  $p+p/p+\text{Au}$  ratio weighting, which is essentially dividing the left plot by the right plot in Figure 4.17, the PMT charges in ring 1 for the  $p+\text{Au}$  dataset will be deweighted so that their corrected average charge will be uniform in  $\phi$ , and in agreement with the average charge for the other rings. If all the BBC rings have the same average charge, this means that the average charge as a function of  $\eta$  for the BBC will be approximately uniform. This is one reason why this method ( $p+p/p+\text{Au}$  ratio weighting) is preferred for the BBC, because the variations in the average charge between the rings are normalized. One could apply the FVTX method of inverse  $\phi$

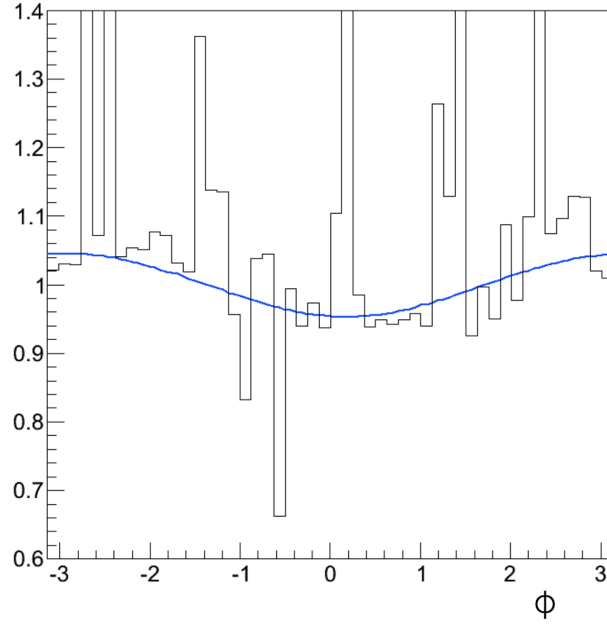


Figure 4.15: The black is the FVTX weighting and the blue is the analytic weighting. They have good agreement.

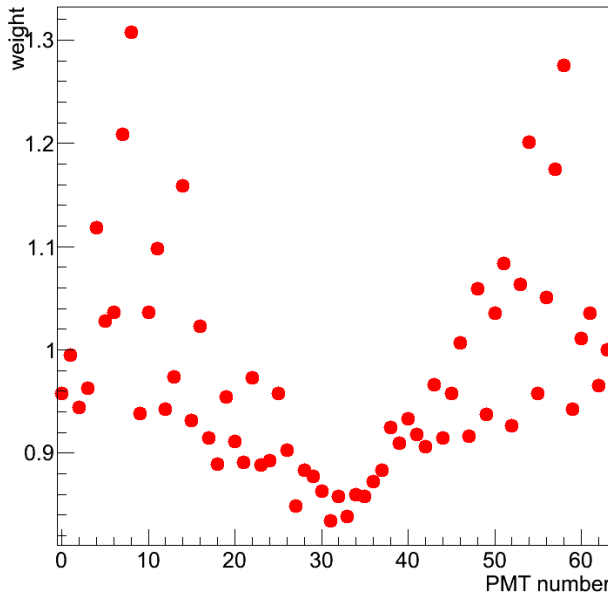


Figure 4.16: Shown here is BBC the multiplicative weight factor  $F$  used when calculating the modified event plane for events where the collision vertex in  $z$  is around 0. The  $y$ -axis is the weight factor and the  $x$ -axis is the PMT number for the BBCS (there are 64 total in the BBCS).

weighting by inverting the right plot of Figure 4.17 to find the weight function. However, although

using only the  $p$ +Au dataset would normalize the average charge as a function of  $\phi$ , it would not normalize the charge as a function of  $\eta$ . Both methods are applied to the data and shown in the next section.

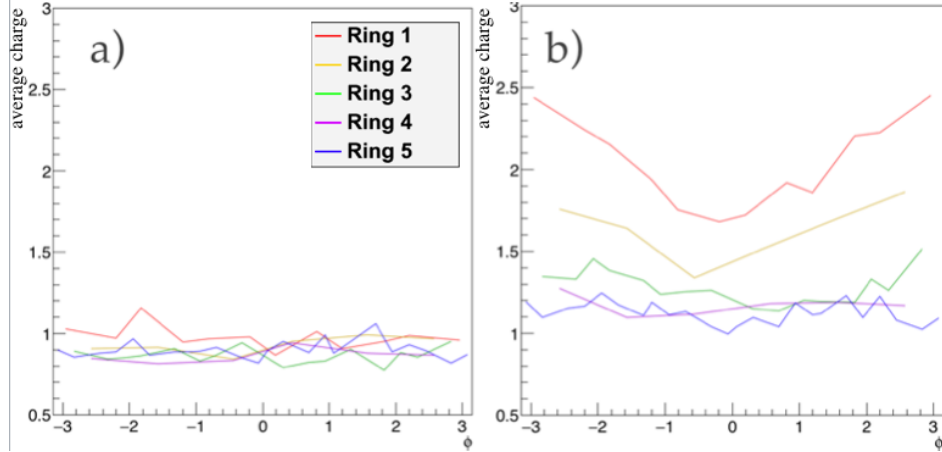


Figure 4.17: These plots depict the average PMT charge per event versus  $\phi$  in the a) the  $p+p \sqrt{s} = 200$  GeV and b)  $p+Au \sqrt{s_{NN}} = 200$  GeV. The PMTs are separated by color, which corresponds to the rings of approximate common radius as shown in Figure 4.6. The left plot shows near uniformity as a function of  $\phi$  and ring. However, the right plot shows a significant deviation from uniformity especially for the innermost rings (rings 1 and 2). In addition to the  $\phi$  variation for the right plot, the innermost rings have the largest average charge when compared to the other rings. This is in part due to the fact the innermost rings cover a slightly larger  $\eta$  range. However, the innermost rings in the left plot also cover the largest  $\eta$  range and do not exhibit this separation in rings.

#### 4.4.4 Applying Weighting to $v_2$

The previously discussed corrections are applied when calculating the raw  $\Psi_2^{\text{FVTXS}}$  used in the  $v_2$  measurement. Shown in Figure 4.18 is the correction summary for the FVTXS  $v_2$  measurement where  $R_{v_2^{\text{FVTXS}}}$  is the y-axis. The first column, which corresponds to  $R_{v_2^{\text{FVTXS}}}$  calculated using FVTXS layers 1, 2, and 4, with layer 3 being excluded, is explained shortly. The black, red, blue, and green points correspond to no weighting, analytic weighting, inverse  $\phi$  weighting, and inverse  $\phi$  weighting with cuts, respectively. Compared to the  $R_{v_2^{\text{FVTXS}}}$  calculated with no weighting,  $R_{v_2^{\text{FVTXS}}}$  calculated with each of the corrections brings the ratio quantity closer to 1.0, indicating the weighting techniques are working. In order to better understand the effect of the corrections,

$R_{v_2^{\text{FVTXS}}}$  is measured separately with each FVTXS layer. The rationale for this exclusion is due to FVTXS layer 3's unusual behavior in relation to the other FVTXS layers. As we go from layer 1 to layer 4, the  $R_{v_2^{\text{FVTXS}}}$  generally is trending downward except for layer 3. Although the reason for this was never definitively determined, it is likely there is some issue with the layer data due to electronic or detector problems. Thus, the measurement of  $v_2^{\text{FVTXS}}$  is calculated without any clusters in the third layer.

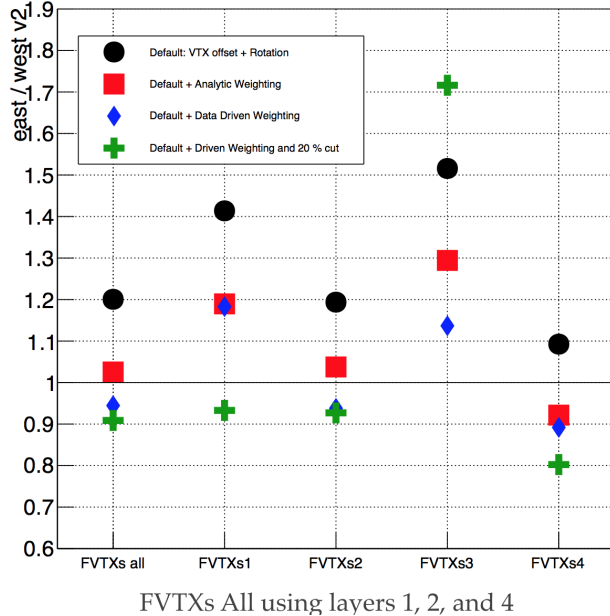


Figure 4.18: Plotted is the FVTXS correction summary where the y-axis is the east/west  $v_2$  ratio and the x-axis is the different subset of clusters used to calculate the  $v_2$ . The black markers correspond to the default corrections. The red boxes correspond to the corrections with the analytic weighting shown in Figure 4.13. The blue diamonds are the FVTX inverse  $\phi$  weighting as shown in section 4.4.2. Finally, the green crosses correspond to the same as the blue diamonds except an additional hot-cold filter of 20% was applied. The first column is using all the FVTXS layers except for the 3rd layer (explained in the text). So the first columns should be approximately the average of columns 2, 3, and 5. Columns 2 through 5 show the ratio calculated from clusters only in that layer.

Similarly, Figure 4.19 is the correction summary for the BBCS  $v_2$  measurement where  $R_{v_2^{\text{BBCS}}}$  is the y-axis. The first column corresponds to  $R_{v_2^{\text{BBCS}}}$  calculated using all five BBCS rings. Compared to the  $R_{v_2^{\text{BBCS}}}$  when calculated with no weighting,  $R_{v_2^{\text{BBCS}}}$  when calculated with the data driven and  $p+p/p+\text{Au}$  ratio weighting is modestly closer to 1.0. By looking at  $R_{v_2^{\text{BBCS}}}$  calculated

with PMTs in individual BBCS rings for the weighted points,  $R_{v_2^{\text{BBCS}}}$  is generally trending downward as a function of ring number. Applying the weighting corrections to  $R_{v_2^{\text{BBCS}}}$  calculated by ring 1, the innermost ring, over-corrects  $R_{v_2^{\text{BBCS}}}$ . This may be explained by the fact that ring 1 covers the largest  $\eta$  acceptance range, causing the correction to be inconsistent. The reason ring 1 is not excluded from the inclusive  $v_2$  calculation, like the FVTXS layer 3 is excluded, is because there is no reasonable justification to exclude it other than its over-corrected  $R_{v_2^{\text{BBCS}}}$  values. While FVTXS layer 3 breaks the trend of  $R_{v_2^{\text{FVTXS}}}$  decreasing, BBCS ring 1 follows the  $R_{v_2^{\text{BBCS}}}$  ring trend. See appendix A for the full  $v_2(p_T)$  measurements for each event plane detector, each correction, and each layer or ring.

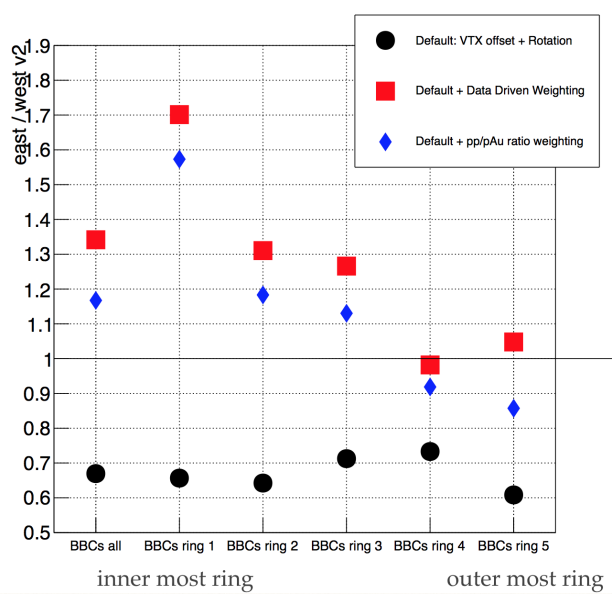


Figure 4.19: Plotted is the BBC correction summary where the y-axis is the east/west  $v_2$  ratio and the x-axis is the different subset of PMTs used to calculate the  $v_2$ . The black markers correspond to the default corrections. The red boxes correspond to the corrections with the analytic weighting shown in Figure 4.13. Finally, the blue diamonds correspond to the BBC inverse  $\phi$  charge weighting as shown in Section 4.4.3. The first column is the quantity calculated from all PMTs. Columns 2 through 6 are using PMTs from certain rings as defined in Figure 4.6. Ring 1 is the hardest to correct. The first column should approximately be the average of all the other columns.

Figure 4.20 shows the  $v_2(p_T)$  with the inverse  $\phi$  weighting and 20% cut from Figure 4.18. This figure also shows  $v_2(p_T)$  with the pp/pAu ratio weighting from Figure 4.19. Although the east and

west  $v_2^{\text{BBCS}}$  measurements do not collapse together like the east and west  $v_2^{\text{FVTXS}}$  measurements, the result is good enough to be incorporated in our systematics uncertainties. Due to the fact that  $R_{v_2^{\text{FVTXS}}}$  is corrected to within  $\pm 10\%$  and the fact that  $v_2^{\text{FVTXS}}(p_T)$  has a smaller statistical uncertainty, the primary  $v_2(p_T)$  measurement is done using the FVTXS.

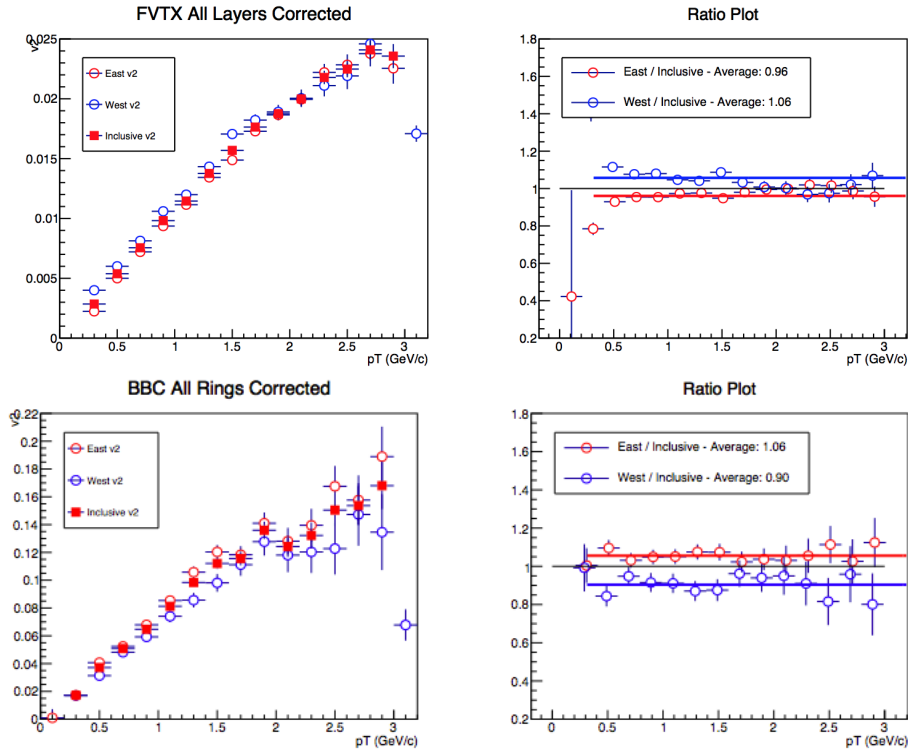


Figure 4.20: FVTXS  $v_2$  event plane measurement corrected with inverse  $\phi$  weighting and 20% cut with FVTXS layer 3 excluded (top) and BBCS  $v_2$  event plane measurement corrected with  $p+p/p+\text{Au}$  ratio weighting (bottom).

In order to estimate the contribution of this systematic uncertainty, we assume the true  $v_2$  value is absolutely bounded between the separate east and west measurements and we assume that the probability distribution for  $v_2$  is uniformly distributed between the upper and lower bounds. Thus, we calculate the point-by-point absolute value of  $v_2^{\text{east}}$  minus the  $v_2^{\text{west}}$  divided by  $\sqrt{12}$ , which is the RMS width of an uniform distribution. By using the best corrected BBCS  $v_2$  measurement in this calculation, we assign a value of 5% for this systematic uncertainty.

## 4.5 Other Sources of Systematic Uncertainty

In this section, other sources of systematic uncertainty are described and the sum of the systematic uncertainties are shown.

### 4.5.1 Effect of Event Pile-Up

Pile-up events occur when there are two or more collisions within the same bunch crossing.

Pile-up events are an issue for this analysis because they:

- (1) are erroneously included into the 0-5% centrality selection due to two low multiplicity collisions looking like a high multiplicity collision,
- (2) and reduce the value of  $v_2$  because the event plane angle from one collision will be different than the event plane angle in the other collision, such that correlations calculated by using particles produced from the two collisions are random and will dilute the real correlations, thereby reducing the flow signal.

In order to filter pile-up events we look at the distribution of BBC PMT timing values as seen in Figure 4.21. A normal event is strongly peaked at 0 while a pile-up event has a broad distribution and may not be centered at 0. We developed an algorithm to efficiently filter pile-up events by analyzing the BBC PMT timing value distribution event by event. When the  $v_2$  values are compared with and without the filter, a difference of 4% is seen.

Pile-up events occur at a rate of 8% in 0-5% central  $p$ +Au collisions. Low-luminosity and high-luminosity subsets of the data were analyzed, and the systematic uncertainty was determined to be  $^{+4\%}_{-0\%}$ , since the  $v_2$  was found to decrease in the events that contain a pile-up as expected.

### 4.5.2 Event Plane Detectors

We expect that the value of  $v_2$  should be consistent when measured in different detectors, after applying corrections. Any remaining difference of  $v_2$  measured independently in the FVTXS

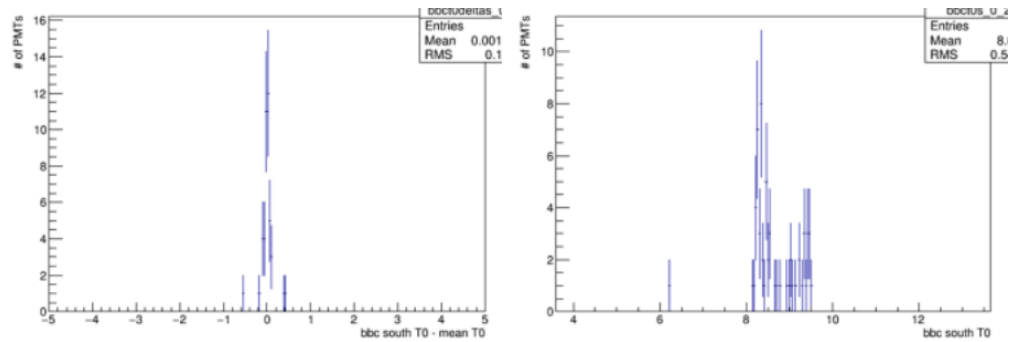


Figure 4.21: The distribution of BBC PMT timing values. The x-axis is the difference between the southern BBC PMT  $t_0$  – the mean  $t_0$  in the south. An example of a normal event (left) and an example pile-up event (right), are shown.

and BBCS indicates a source of systematic uncertainty. The difference is calculated after applying corrections to beam alignment  $v_2$ , as shown in Figure 4.22. The right panel of the figure shows the average difference to be around 0.97. Thus, the systematic uncertainty estimated is  $\pm 3\%$ .

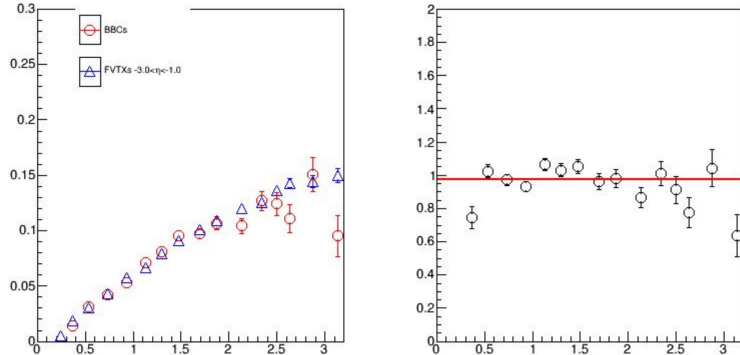


Figure 4.22:  $v_2(p_T)$  measured separately in the BBCS and the FVTXS after beam alignment corrections (left) and the ratio of  $v_2^{\text{FVTXS}}$  to  $v_2^{\text{BBCS}}$  (right). The red line is the average of the ratio across  $p_T$ .

#### 4.5.3 Track Background

The set of tracks that are used in this analysis come from central arm tracks which are known to have a track background of 2.0%. The track background from photonic conversions and weak decays, and mis-reconstructed tracks, which we estimate at 2% relative to  $v_2$  by varying the

windows in the PC3 matching variables from  $3\sigma$  to  $2\sigma$ .

#### 4.5.4 Effects of Non-Flow

As discussed in Chapter 2, non-flow is a catch-all term used to categorize all types of angular correlations which do not arise from hydrodynamic flow and are not related to the initial collision geometry. Non-flow constitutes a significant background to our measurement. There are several known sources of non-flow:

- (1) hard scattering events producing dijets,
- (2) initial state correlations between target and projectile,
- (3) decay chains of exotic particles,
- (4) momentum conservation.

Figure 4.23 shows the characteristic two-particle correlations arising from non-flow associated with dijets. The near-side peak at  $(0,0)$  is from the cone of particles in a single jet all at a similar location in  $\eta$  and  $\phi$ . The away-side ridge around  $\phi = \pi$  originates from particle pairs, where each particle belongs to a different jet. The two jets are completely back-to-back in  $\Delta\phi$ , but have a spread in  $\Delta\eta$ . This correlation function yields a substantial  $c_2$  very similar to that from the hydrodynamic flow signal we are seeking. In order to minimize the contribution of dijet events, the standard flow analysis procedure is to select regions outside of the red dotted lines seen in Figure 4.23 ( $|\Delta\eta| > \eta_{min}$ , where  $\eta_{min}$  is usually on the order of 1.0 units of pseudorapidity).

In order to estimate the degree of presence of non-flow, we can measure the  $c_2$  from  $p+p$  events which should be devoid of any hydrodynamic flow but should have many of the sources of non-flow present. In order to compare  $p+p$  with  $p+Au$ , we must scale-up the  $p+p$  quantity by the dilution factor defined in Equation 4.18. The scaled down reference  $c_2$  is shown as blue squares in Fig. 4.24, panel a). The ratio of  $c_2$  in the scaled-down  $p+p$  reference to that in  $p+Au$  is shown in panel b).

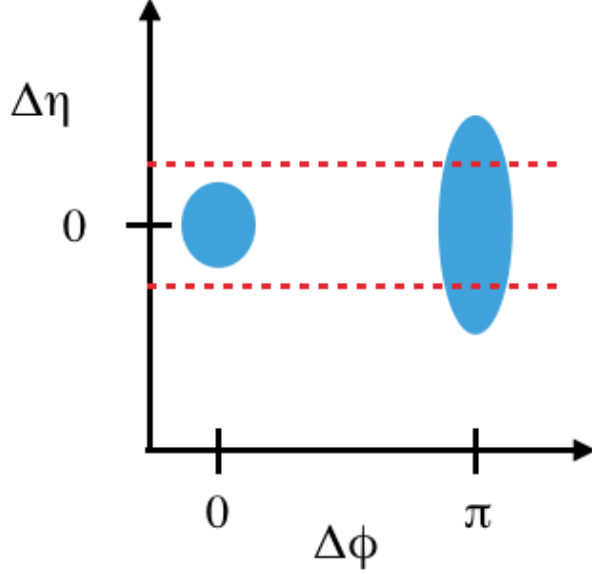


Figure 4.23: 2D profile of a correlation function in  $\Delta\eta\Delta\phi$  space of a dijet event. The area bounded by red dotted lines represents the exclusion zone in  $\Delta\eta$ , such that the measurement is made only using data from outside of the exclusion zone to reduce non-flow contributions.

From this ratio, as calculated in Equation 4.18, it can be seen that the relative correlation strength in  $p+Au$  from elementary processes is at most 23% at the highest  $p_T$ . Since this procedure constitutes an approximation to quantify the non-flow correlation strength, it is not subtracted from the total signal, instead it is treated as a source of systematic uncertainty. Even though the  $p+Au$  and the  $p+p$  baseline data were collected in different years, such that potential changes in detector performance could affect our results, it was verified that using  $p+p$  data from various run periods has an effect of at most 3% on the calculated non-flow contribution. The non-flow correlations which enhance the  $v_2$ , whose contribution we estimate from Figure 4.24, assigning a  $p_T$ -dependent asymmetric uncertainty with a maximum value of  $^{+0}_{-23}\%$

$$c_2^{\text{pAu elementary}}(p_T) \simeq c_2^{p+p}(p_T) \frac{(\sum Q^{\text{BBC-S}})_{p+p}}{(\sum Q^{\text{BBC-S}})_{\text{pAu}}}. \quad (4.18)$$

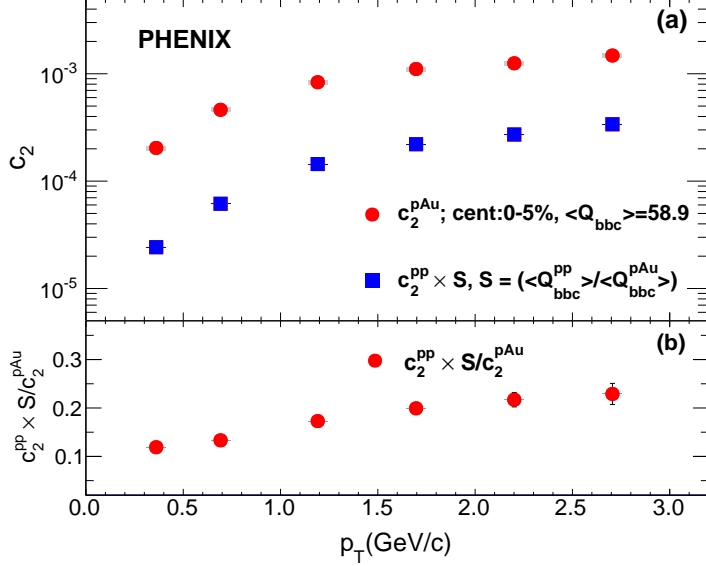


Figure 4.24: (a) The second order harmonic coefficients  $c_2(p_T)$  for long range angular correlations in 0%–5%  $p$ +Au collisions, as well as for minimum bias  $p$ + $p$  collisions. The latter are scaled down by the factor  $(\sum Q^{\text{BBC-S}})_{p+p} / (\sum Q^{\text{BBC-S}})_{\text{pAu}}$ . (b) The ratio of the two harmonics is plotted with the corresponding statistical errors.

## 4.6 Systematic Uncertainties Summary

Table 4.6 summarizes the sources of systematic uncertainty for the  $v_2$  measurement. Each of these systematic uncertainties are categorized by type:

- (1) point-to-point uncorrelated between  $p_T$  bins,
- (2) point-to-point correlated between  $p_T$  bins,
- (3) overall normalization uncertainty in which all points are scaled by the same multiplicative factor.

We total the five sources of systematic uncertainty, by adding them in quadrature. The total systematic uncertainty varies from  $^{+7}_{-13}\%$  at low  $p_T$  to  $^{+7}_{-23}\%$  at high  $p_T$ . Now that the systematic uncertainties have been estimated, we show the  $v_2$  physics result in the next chapter.

Table 4.5: Systematic uncertainties given as a percent of the  $v_2$  measurement. Note that the non-flow contribution is  $p_T$  dependent and the value here quoted corresponds to the highest measured  $p_T$ .

Source	Systematic Uncertainty	Type
Track Background	2%	1
Event Pile-up	$^{+4\%}_{-0\%}$	2
Non-Flow	$^{+0\%}_{-23\%}$	2
Beam Angle	5%	3
Event Plane Detectors	3%	3

## Chapter 5

### Results and Discussion

The  $v_2$  measurement for  $p+\text{Au}$  at  $\sqrt{s_{NN}} = 200$  GeV 0–5% centrality completes the set of flow measurements in the small systems available at RHIC:  $p+\text{Au}$ ,  $d+\text{Au}$ , and  ${}^3\text{He}+\text{Au}$ . The goal of this set of measurements is to determine the effect of varying initial collision conditions on the resulting flow.

#### 5.1 $v_2$ Measurement

The resulting  $v_2$  measurement for  $p+\text{Au}$  at  $\sqrt{s_{NN}} = 200$  GeV 0–5% centrality is shown in Figure 5.1. The systematic uncertainty varies from  ${}^{+7}_{-13}\%$  at low  $p_T$  to  ${}^{+7}_{-23}\%$  at high  $p_T$ , where the asymmetric uncertainty is dominated by non-flow contributions. The fact that the non-flow dominates the systematic uncertainty warrants further discussion on the treatment of non-flow.

##### 5.1.1 Non-flow Contribution

As was discussed in Section 4.4.2, the non-flow systematic uncertainty can instead be thought of as a systematic error that can be corrected for in our measurement. To further explore this non-flow effect, Figure 5.2 shows what the  $p+\text{Au}$  measurement looks like by subtracting the non-flow effect rather than treating it as an uncertainty. Due to non-flow being the dominant source of systematic uncertainty, the corrected  $p+\text{Au}$  points are nearly at the bottom of the systematic uncertainty boxes of the uncorrected points. The substantial changes this correction makes to the  $p+\text{Au}$  points, especially at high  $p_T$ , must be put in context of the field of heavy ion physics. This

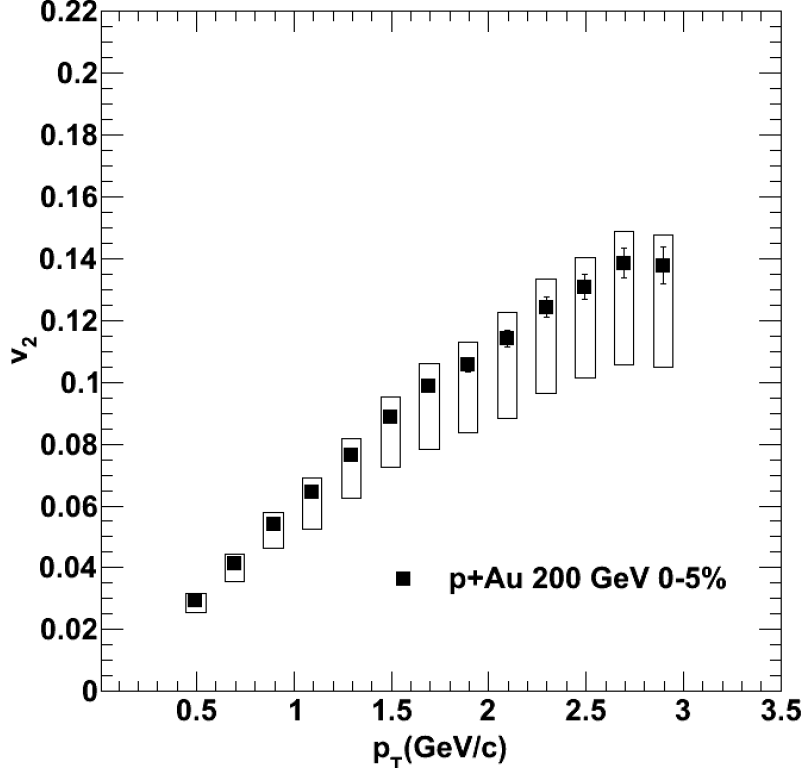


Figure 5.1: The  $v_2$  measurement of  $p+Au$  at  $\sqrt{s_{NN}} = 200$  GeV 0–5% centrality.

procedure to estimate the contribution of elementary processes to the measured  $v_2$  signal is an attempt at an accurate approximation. Although the non-flow approximation used in this thesis has its merits, there is currently no consensus in the field regarding how to properly quantify how much of the  $v_2$  corresponds to “flow” and how much corresponds to “non-flow.” Other experimental collaborations making flow measurements, such as STAR, ATLAS, ALICE, and CMS treat non-flow in different ways [62]. Therefore, we chose to explicitly state our methodology to estimate this non-flow and to treat it as a systematic effect that raises the measured  $v_2$ .

## 5.2 Comparison with Other Species at $\sqrt{s_{NN}} = 200$ GeV 0–5% Centrality

The substantial  $v_2$  in  $p+Au$  at  $\sqrt{s_{NN}} = 200$  GeV is interesting in itself but the significance of the measurement is best understood by comparing it to other small collision system results,

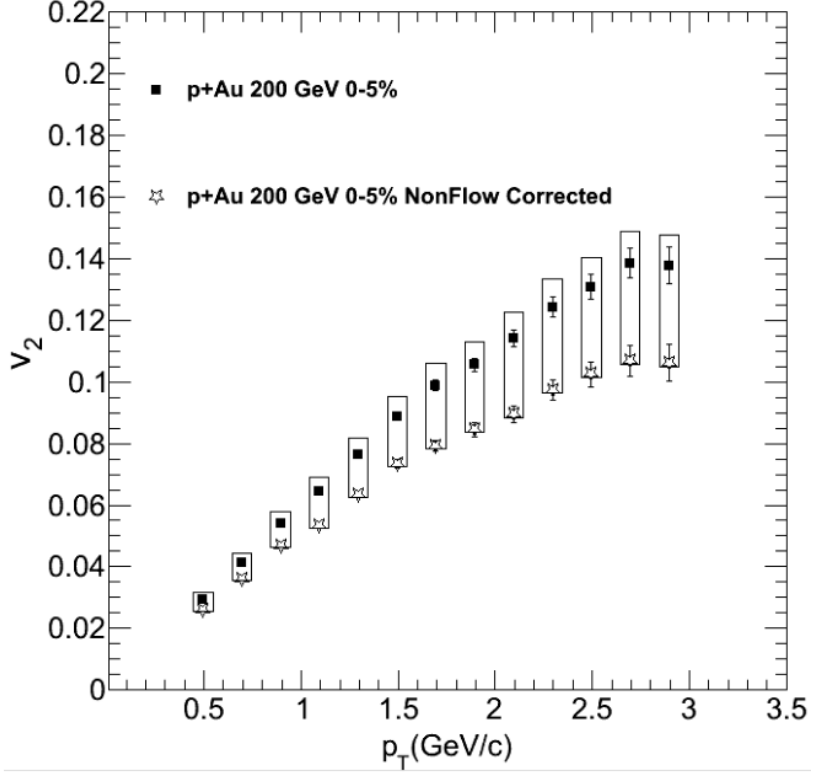


Figure 5.2: The  $v_2$  measurement of  $p$ +Au at  $\sqrt{s_{NN}} = 200$  GeV 0–5% centrality with the statistical and systematic errors corresponding to the bars and the boxes respectively. The stars are the same  $p$ +Au points but with the non-flow estimate subtracted rather than treated as a systematic uncertainty.

specifically  ${}^3\text{He}+\text{Au}$  [23] and  $d+\text{Au}$  [23] at the same  $\sqrt{s_{NN}}$ . In order to properly make the strongest physics statement possible in this comparison, we attempt to hold as many variables constant across all three datasets. Table 5.1 compares the various relevant parameters for the three collision species. As shown in the table, the FVTXs was not used in the  $d+\text{Au}$  measurement unlike for the  $p$ +Au and  ${}^3\text{He}+\text{Au}$  due to the fact that the FVTX was not installed in 2008 when the  $d+\text{Au}$  measurement was taken. The table also highlights the fact that  $dN_{ch}/d\eta$ , the  $\eta$  dependence of the charged particle multiplicity, has not been measured in  $p$ +Au  $\sqrt{s_{NN}} = 200$  GeV, in contrast to  ${}^3\text{He}+\text{Au}$  and  $d+\text{Au}$ . This fact is relevant because mid-rapidity  $dN_{ch}/d\eta$  is an input to the SONIC model for the purposes of multiplicity matching, as discussed in the next section. Among the differences across the columns, the largest is the lack of a non-flow estimate for the  $d+\text{Au}$  dataset. In the

interest of measurement compatibility, and for the reason stated in the previous section, there is no non-flow correction applied to any of the datasets.

Table 5.1: Dataset Variables Comparison listed in order: center of mass energy per nucleon, centrality, mid-rapidity charged particle multiplicity per unit of pseudorapidity from [4], year, trigger (as defined in section 2.2.4) particle sample, trigger particle acceptance, event plane determination,  $\Psi_2$  Resolution, condition of available non-flow estimate.

Variable	$p$ +Au	$d$ +Au	${}^3\text{He}+\text{Au}$
$\sqrt{s_{NN}}$ (GeV)	200	200	200
Centrality	0–5%	0–5%	0–5%
Mid-rapidity $dN_{ch}/d\eta$	N/A	$20.8 \pm 1.5$	$26.3 \pm 1.8$
Year (collected)	2015	2008	2014
Trigger Particle Sample	Charged Hadrons	Charged Hadrons	Charged Hadrons
Trigger Particle Acceptance	$ \eta  < 0.35$	$ \eta  < 0.35$	$ \eta  < 0.35$
Event Plane	$-3 < \eta < -1$ (FVTXs)	$-3.7 < \eta < -3.1$ (MPCs)	$-3 < \eta < -1$ (FVTXs)
$\Psi_2$ Resolution	0.171	0.14	0.274
Non-flow Estimate	yes	no	yes

Figure 5.3 shows the  $v_2(p_T)$  measurements in the three systems. All three measurements exhibit substantial  $v_2$  values that rise as a function of  $p_T$  with a similar shape. Within the error bars of each measurement, the  ${}^3\text{He}+\text{Au}$  and  $d$ +Au measurements agree and the  $p$ +Au measurement is substantially lower. This effect is especially clear at low  $p_T$ , where bulk effects would be most dominant. In order to understand the significance of this set of measurements, comparison to standard theoretical models are useful.

### 5.3 Comparison with Theory

Figure 5.4 shows  $v_2(p_T)$  for the three systems and  $v_2(p_T)$  calculations for each system from the SONIC hydrodynamic model [33], which uses the Monte Carlo Glauber (MC-Glauber) initial conditions and viscous hydrodynamics with  $\eta/s = 0.08$ , and a hadronic cascade temperature of  $T = 170$  MeV. The scale of each collision system in these calculations is taken as charged particle multiplicity at mid-rapidity and the values for 0–5% centrality are 10.0, 20.0, and 27.0, for  $p$ +Au,  $d$ +Au, and  ${}^3\text{He}+\text{Au}$  collisions, respectively [33]. As mentioned above, the  $dN_{ch}/d\eta$  remains un-

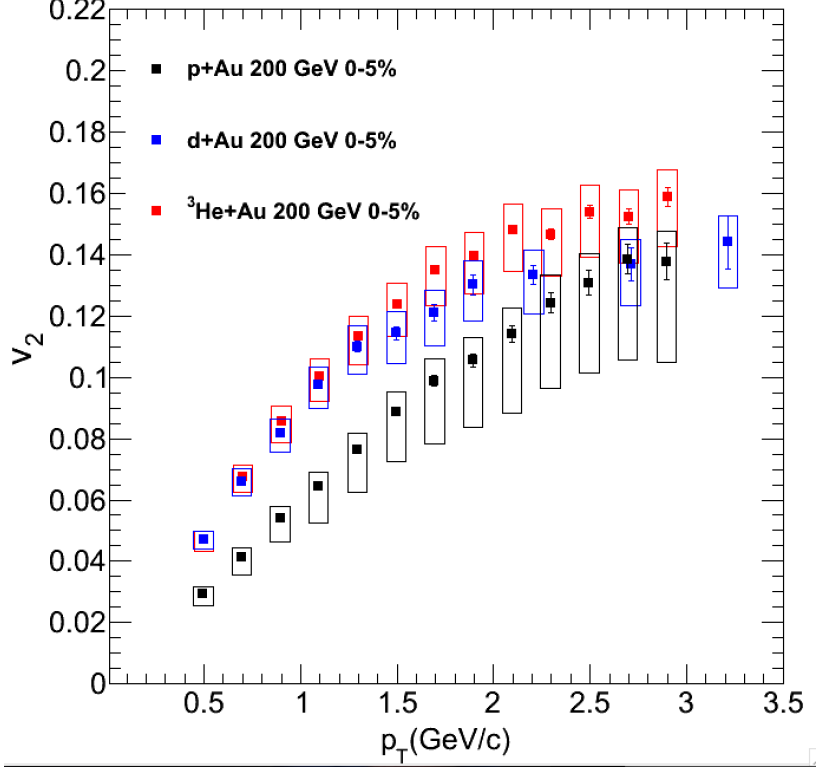


Figure 5.3:  $v_2$  of charged hadrons within  $|\eta| < 0.35$  in 0–5% centrality  $p+\text{Au}$  at  $\sqrt{s_{NN}} = 200$  GeV events compared to the  $v_2$  of charged hadrons in 0–5% centrality  $d+\text{Au}$  and  ${}^3\text{He}+\text{Au}$  events at  $\sqrt{s_{NN}} = 200$  GeV.

measured for  $p+\text{Au}$ ; the 10.0 was obtained by extrapolating from measurements in the other two collision systems [33]. The SONIC calculation incorporates the in the initial collision geometry and the relative medium size for the three systems. For each collision system, there is an excellent agreement within the uncertainties of the measured and the simulated  $v_2$ . This agreement between data and hydrodynamic calculation strongly supports the notion of initial geometry coupled to the hydrodynamic evolution of the medium as a valid framework to understand small system collectivity.

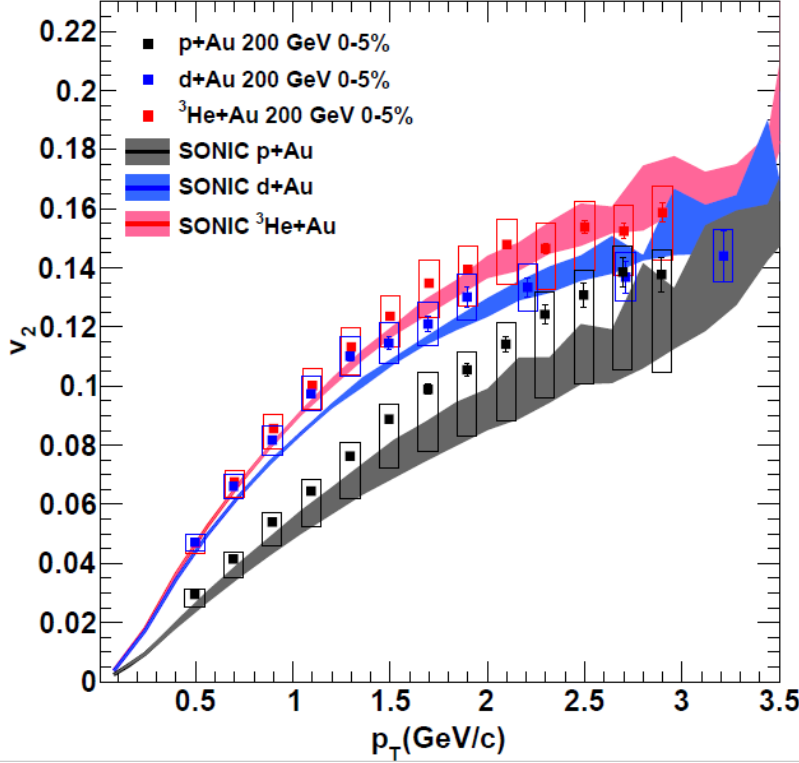


Figure 5.4:  $v_2$  of charged hadrons within  $|\eta| < 0.35$  in 0–5%  $p$ +Au,  $d$ +Au, and  $^3\text{He}$ +Au central collisions, compared to hydrodynamic calculations using the SONIC model, matched to the same multiplicity as the data. Note that the data points shown include non-flow contributions, whose estimated magnitude is accounted for in the asymmetric systematic uncertainties.

### 5.3.1 Initial Conditions and Eccentricity

In order to better understand the comparison of the three systems, a deeper understanding of the initial conditions is warranted. One critical quantity to characterize the initial collision symmetry is known as the eccentricity. As mentioned in Chapter 2, the second order eccentricity,  $\varepsilon_2$ , can be calculated from the distribution of the nucleons involved in the initial collision as:

$$\varepsilon_2 = \frac{\sqrt{\langle r^2 \cos 2\phi \rangle^2 + \langle r^2 \sin 2\phi \rangle^2}}{\langle r^2 \rangle}, \quad (5.1)$$

where  $r$  is the radial nucleon position relative to the centroid of the participants and  $\phi$  is the azimuthal angle of the nucleons [44].

The significance of  $\varepsilon_2$  is that  $v_2$  should be proportional to  $\varepsilon_2$  if the  $v_2$  is primarily from elliptical flow. Table 5.2 shows  $\varepsilon_2$  calculations from the MC-Glauber and IP-Glasma models. The  $\varepsilon_2$  values can be understood by looking at the top three panels of Figure 5.5 which show the spatial distribution of the energy density of the collisions for the  $p+\text{Au}$ ,  $d+\text{Au}$ , and  $^3\text{He}+\text{Au}$  from left to right. It is noteworthy that the eccentricities of  $d+\text{Au}$  and  $^3\text{He}+\text{Au}$  collisions are largely based on relative nucleon orientation, whereas the initial condition of  $p+\text{Au}$  is solely based on the shape of the lone proton projectile and any fluctuations in the target gold nucleus. Table 5.2 illustrates the uniqueness of the  $p+\text{Au}$  system by showing the diverging values of  $\varepsilon_2$  which can be calculated by IP-Glasma and MC-Glauber. Unlike MC-Glauber, IP-Glasma generates very circular initial conditions for  $p+\text{Au}$ , which correspond to very small  $\varepsilon_2$  values. For  $d+\text{Au}$  and  $^3\text{He}+\text{Au}$ , the presence of multiple hot spots wash out differences in single nucleon initial conditions, and thus IP-Glasma and MC-Glauber agree at the 10% level.

While the top three panels of Figure 5.5 are examples of initial energy density distributions for the three systems, the bottom three panels are the energy density distributions of the system after a medium has been formed and time evolved hydrodynamically. For the cases of  $d+\text{Au}$  and  $^3\text{He}+\text{Au}$ , the initial hot spot orientation is translated into an inverted orientation. This is due to the fact that the medium is produced with the highest energy density at places where the expanding hotspots overlap. The expanding hotspots create a substantial final state elliptical flow with an event plane angle relative to the spatial orientation of the initial hotspots. For example, in the  $d+\text{Au}$  collision, the event plane vector is transverse to the line that connects the deuteron's nucleons.

Table 5.2: Initial eccentricity  $\varepsilon_2$  of small systems at  $\sqrt{s_{NN}} = 200$  GeV for 0–5% centrality from MC-Glauber initial conditions smeared with a two-dimensional Gaussian of width  $\sigma = 0.4$  fm, and IP-Glasma initial conditions.

	$p+\text{Au}$	$d+\text{Au}$	$^3\text{He}+\text{Au}$
MC-Glauber $\langle \varepsilon_2 \rangle$	$0.23 \pm 0.01$	$0.54 \pm 0.04$	$0.50 \pm 0.02$
IP-Glasma $\langle \varepsilon_2 \rangle$	$0.10 \pm 0.02$	$0.59 \pm 0.01$	$0.55 \pm 0.01$

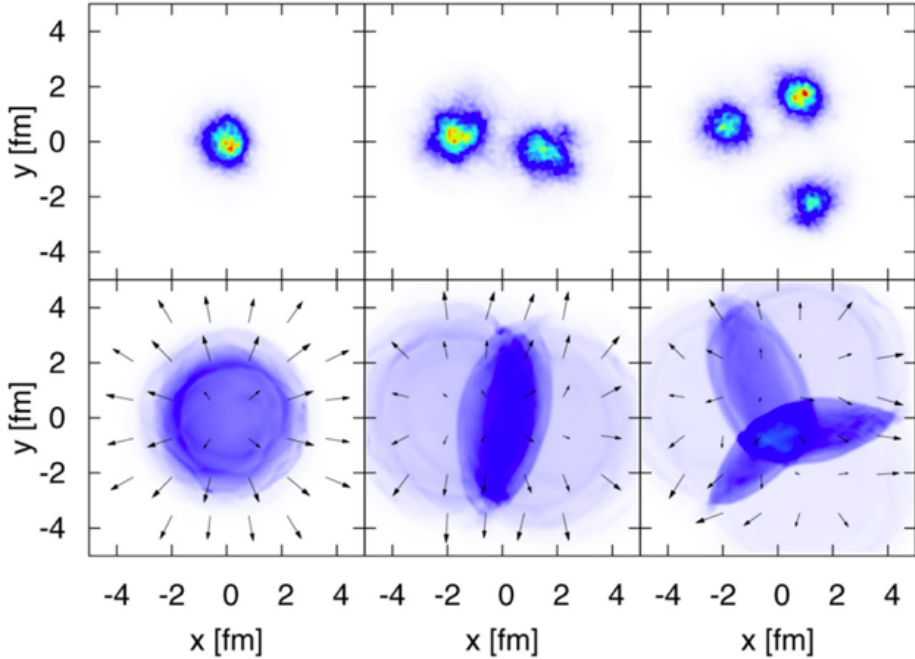


Figure 5.5: The top three panes show the transverse spatial locations of the initial hot spots of the three collision species,  $p+\text{Au}$ ,  $d+\text{Au}$ , and  ${}^3\text{He}+\text{Au}$ , respectively. The bottom three plots show the resulting medium produced from the overlapping hot spots as well as the resulting particle momentum vector field as calculated from a hydrodynamic model, calculation details in [31]

In order to study the effect of initial conditions on our  $v_2$  measurement, the  $v_2$  curves are divided by their corresponding  $\varepsilon_2$  from Table 5.2, with the goal of establishing a scaling between the  $v_2$  and  $\varepsilon_2$ . In ideal ( $\eta/s = 0$ ) hydrodynamics with long lived systems,  $v_2/\varepsilon_2$  should be independent of  $\varepsilon_2$ . Figure 5.6 shows that this ratio is not constant across the three collision systems.

Figure 5.7 gives insight into the relation between initial collision eccentricities, as defined in Equation 5.1, as they are transformed into final state flow. The plot was produced by running many events for  $p+\text{Au}$ ,  $d+\text{Au}$ , and  ${}^3\text{He}+\text{Au}$  systems with different initial spatial distribution smearing (i.e. different  $\varepsilon_2$ ). The final freeze-out hyper-surface of each event is then translated into a distribution of hadrons via the Cooper-Frye freeze-out technique [49]. Figure 5.7 shows the pion  $v_2$  at  $p_T = 1.0$  GeV/c divided by  $\varepsilon_2$  as a function of  $\varepsilon_2$  for each individual  $p+\text{Au}$ ,  $d+\text{Au}$ , and  ${}^3\text{He}+\text{Au}$  event. The figure shows a reasonably common scaling of  $v_2/\varepsilon_2$  for all three systems with

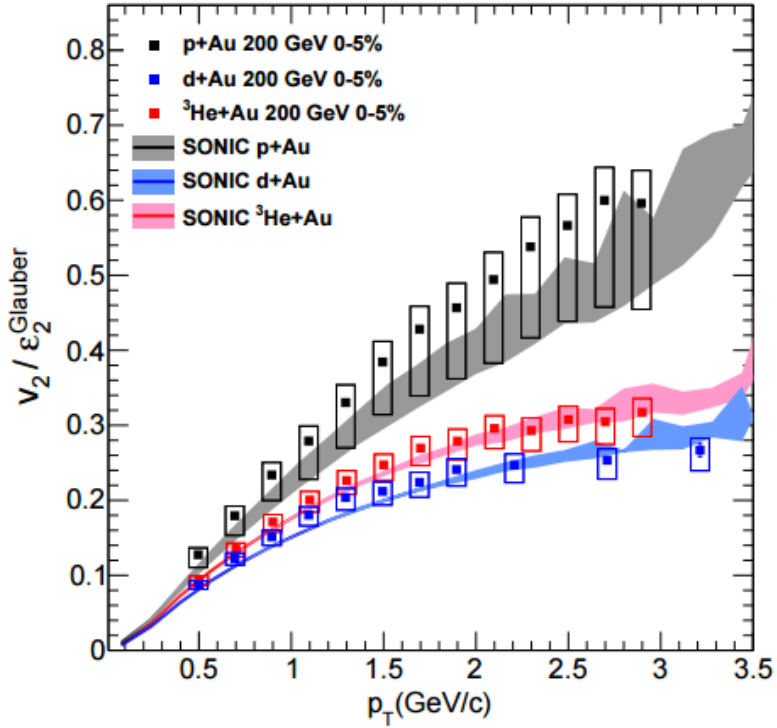


Figure 5.6:  $v_2$  of charged hadrons within  $|\eta| < 0.35$  in 0–5%  $p$ +Au,  $d$ +Au, and  $^3\text{He}+\text{Au}$  central collisions, divided by their corresponding eccentricity  $\varepsilon_2$  from MC-Glauber calculations, compared to SONIC calculations of the same quantity. Note that the data points shown include non-flow contributions, whose estimated magnitude is accounted for in the asymmetric systematic uncertainties.

the  $d$ +Au and  $^3\text{He}+\text{Au}$  simply extending to larger eccentricities. There are a small set of events with very large  $\varepsilon_2$ , but have a rather small final  $v_2$ . Examination of these events reveals them to be  $d$ +Au events where the two hot spots are so far apart that the hydrodynamic fluids never connect during the time evolution, as seen in the overlay in Figure 5.7, therefore produce almost no elliptic flow. There are fewer  $^3\text{He}+\text{Au}$  in this category, seen where two nucleons are very close and the third is quite far away, again having the same effect.

Although MC-Glauber and IP-Glasma are the established models for calculating initial conditions in this context, new models for calculating the initial conditions are promising. There exists a model for initial conditions that includes more degrees of freedom by modifying the MC-Glauber approach to additionally incorporate collisions between constituent quarks increasing the granular-

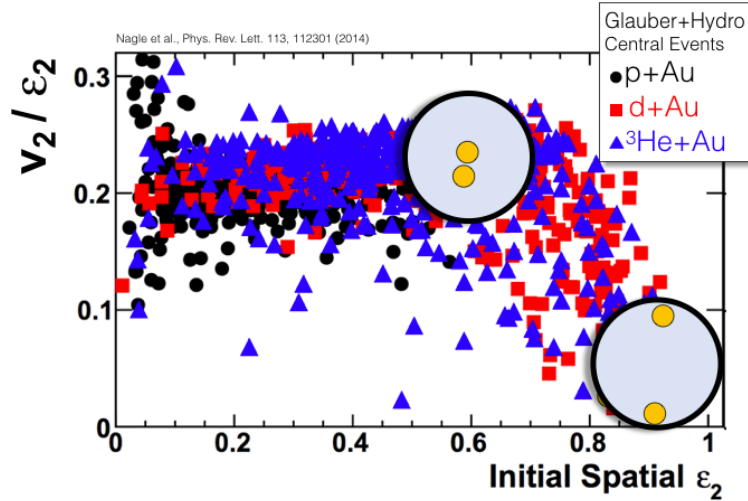


Figure 5.7:  $v_2/\varepsilon_2$  versus  $\varepsilon_2$  with the flow coefficient for pions evaluated at  $p_T = 1.0$  GeV/c from  $p$ +Au,  $d$ +Au, and  $^3\text{He}$ +Au central ( $b < 2$  fm) events (which roughly corresponds to 0–5% centrality). The results are with input parameters  $\eta/s = 1/4\pi$  and initial Gaussian smearing  $\sigma = 0.4$  fm and a freeze-out temperature of  $T_F = 150$  MeV. Diagrams of two possible  $d$ +Au initial configurations are overlayed on top of the plot. Increasing distance between the two  $d$ +Au nucleons correspond to a larger  $\varepsilon_2$  [1].

ity of the simulation [63]. In the rightmost panel of Figure 5.8, the initial eccentricities  $\varepsilon_2$  in  $p$ +Au,  $d$ +Au, and  $^3\text{He}$ +Au, obtained by incorporating constituent quarks, in addition to multiplicity fluctuations, are found to be  $\varepsilon_2 = 0.42$ ,  $0.54$ , and  $0.54$ , respectively. The  $\varepsilon_2$  of  $d$ +Au and  $^3\text{He}$ +Au systems show minimal sensitivity to the incorporation of constituent quarks and multiplicity fluctuations. However,  $p$ +Au has a substantially larger  $\varepsilon_2$  than in the models shown in Table 5.2 when accounting these effects. Another attempt at the calculation incorporating constituent quarks and multiplicity presents calculations in which lower value of  $\varepsilon_2 = 0.34$  is obtained for  $p$ +Au [32]. This result shows that when compared to the MC-Glauber  $\varepsilon_2$  for  $p$ +Au in Table 5.2, quark-level degrees of freedom and multiplicity fluctuations may both play a significant role. In addition to the constituent MC Glauber, it is worth mentioning that an intriguing method for understanding the initial conditions in  $p$ +Au comes from event-by-event fluctuations of the shape of the proton, as described in Ref [64].

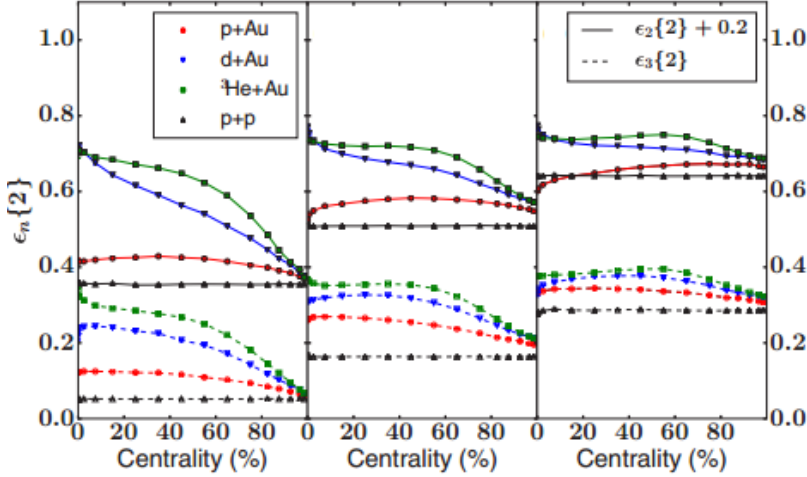


Figure 5.8: Centrality dependence of  $\varepsilon_2$  calculated in a variety of small collision systems with a variety of models for collision detection [disklike (left), Gaussian (middle), quark-subdivided nucleons with  $\sigma_g = 0.3$  fm (right)] [32].

### 5.3.2 Comparison to Alternative Models

Although hydrodynamic models like SONIC, that incorporate MC-Glauber plus relativistic hydrodynamics, are the standard in which elliptical flow is understood in the field of heavy ions, it is important to test the consistency of other models with our data. Figure 5.9 depicts the measured  $v_2(p_T)$  data curves with four different model comparisons. Theoretical predictions were available at the time of measurement, specifically from hydrodynamics with MC-Glauber initial conditions (SONIC [65] and SuperSONIC [52]), hydrodynamics with IP-Glasma initial conditions [31], and A-Multi-Phase-Transport Model (AMPT) [53]. The SuperSONIC model uses the same technique for initial conditions, hydrodynamic expansion, and hadronic cascade as SONIC, yet additionally incorporates pre-equilibrium dynamics with a calculation in the framework of the AdS/CFT correspondence [66].

As mentioned in Chapter 2, calculations using IP-Glasma initial conditions with viscous hydrodynamics describe collectivity in large collision systems, so it is reasonable to apply IP-Glasma to  $v_2$  in small systems. For the model of IP-Glasma+Hydro, in the case of  $d+Au$  and  $^3He+Au$ , a better agreement with data can be achieved by modifying the value of  $\eta/s$ . However,

doing so would lower the prediction for  $p+\text{Au}$  even further. This demonstrates that IP-Glasma does not produce the correct initial conditions which are consistent to measured  $v_2$  via hydrodynamic flow.

SONIC and SuperSONIC both agree well with the data of all three systems. As mentioned above, the agreement of hydrodynamic models supports the idea of initial geometry as the driver of the  $v_2$  signal. Additionally, the three different initial geometries provided by the datasets are useful in constraining the parameters in the SONIC and SuperSONIC models such as  $\eta/s$ , the transition temperature to a hadron cascade, and the MC-Glauber smearing of nucleon coordinates of  $\sigma = 0.4$  fm.

The last model to consider is AMPT, which is as described in Chapter 2. AMPT events with impact parameter  $b < 2$  have a midrapidity  $dN_{ch}/d\eta = 8.1, 14.8$ , and  $20.7$  for  $p+\text{Au}$ ,  $d+\text{Au}$ , and  ${}^3\text{He}+\text{Au}$ , respectively. AMPT uses the same MC-Glauber initial conditions used to characterize event geometry as in SONIC or SuperSONIC. However, AMPT makes use of the initial MC-Glauber geometry information to compute  $v_2$  relative to the participant plane [67]. Elliptic flow calculations from AMPT events agree reasonably well with the data below  $p_T \approx 1$  GeV/c, yet under predict them at higher  $p_T$ . Although AMPT does not describe the data as well as SONIC, AMPT does describe the data of a variety of systems at RHIC and the LHC [68].

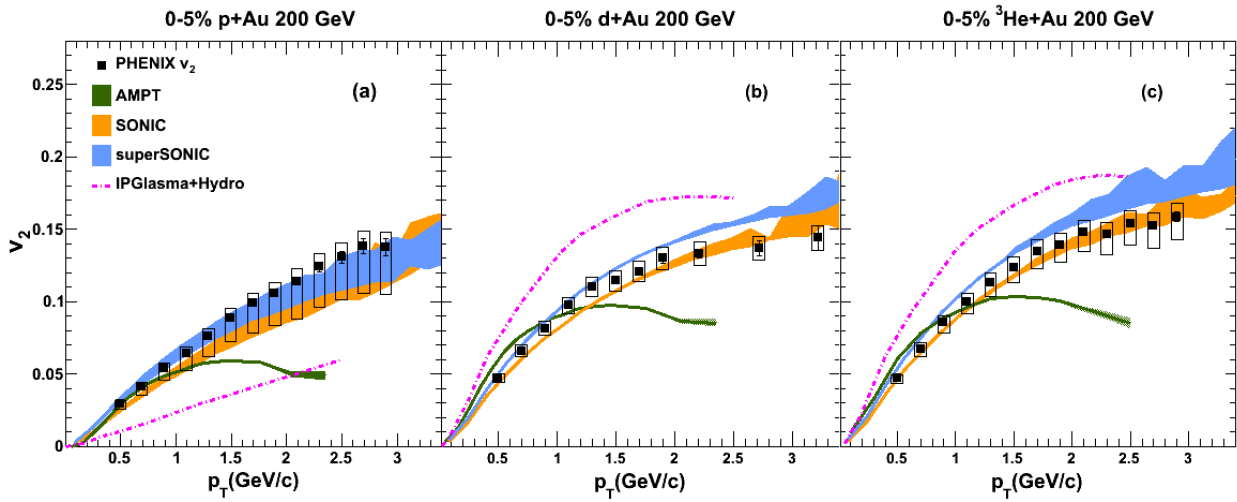


Figure 5.9: Transverse momentum dependence of  $v_2$  in central 0–5% (a)  $p$ +Au, (b)  $d$ +Au, and (c)  ${}^3\text{He}$ +Au collisions at  $\sqrt{s_{NN}} = 200$  GeV. Theoretical calculations from AMPT, SuperSONIC, and IP-Glasma+Hydro are shown in each panel. Note that the data points shown include non-flow contributions, whose estimated magnitude is accounted for in the asymmetric systematic uncertainties.

## Chapter 6

### Summary and Outlook

In this thesis, we have measured the elliptic flow in 0–5% centrality  $p$ +Au collisions at  $\sqrt{s_{NN}} = 200$  GeV. The elliptic flow is quantified by measuring the second-order flow coefficient  $v_2$  defined as:

$$v_2 = \frac{\langle \cos 2(\phi - \Psi_2) \rangle}{\text{Res}(\Psi_2)}, \quad (6.1)$$

where  $\phi$  is the azimuthal angle of charged hadrons at mid-rapidity,  $\Psi_2$  is the second-order event plane determined at backwards rapidity (Au-going direction), and  $\text{Res}(\Psi_2)$  is the event plane resolution. This procedure is detailed in Section 4.2.1.

The measurement of  $v_2(p_T)$ , as a function of transverse momentum, in 0–5% centrality  $p$ +Au at  $\sqrt{s_{NN}} = 200$  GeV collisions completes a set of measurements with engineered initial geometries at RHIC, including the  $p$ +Au,  $d$ +Au, and  ${}^3\text{He}+\text{Au}$  as shown in Figure 6.1. Sources of systematic uncertainty have been described in detail in Chapter 4, Section 4.5, with the non-flow being the dominant source of systematic uncertainty. The measured  $v_2(p_T)$  in  $p$ +Au at  $\sqrt{s_{NN}} = 200$  GeV is in agreement with Monte Carlo Glauber initial conditions plus relativistic hydrodynamics (SONIC), as also shown in Figure 6.1. The agreement of  $v_2$  with a hydrodynamic model is an indication that the initial state geometry becomes transformed into a final state momentum anisotropy in 0–5%  $p$ +Au at  $\sqrt{s_{NN}} = 200$  GeV collisions.

In order to properly compare the  $v_2$  of  $p$ +Au,  $d$ +Au, and  ${}^3\text{He}+\text{Au}$  at  $\sqrt{s_{NN}} = 200$  GeV for each system, we have compared the average second-order eccentricity  $\varepsilon_2$  of the initial collision, as defined in Section 5.3.1. If the measured  $v_2$  is primarily from hydrodynamic flow, i.e. minimal levels

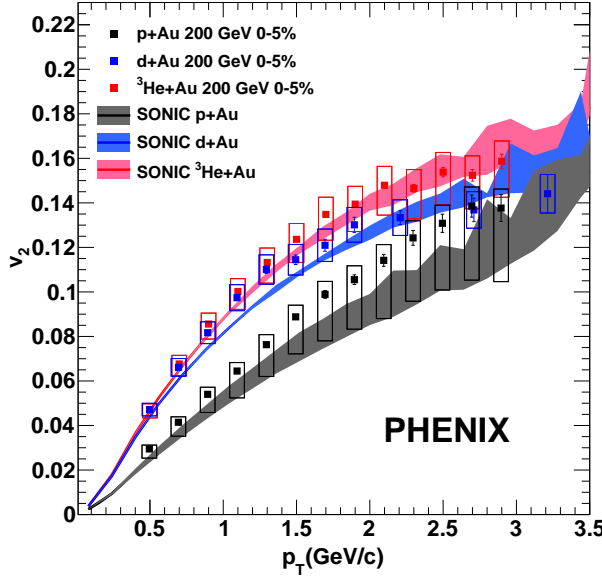


Figure 6.1:  $v_2$  of charged hadrons within  $|\eta| < 0.35$  in 0–5% centrality  $p$ +Au,  $d$ +Au, and  $^3\text{He}+\text{Au}$  at  $\sqrt{s_{NN}} = 200$  GeV, compared with hydrodynamic calculations using the SONIC model, matched to the same multiplicity as the data [33].

of non-flow, then  $v_2 \propto \varepsilon_2$ . Thus, the MC-Glauber  $\varepsilon_2$  for  $p$ +Au,  $d$ +Au, and  $^3\text{He}+\text{Au}$  being 0.23, 0.54, and 0.50, respectively, implies the ordering of  $v_2$  of the three systems should be  $v_2^{d+\text{Au}} \approx v_2^{^3\text{He}+\text{Au}} > v_2^{p+\text{Au}}$ , which is what is observed in Figure 6.1.

Future work is being done in analyzing small collision systems recently run (in 2016) at RHIC:  $d$ +Au at  $\sqrt{s_{NN}} = 200, 62.4, 39$ , and  $19.6$  GeV. By measuring the elliptic flow in this  $d$ +Au beam energy scan, information on the effect of varying the initial temperature and the lifetime of the medium can be obtained. It is noteworthy that even at low  $\sqrt{s_{NN}}$  for  $d$ +Au collisions, hydrodynamic simulations predict that the space-time volume of QGP is not negligible, as shown in Figure 6.2 [34]. In fact, the calculated space-time volume of the medium at  $\sqrt{s_{NN}} = 19.6$  GeV is roughly half of the calculated space-time volume for  $\sqrt{s_{NN}} = 200$  GeV, indicating that there is a reasonable expectation to see some evidence of a QGP medium forming in  $d$ +Au collisions event at  $\sqrt{s_{NN}} = 19.6$  GeV.

Predications have been made of the  $v_2$  for the various energies of the  $d$ +Au beam energy

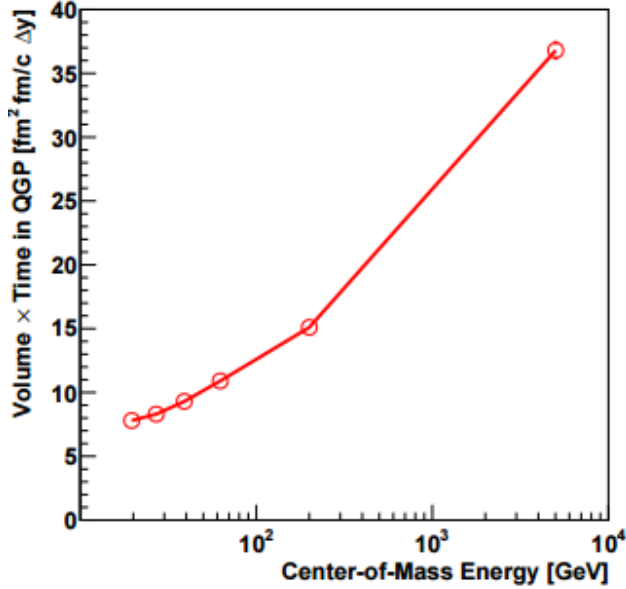


Figure 6.2: The total space-time volume as a function of  $\sqrt{s_{NN}}$  in heavy ion collisions calculated by a hydrodynamic model [34].

scan by using the SONIC, superSONIC, and AMPT models; these models are described in Chapter 2. Figure 6.3 shows predictions for  $v_2$  in the four different energy collisions. The SONIC and superSONIC models (the hydrodynamic models) both predict that there will be a sizable  $v_2$  at all  $\sqrt{s_{NN}}$  systems and that the  $v_2$  will have a positive  $\sqrt{s_{NN}}$  dependence across all  $p_T$ . AMPT, a non-hydrodynamic model, predicts a similarly large  $v_2$  across the different energies with only a modest  $\sqrt{s_{NN}}$  dependence for  $p_T \approx 1.0$  GeV/c and less. The differences between the SONIC and superSONIC  $v_2$  and the AMPT  $v_2$  at  $p_T > 1.0$  GeV/c is further explored in Ref [34]. The future measurement of elliptic flow in the  $d$ +Au beam energy scan datasets, along with the measurement of the completion of the set of three measurements made in this thesis, furthers our understanding of the phenomena of QGP in small collision systems.

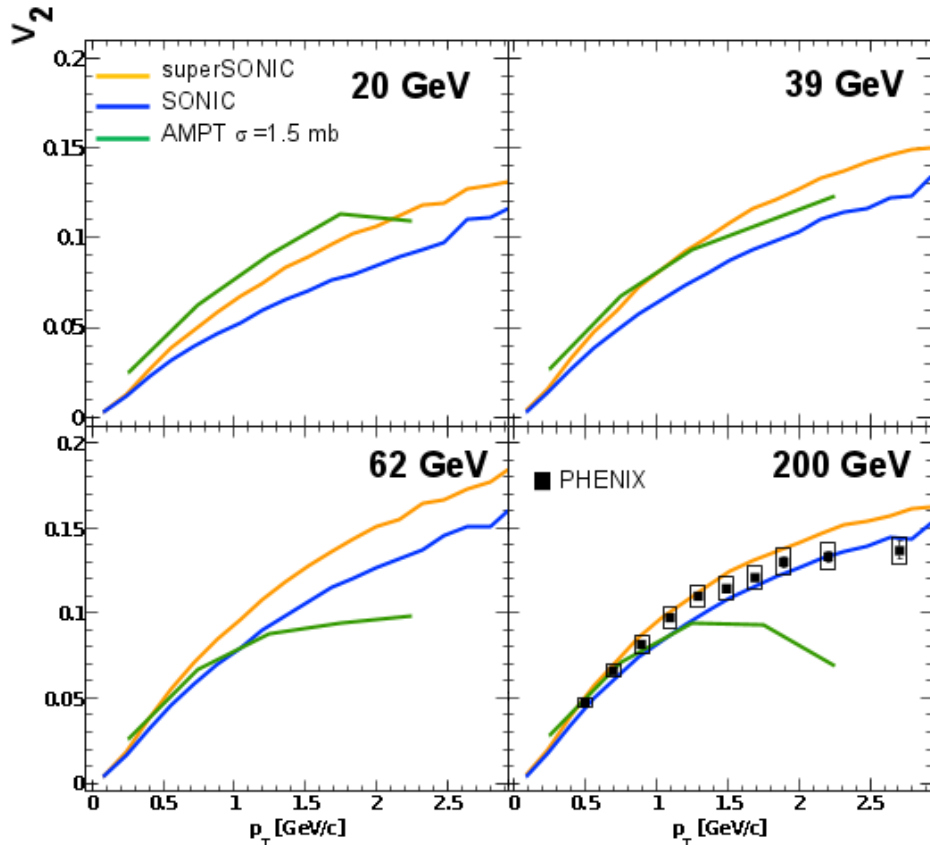


Figure 6.3: Calculations of  $v_2(p_T)$   $d+Au$  events at various  $\sqrt{s_{NN}}$  (given on the upper right of each panel) for AMPT, SONIC, and Supersonic models. Note that there are data points in the lower right panel due to the fact that the  $v_2$  in  $d+Au$  at  $\sqrt{s_{NN}} = 200$  GeV has been measured previously by PHENIX from data taken in 2008 [34].

## Bibliography

- [1] J. L. Nagle, A. Adare, S. Beckman, T. Koblesky, J. Orjuela Koop, D. McGlinchey, P. Romschke, J. Carlson, J. E. Lynn, and M. McCumber. Exploiting intrinsic triangular geometry in relativistic  ${}^3\text{He} + \text{Au}$  collisions to disentangle medium properties. *Phys. Rev. Lett.*, 113: 112301, Sep 2014. doi: 10.1103/PhysRevLett.113.112301. URL <http://link.aps.org/doi/10.1103/PhysRevLett.113.112301>.
- [2] C. et al. Aidala. Measurement of long-range angular correlations and azimuthal anisotropies in high-multiplicity  $p + \text{Au}$  collisions at  $\sqrt{s_{NN}} = 200$  gev. *Phys. Rev. C*, 95:034910, Mar 2017. doi: 10.1103/PhysRevC.95.034910. URL <https://link.aps.org/doi/10.1103/PhysRevC.95.034910>.
- [3] Eric Michael Belmont. Measurements of identified hadrons in Au+Au and d+Au collisions at  $\sqrt{s_{NN}} = 200$  GeV. PhD thesis, Vanderbilt, 2012.
- [4] A. Adare and et al. Transverse energy production and charged-particle multiplicity at midrapidity in various systems from  $\sqrt{s_{NN}} = 7.7$  to 200 gev. *Phys. Rev. C*, 93:024901, Feb 2016. doi: 10.1103/PhysRevC.93.024901. URL <http://link.aps.org/doi/10.1103/PhysRevC.93.024901>.
- [5] J. et al Beringer. Review of particle physics. *Phys. Rev. D*, 86:010001, Jul 2012. doi: 10.1103/PhysRevD.86.010001. URL <http://link.aps.org/doi/10.1103/PhysRevD.86.010001>.
- [6] F. D. et al Aaron. Inclusive deep inelastic scattering at high  $q^2$  with longitudinally polarised lepton beams at hera. *Journal of High Energy Physics*, 2012(9):61, 2012. ISSN 1029-8479. doi: 10.1007/JHEP09(2012)061. URL [http://dx.doi.org/10.1007/JHEP09\(2012\)061](http://dx.doi.org/10.1007/JHEP09(2012)061).
- [7] Siegfried Bethke. The 2009 world average of  $\alpha$ . *The European Physical Journal C*, 64(4): 689–703, 2009. ISSN 1434-6052. doi: 10.1140/epjc/s10052-009-1173-1. URL <http://dx.doi.org/10.1140/epjc/s10052-009-1173-1>.
- [8] Rajeev S. Bhalerao. Relativistic heavy-ion collisions. In Proceedings, 1st Asia-Europe-Pacific School of High-Energy Physics (AEPSHEP): Fukuoka, Japan, October 14-27, 2012, pages 219–239, 2014. doi: 10.5170/CERN-2014-001.219. URL <https://inspirehep.net/record/1290394/files/arXiv:1404.3294.pdf>.
- [9] Johann Rafelski and Jeremiah Birrell. Traveling through the universe: Back in time to the quark-gluon plasma era. *Journal of Physics: Conference Series*, 509(1):012014, 2014. URL <http://stacks.iop.org/1742-6596/509/i=1/a=012014>.

- [10] M. Cheng, S. Ejiri, P. Hegde, F. Karsch, O. Kaczmarek, E. Laermann, R. D. Mawhinney, C. Miao, S. Mukherjee, P. Petreczky, C. Schmidt, and W. Soeldner. Equation of state for physical quark masses. *Phys. Rev. D*, 81:054504, Mar 2010. doi: 10.1103/PhysRevD.81.054504. URL <http://link.aps.org/doi/10.1103/PhysRevD.81.054504>.
- [11] Ulrich W. Heinz. Towards the Little Bang Standard Model. *J. Phys. Conf. Ser.*, 455:012044, 2013. doi: 10.1088/1742-6596/455/1/012044.
- [12] S. S. et al Adler. Absence of suppression in particle production at large transverse momentum in  $\sqrt{s_{NN}} = 200$  GeV  $d + Au$  collisions. *Phys. Rev. Lett.*, 91:072303, Aug 2003. doi: 10.1103/PhysRevLett.91.072303. URL <http://link.aps.org/doi/10.1103/PhysRevLett.91.072303>.
- [13] Guang-You Qin. Anisotropic Flow and Jet Quenching in Relativistic Nuclear Collisions. *Int. J. Mod. Phys.*, E24(02):1530001, 2015. doi: 10.1142/S0218301315300015.
- [14] Charles Gale, Sangyong Jeon, Björn Schenke, Prithwish Tripathy, and Raju Venugopalan. Event-by-event anisotropic flow in heavy-ion collisions from combined yang-mills and viscous fluid dynamics. *Phys. Rev. Lett.*, 110:012302, Jan 2013. doi: 10.1103/PhysRevLett.110.012302. URL <http://link.aps.org/doi/10.1103/PhysRevLett.110.012302>.
- [15] Eric Michael Richardson. Elliptic flow at forward rapidity in  $\sqrt{s_{NN}} = 200$  GeV  $Au+Au$  collisions. PhD thesis, Maryland U., 2012. URL [https://inspirehep.net/record/1221131/files/Richardson\\_Eric-Eric\\_Richardson\\_Dissertation.pdf](https://inspirehep.net/record/1221131/files/Richardson_Eric-Eric_Richardson_Dissertation.pdf).
- [16] V. Khachatryan and et al. Observation of long-range, near-side angular correlations in proton-proton collisions at the lhc. *Journal of High Energy Physics*, 2010(9):91, 2010. ISSN 1029-8479. doi: 10.1007/JHEP09(2010)091. URL [http://dx.doi.org/10.1007/JHEP09\(2010\)091](http://dx.doi.org/10.1007/JHEP09(2010)091).
- [17] K. Aamodt and et al. Harmonic decomposition of two particle angular correlations in pbpb collisions at. *Physics Letters B*, 708(35):249 – 264, 2012. ISSN 0370-2693. doi: <http://dx.doi.org/10.1016/j.physletb.2012.01.060>. URL <http://www.sciencedirect.com/science/article/pii/S0370269312001013>.
- [18] Stephen J. Sanders Michael L. Miller, Klaus Reygers and Peter Steinberg. Glauber modeling in high-energy nuclear collisions. *Annual Review of Nuclear and Particle Science*, 57:205–243, 2007. URL <http://www.annualreviews.org/doi/10.1146/annurev.nucl.57.090506.123020>.
- [19] Björn Schenke, Prithwish Tripathy, and Raju Venugopalan. Fluctuating glasma initial conditions and flow in heavy ion collisions. *Phys. Rev. Lett.*, 108:252301, Jun 2012. doi: 10.1103/PhysRevLett.108.252301. URL <http://link.aps.org/doi/10.1103/PhysRevLett.108.252301>.
- [20] B. Abelev et al. Long-range angular correlations of  $k$  and  $p$  in pp collisions at  $\sqrt{s_{NN}} = 5.02$  tev. *Physics Letters B*, 726(13):164 – 177, 2013. ISSN 0370-2693. doi: <http://dx.doi.org/10.1016/j.physletb.2013.08.024>. URL <http://www.sciencedirect.com/science/article/pii/S0370269313006503>.
- [21] J. et al Adam. Higher harmonic flow coefficients of identified hadrons in pb-pb collisions at  $\sqrt{s} = 2.76$  tev. *Journal of High Energy Physics*, 2016(9):164, 2016. ISSN 1029-8479. doi: 10.1007/JHEP09(2016)164. URL [http://dx.doi.org/10.1007/JHEP09\(2016\)164](http://dx.doi.org/10.1007/JHEP09(2016)164).

- [22] V. Khachatryan and et al. Evidence for collectivity in pp collisions at the {LHC}. *Physics Letters B*, 765:193 – 220, 2017. ISSN 0370-2693. doi: <http://dx.doi.org/10.1016/j.physletb.2016.12.009>. URL <http://www.sciencedirect.com/science/article/pii/S037026931630747X>.
- [23] A. et al Adare. Measurements of elliptic and triangular flow in high-multiplicity  ${}^3\text{He} + \text{Au}$  collisions at  $\sqrt{s_{NN}} = 200$  GeV. *Phys. Rev. Lett.*, 115:142301, Sep 2015. doi: 10.1103/PhysRevLett.115.142301. URL <http://link.aps.org/doi/10.1103/PhysRevLett.115.142301>.
- [24] M. J. Tannenbaum. Highlights from BNL-RHIC. *Subnucl. Ser.*, 50:347–367, 2014. doi: 10.1142/9789814603904\_0022.
- [25] C. Aidala et al. The {PHENIX} forward silicon vertex detector. *Nuclear Instruments and Methods in Physics Research Section A: Accelerators, Spectrometers, Detectors and Associated Equipment*, 755:44 – 61, 2014. ISSN 0168-9002. doi: <http://dx.doi.org/10.1016/j.nima.2014.04.017>. URL <http://www.sciencedirect.com/science/article/pii/S0168900214004124>.
- [26] S.H. Aronson and et al. {PHENIX} magnet system. *Nuclear Instruments and Methods in Physics Research Section A: Accelerators, Spectrometers, Detectors and Associated Equipment*, 499(23):480 – 488, 2003. ISSN 0168-9002. doi: [http://dx.doi.org/10.1016/S0168-9002\(02\)01951-4](http://dx.doi.org/10.1016/S0168-9002(02)01951-4). URL <http://www.sciencedirect.com/science/article/pii/S0168900202019514>. The Relativistic Heavy Ion Collider Project: {RHIC} and its Detectors.
- [27] K. Adcox et al. {PHENIX} detector overview. *Nuclear Instruments and Methods in Physics Research Section A: Accelerators, Spectrometers, Detectors and Associated Equipment*, 499(2?3):469 – 479, 2003. ISSN 0168-9002. doi: [http://dx.doi.org/10.1016/S0168-9002\(02\)01950-2](http://dx.doi.org/10.1016/S0168-9002(02)01950-2). URL <http://www.sciencedirect.com/science/article/pii/S0168900202019502>. The Relativistic Heavy Ion Collider Project: {RHIC} and its Detectors.
- [28] M. Aizawa et al. {PHENIX} central arm particle {ID} detectors. *Nuclear Instruments and Methods in Physics Research Section A: Accelerators, Spectrometers, Detectors and Associated Equipment*, 499(23):508 – 520, 2003. ISSN 0168-9002. doi: [http://dx.doi.org/10.1016/S0168-9002\(02\)01953-8](http://dx.doi.org/10.1016/S0168-9002(02)01953-8). URL <http://www.sciencedirect.com/science/article/pii/S0168900202019538>. The Relativistic Heavy Ion Collider Project: {RHIC} and its Detectors.
- [29] A. Adare and et al. Centrality categorization for  $R_{p(d)+A}$  in high-energy collisions. *Phys. Rev. C*, 90:034902, Sep 2014. doi: 10.1103/PhysRevC.90.034902. URL <http://link.aps.org/doi/10.1103/PhysRevC.90.034902>.
- [30] Event reconstruction in the {PHENIX} central arm spectrometers. *Nucl.Instrum.Meth*, A482: 491–512, 2002.
- [31] Bjrn Schenke and Raju Venugopalan. Collective effects in lightheavy ion collisions. *Nuclear Physics A*, 931:1039 – 1044, 2014. ISSN 0375-9474. doi: <http://dx.doi.org/10.1016/j.nuclphysa.2014.08.092>. URL <http://www.sciencedirect.com/science/article/pii/S0375947414003522>. {QUARK} {MATTER} 2014XXIV {INTERNATIONAL} {CONFERENCE} {ON} {ULTRARELATIVISTIC} NUCLEUS-NUCLEUS {COLLISIONS}.

- [32] Kevin Welsh, Jordan Singer, and Ulrich Heinz. Initial-state fluctuations in collisions between light and heavy ions. *Phys. Rev. C*, 94:024919, Aug 2016. doi: 10.1103/PhysRevC.94.024919. URL <http://link.aps.org/doi/10.1103/PhysRevC.94.024919>.
- [33] M. Habich, J. L. Nagle, and P. Romatschke. Particle spectra and hbt radii for simulated central nuclear collisions of c+c, al+al, cu+cu, au+au, and pb+pb from  $\text{sqrt}(s)=62.4-2760$  gev. *The European Physical Journal C*, 75(1):15, 2015. ISSN 1434-6052. doi: 10.1140/epjc/s10052-014-3206-7. URL <http://dx.doi.org/10.1140/epjc/s10052-014-3206-7>.
- [34] J. D. Orjuela Koop, R. Belmont, P. Yin, and J. L. Nagle. Exploring the beam-energy dependence of flow-like signatures in small-system  $d + \text{Au}$  collisions. *Phys. Rev. C*, 93:044910, Apr 2016. doi: 10.1103/PhysRevC.93.044910. URL <http://link.aps.org/doi/10.1103/PhysRevC.93.044910>.
- [35] S.M. Bilenky and J. Hoek. Glashow-weinberg-salam theory of electroweak interactions and the neutral currents. *Physics Reports*, 90(2):73 – 157, 1982. ISSN 0370-1573. doi: [http://dx.doi.org/10.1016/0370-1573\(82\)90016-3](http://dx.doi.org/10.1016/0370-1573(82)90016-3). URL <http://www.sciencedirect.com/science/article/pii/0370157382900163>.
- [36] Roel Aaij et al. Observation of  $J/\psi p$  Resonances Consistent with Pentaquark States in  $\Lambda_b^0 \rightarrow J/\psi K^- p$  Decays. *Phys. Rev. Lett.*, 115:072001, 2015. doi: 10.1103/PhysRevLett.115.072001.
- [37] Helmut Satz. The quark-gluon plasma a short introduction. *Nuclear Physics A*, 862:4 – 12, 2011. ISSN 0375-9474. doi: <http://dx.doi.org/10.1016/j.nuclphysa.2011.05.014>. URL <http://www.sciencedirect.com/science/article/pii/S0375947411003435>.
- [38] Johann Rafelski. Connecting qgp-heavy ion physics to the early universe. *Nuclear Physics B - Proceedings Supplements*, 243:155 – 162, 2013. ISSN 0920-5632. doi: <http://dx.doi.org/10.1016/j.nuclphysbps.2013.09.017>. URL <http://www.sciencedirect.com/science/article/pii/S0920563213005410>.
- [39] Enrico Fermi. High energy nuclear events. *Progress of Theoretical Physics*, 5(4):570–583, 1950. doi: 10.1143/ptp/5.4.570. URL <http://ptp.oxfordjournals.org/content/5/4/570.abstract>.
- [40] Yasuyuki Akiba et al. The Hot QCD White Paper: Exploring the Phases of QCD at RHIC and the LHC. 2015.
- [41] S. Voloshin and Y. Zhang. Flow study in relativistic nuclear collisions by fourier expansion of azimuthal particle distributions. *Zeitschrift für Physik C Particles and Fields*, 70(4):665–671, 1996. ISSN 1431-5858. doi: 10.1007/s002880050141. URL <http://dx.doi.org/10.1007/s002880050141>.
- [42] Fernando G. Gardim, Frédérique Grassi, Matthew Luzum, and Jean-Yves Ollitrault. Breaking of factorization of two-particle correlations in hydrodynamics. *Phys. Rev. C*, 87:031901, Mar 2013. doi: 10.1103/PhysRevC.87.031901. URL <http://link.aps.org/doi/10.1103/PhysRevC.87.031901>.
- [43] A. M. Poskanzer and S. A. Voloshin. Methods for analyzing anisotropic flow in relativistic nuclear collisions. *Phys. Rev. C*, 58:1671–1678, Sep 1998. doi: 10.1103/PhysRevC.58.1671. URL <http://link.aps.org/doi/10.1103/PhysRevC.58.1671>.

- [44] B. Alver and G. Roland. Collision-geometry fluctuations and triangular flow in heavy-ion collisions. *Phys. Rev. C*, 81:054905, May 2010. doi: 10.1103/PhysRevC.81.054905. URL <http://link.aps.org/doi/10.1103/PhysRevC.81.054905>.
- [45] B. Alver, M. Baker, C. Loizides, and P. Steinberg. The PHOBOS Glauber Monte Carlo. 2008.
- [46] H. De Vries, C.W. De Jager, and C. De Vries. Nuclear charge-density-distribution parameters from elastic electron scattering. *Atomic Data and Nuclear Data Tables*, 36(3):495 – 536, 1987. ISSN 0092-640X. doi: [http://dx.doi.org/10.1016/0092-640X\(87\)90013-1](http://dx.doi.org/10.1016/0092-640X(87)90013-1). URL <http://www.sciencedirect.com/science/article/pii/0092640X87900131>.
- [47] Edmond Iancu and Raju Venugopalan. The Color glass condensate and high-energy scattering in QCD. In *In \*Hwa, R.C. (ed.) et al.: Quark gluon plasma\* 249-3363*, 2003. doi: 10.1142/978981279533\_0005.
- [48] Huichao Song. Hydrodynamic modelling for relativistic heavy-ion collisions at rhic and lhc. *Pramana*, 84(5):703–715, 2015. ISSN 0973-7111. doi: 10.1007/s12043-015-0971-2. URL <http://dx.doi.org/10.1007/s12043-015-0971-2>.
- [49] Fred Cooper and Graham Frye. Single-particle distribution in the hydrodynamic and statistical thermodynamic models of multiparticle production. *Phys. Rev. D*, 10:186–189, Jul 1974. doi: 10.1103/PhysRevD.10.186. URL <http://link.aps.org/doi/10.1103/PhysRevD.10.186>.
- [50] Peter F. Kolb and Ulrich W. Heinz. Hydrodynamic description of ultrarelativistic heavy ion collisions. 2003.
- [51] J. Scott Moreland, Jonah E. Bernhard, and Steffen A. Bass. Alternative ansatz to wounded nucleon and binary collision scaling in high-energy nuclear collisions. *Phys. Rev. C*, 92:011901, Jul 2015. doi: 10.1103/PhysRevC.92.011901. URL <http://link.aps.org/doi/10.1103/PhysRevC.92.011901>.
- [52] P. Romatschke. Light-heavy-ion collisions: a window into pre-equilibrium qcd dynamics? *The European Physical Journal C*, 75(7):305, 2015. ISSN 1434-6052. doi: 10.1140/epjc/s10052-015-3509-3. URL <http://dx.doi.org/10.1140/epjc/s10052-015-3509-3>.
- [53] Zi-Wei Lin, Che Ming Ko, Bao-An Li, Bin Zhang, and Subrata Pal. Multiphase transport model for relativistic heavy ion collisions. *Phys. Rev. C*, 72:064901, Dec 2005. doi: 10.1103/PhysRevC.72.064901. URL <http://link.aps.org/doi/10.1103/PhysRevC.72.064901>.
- [54] A. D. Frawley. Cold Nuclear Matter Effects and Heavy Quark Production in PHENIX. *Nucl. Phys.*, A910-911:123–130, 2013. doi: 10.1016/j.nuclphysa.2012.12.032.
- [55] Tetsufumi Hirano, Ulrich Heinz, Dmitri Kharzeev, Roy Lacey, and Yasushi Nara. Mass ordering of differential elliptic flow and its violation for  $\phi$  mesons. *Phys. Rev. C*, 77:044909, Apr 2008. doi: 10.1103/PhysRevC.77.044909. URL <http://link.aps.org/doi/10.1103/PhysRevC.77.044909>.
- [56] Jean-Yves Ollitrault, Arthur M. Poskanzer, and Sergei A. Voloshin. Effect of flow fluctuations and nonflow on elliptic flow methods. *Phys. Rev. C*, 80:014904, Jul 2009. doi: 10.1103/PhysRevC.80.014904. URL <http://link.aps.org/doi/10.1103/PhysRevC.80.014904>.

- [57] Kevin Dusling and Raju Venugopalan. Azimuthal collimation of long range rapidity correlations by strong color fields in high multiplicity hadron-hadron collisions. *Phys. Rev. Lett.*, 108: 262001, Jun 2012. doi: 10.1103/PhysRevLett.108.262001. URL <http://link.aps.org/doi/10.1103/PhysRevLett.108.262001>.
- [58] A. Ortiz Velasquez, P. Christiansen, E. Cuautle Flores, I. A. Maldonado Cervantes, and G. Paić. Color reconnection and flowlike patterns in  $pp$  collisions. *Phys. Rev. Lett.*, 111: 042001, Jul 2013. doi: 10.1103/PhysRevLett.111.042001. URL <http://link.aps.org/doi/10.1103/PhysRevLett.111.042001>.
- [59] Adam Bzdak and Guo-Liang Ma. Elliptic and triangular flow in  $p$ -pb and peripheral pb-pb collisions from parton scatterings. *Phys. Rev. Lett.*, 113:252301, Dec 2014. doi: 10.1103/PhysRevLett.113.252301. URL <http://link.aps.org/doi/10.1103/PhysRevLett.113.252301>.
- [60] T. Roser. Rhic performance. *Nuclear Physics A*, 698(1):23 – 28, 2002. ISSN 0375-9474. doi: [http://dx.doi.org/10.1016/S0375-9474\(01\)01345-8](http://dx.doi.org/10.1016/S0375-9474(01)01345-8). URL <http://www.sciencedirect.com/science/article/pii/S0375947401013458>.
- [61] Rhic operations with asymmetric collisions in 2015. 2015. URL <http://www.agsrhichome.bnl.gov/RHIC/Runs/RhicRun15pA2.pdf>.
- [62] Piotr Bozek. Elliptic flow in proton–proton collisions at  $\sqrt{s}=7\text{tev}$ . *The European Physical Journal C*, 71(1):1530, 2011. ISSN 1434-6052. doi: 10.1140/epjc/s10052-010-1530-0. URL <http://dx.doi.org/10.1140/epjc/s10052-010-1530-0>.
- [63] S. Eremin and S. Voloshin. Nucleon participants or quark participants? *Phys. Rev. C*, 67: 064905, Jun 2003. doi: 10.1103/PhysRevC.67.064905. URL <http://link.aps.org/doi/10.1103/PhysRevC.67.064905>.
- [64] Sren Schlichting and Bjrn Schenke. The shape of the proton at high energies. *Physics Letters B*, 739:313 – 319, 2014. ISSN 0370-2693. doi: <http://dx.doi.org/10.1016/j.physletb.2014.10.068>. URL <http://www.sciencedirect.com/science/article/pii/S0370269314008016>.
- [65] M. Habich, J. L. Nagle, and P. Romatschke. Particle spectra and hbt radii for simulated central nuclear collisions of. *The European Physical Journal C*, 75(1):15, 2015. ISSN 1434-6052. doi: 10.1140/epjc/s10052-014-3206-7. URL <http://dx.doi.org/10.1140/epjc/s10052-014-3206-7>.
- [66] Wilke van der Schee, Paul Romatschke, and Scott Pratt. Fully dynamical simulation of central nuclear collisions. *Phys. Rev. Lett.*, 111:222302, Nov 2013. doi: 10.1103/PhysRevLett.111.222302. URL <http://link.aps.org/doi/10.1103/PhysRevLett.111.222302>.
- [67] J. D. Orjuela Koop, A. Adare, D. McGlinchey, and J. L. Nagle. Azimuthal anisotropy relative to the participant plane from a multiphase transport model in central  $p + \text{Au}$ ,  $d + \text{Au}$ , and  ${}^3\text{He} + \text{Au}$  collisions at  $\sqrt{s_{NN}} = 200$  gev. *Phys. Rev. C*, 92:054903, Nov 2015. doi: 10.1103/PhysRevC.92.054903. URL <http://link.aps.org/doi/10.1103/PhysRevC.92.054903>.
- [68] Guo-Liang Ma and Zi-Wei Lin. Predictions for  $\sqrt{s_{NN}} = 5.02$  tev  $\text{pb} + \text{pb}$  collisions from a multiphase transport model. *Phys. Rev. C*, 93:054911, May 2016. doi: 10.1103/PhysRevC.93.054911. URL <http://link.aps.org/doi/10.1103/PhysRevC.93.054911>.

- [69] Matthew Luzum and Paul Romatschke. Conformal relativistic viscous hydrodynamics: Applications to rhic results at  $\sqrt{s_{NN}} = 200$  gev. *Phys. Rev. C*, 78:034915, Sep 2008. doi: 10.1103/PhysRevC.78.034915. URL <http://link.aps.org/doi/10.1103/PhysRevC.78.034915>.
- [70] XIAO-MING XU. ORIGIN OF TEMPERATURE OF QUARK-GLUON PLASMA IN HEAVY ION COLLISIONS, pages 203–208. WORLD SCIENTIFIC, 2015. doi: 10.1142/9789814689304\_0031. URL [http://www.worldscientific.com/doi/abs/10.1142/9789814689304\\_0031](http://www.worldscientific.com/doi/abs/10.1142/9789814689304_0031).
- [71] A Fedotov. Progress of high-energy electron cooling for rhic. 2007.

## Appendix A

### $v_2(p_T)$ with Different $\Psi_2$ Weighting

In this appendix, we show the  $v_2(p_T)$  measurement with the FVTXS and BBCS event plane with various corrections which are described in Chapter 4. We show  $v_2(p_T)$  for each layer of the FVTX and each ring of the BBC separately.

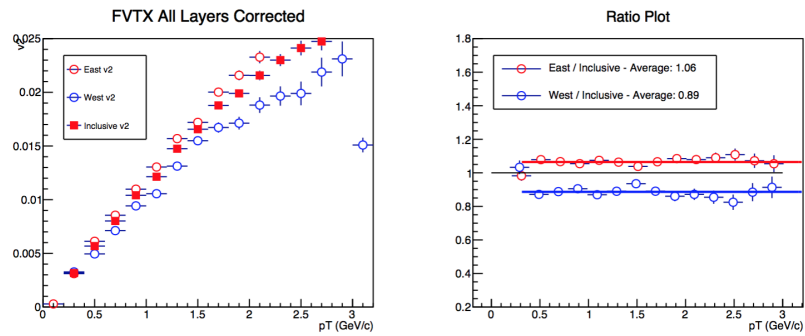


Figure A.1: FVTXS event plane measurement with default correction and FVTX layers 1, 2, and 4 of  $v_2(p_T)$  with the for the  $p+\text{Au}$   $\sqrt{s_{NN}} = 200$  GeV (left) and the ratio of the east and west  $v_2$  measurements to the inclusive  $v_2$  (right).

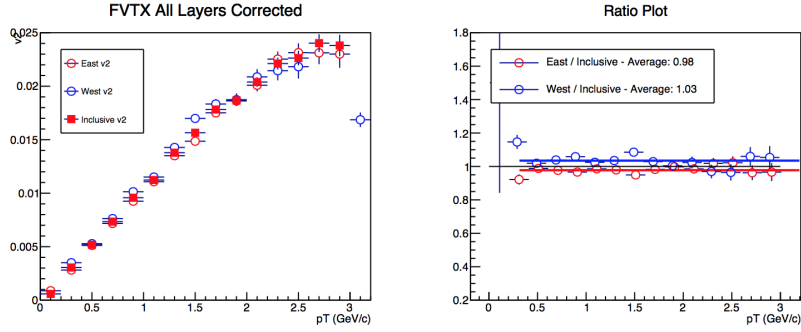


Figure A.2: FVTXS event plane measurement with inverse  $\phi$  weighting and FVTX layers 1, 2, and 4 of  $v_2(p_T)$  with the for the  $p+\text{Au}$   $\sqrt{s_{NN}} = 200$  GeV (left) and the ratio of the east and west  $v_2$  measurements to the inclusive  $v_2$  (right).

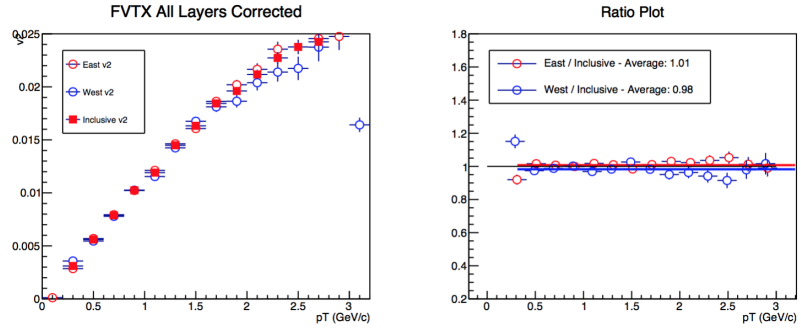


Figure A.3: FVTXS event plane measurement with analytic weighting and a 20% cut and FVTX layers 1, 2, and 4 of  $v_2(p_T)$  with the for the  $p+\text{Au}$   $\sqrt{s_{NN}} = 200$  GeV (left) and the ratio of the east and west  $v_2$  measurements to the inclusive  $v_2$  (right).

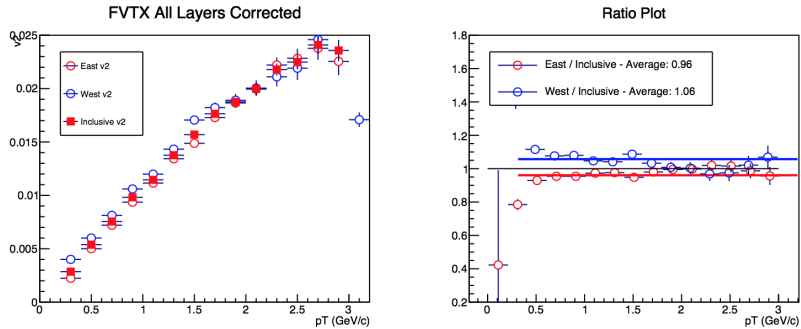


Figure A.4: FVTXS event plane measurement with inverse  $\phi$  weighting and a 20% cut and FVTX layers 1, 2, and 4 of  $v_2(p_T)$  with the for the  $p+\text{Au}$   $\sqrt{s_{NN}} = 200$  GeV (left) and the ratio of the east and west  $v_2$  measurements to the inclusive  $v_2$  (right).

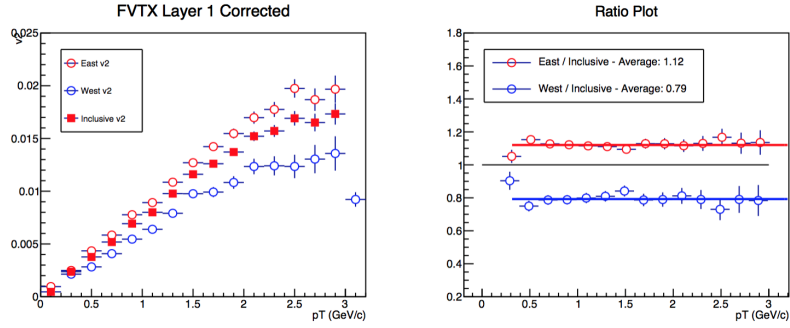


Figure A.5: FVTXS event plane measurement with default correction and FVTX layer 1 of  $v_2(p_T)$  with the for the  $p+\text{Au}$   $\sqrt{s_{NN}} = 200$  GeV (left) and the ratio of the east and west  $v_2$  measurements to the inclusive  $v_2$  (right).

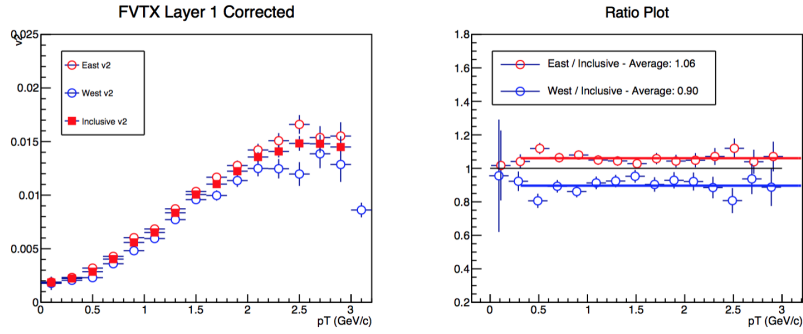


Figure A.6: FVTXS event plane measurement with inverse  $\phi$  weighting and FVTX layer 1 of  $v_2(p_T)$  with the for the  $p+\text{Au}$   $\sqrt{s_{NN}} = 200$  GeV (left) and the ratio of the east and west  $v_2$  measurements to the inclusive  $v_2$  (right).

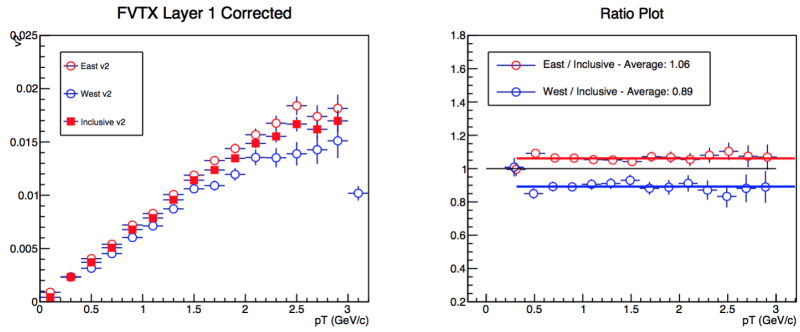


Figure A.7: FVTXS event plane measurement with analytic weighting and a 20% cut and FVTX layer 1 of  $v_2(p_T)$  with the for the  $p+\text{Au}$   $\sqrt{s_{NN}} = 200$  GeV (left) and the ratio of the east and west  $v_2$  measurements to the inclusive  $v_2$  (right).

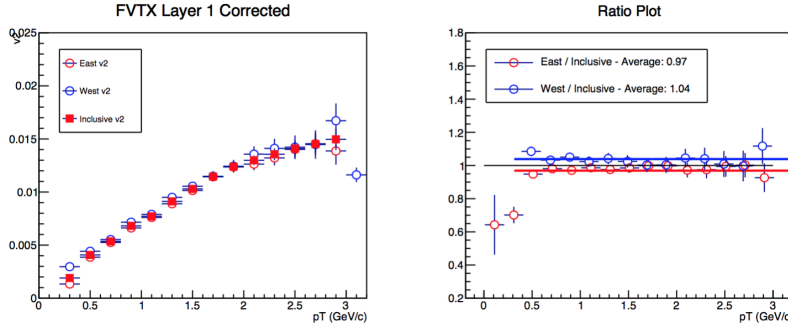


Figure A.8: FVTXS event plane measurement with inverse  $\phi$  weighting and a 20% cut and FVTX layer 1 of  $v_2(p_T)$  with the for the  $p+\text{Au}$   $\sqrt{s_{NN}} = 200$  GeV (left) and the ratio of the east and west  $v_2$  measurements to the inclusive  $v_2$  (right).

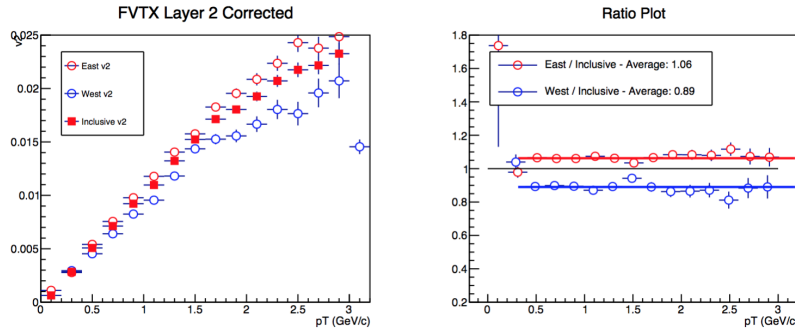


Figure A.9: FVTXS event plane measurement with default correction and FVTX layer 2 of  $v_2(p_T)$  with the for the  $p+\text{Au}$   $\sqrt{s_{NN}} = 200$  GeV (left) and the ratio of the east and west  $v_2$  measurements to the inclusive  $v_2$  (right).

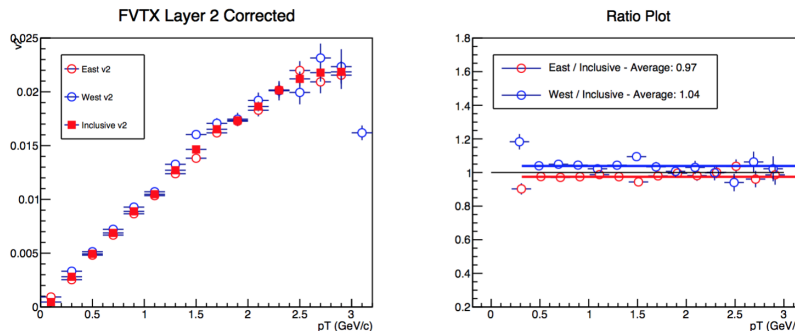


Figure A.10: FVTXS event plane measurement with inverse  $\phi$  weighting and FVTX layer 2 of  $v_2(p_T)$  with the for the  $p+\text{Au}$   $\sqrt{s_{NN}} = 200$  GeV (left) and the ratio of the east and west  $v_2$  measurements to the inclusive  $v_2$  (right).

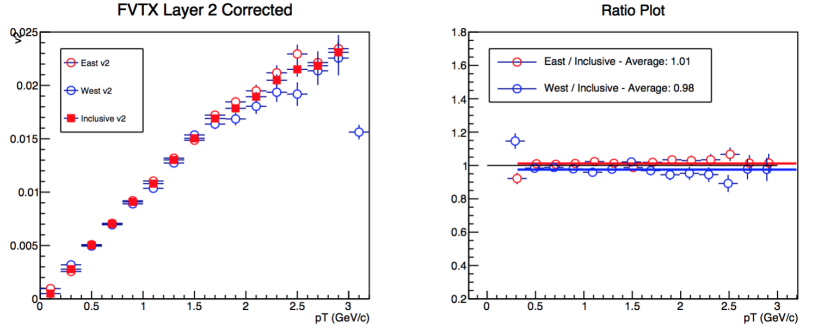


Figure A.11: FVTXS event plane measurement with analytic weighting and a 20% cut and FVTX layer 2 of  $v_2(p_T)$  with the for the  $p+\text{Au}$   $\sqrt{s_{NN}} = 200$  GeV (left) and the ratio of the east and west  $v_2$  measurements to the inclusive  $v_2$  (right).

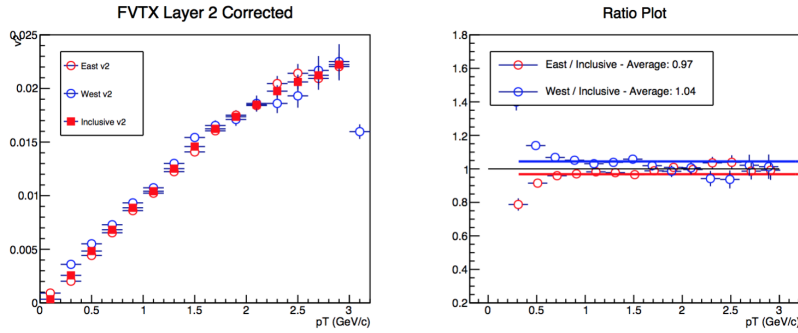


Figure A.12: FVTXS event plane measurement with inverse  $\phi$  weighting and a 20% cut and FVTX layer 2 of  $v_2(p_T)$  with the for the  $p+\text{Au}$   $\sqrt{s_{NN}} = 200$  GeV (left) and the ratio of the east and west  $v_2$  measurements to the inclusive  $v_2$  (right).

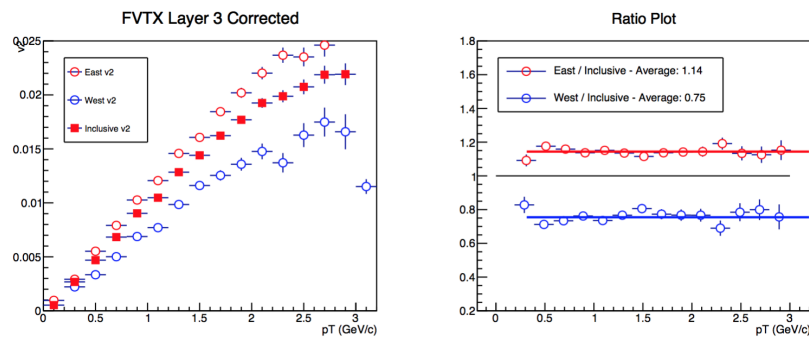


Figure A.13: FVTXS event plane measurement with default correction and FVTX layer 3 of  $v_2(p_T)$  with the for the  $p+\text{Au}$   $\sqrt{s_{NN}} = 200$  GeV (left) and the ratio of the east and west  $v_2$  measurements to the inclusive  $v_2$  (right).

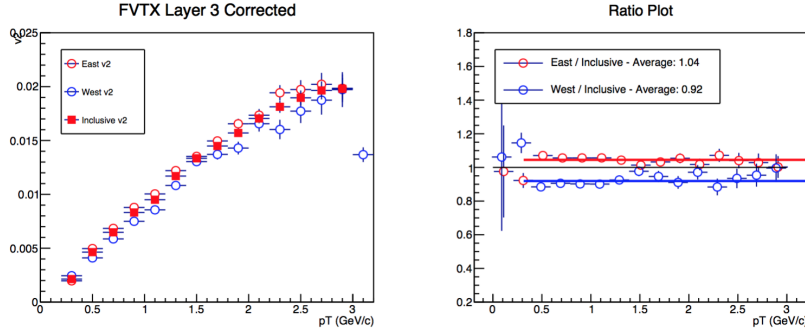


Figure A.14: FVTXS event plane measurement with inverse  $\phi$  weighting and FVTX layer 3 of  $v_2(p_T)$  with the for the  $p+\text{Au}$   $\sqrt{s_{NN}} = 200$  GeV (left) and the ratio of the east and west  $v_2$  measurements to the inclusive  $v_2$  (right).

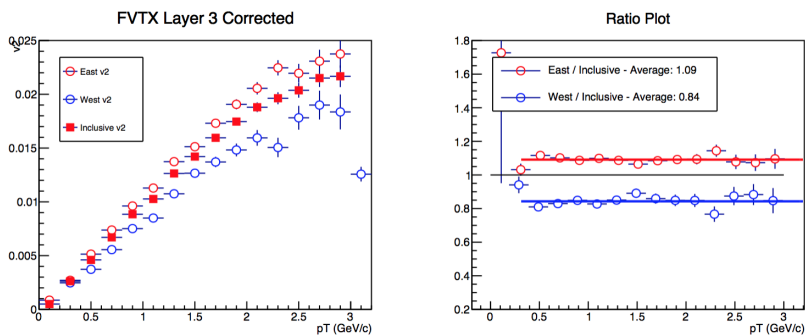


Figure A.15: FVTXS event plane measurement with analytic weighting and a 20% cut and FVTX layer 3 of  $v_2(p_T)$  with the for the  $p+\text{Au}$   $\sqrt{s_{NN}} = 200$  GeV (left) and the ratio of the east and west  $v_2$  measurements to the inclusive  $v_2$  (right).

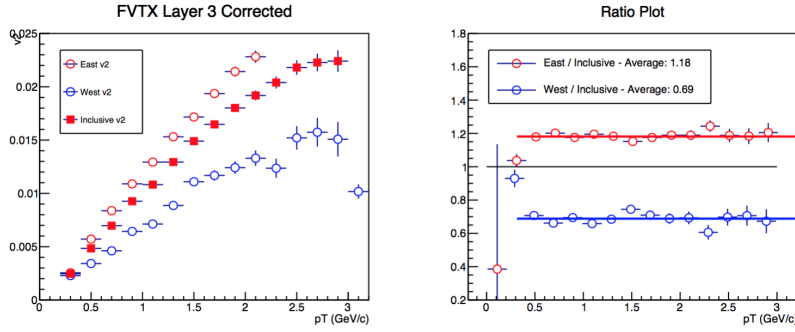


Figure A.16: FVTXS event plane measurement with inverse  $\phi$  weighting and a 20% cut and FVTX layer 3 of  $v_2(p_T)$  with the for the  $p+\text{Au}$   $\sqrt{s_{NN}} = 200$  GeV (left) and the ratio of the east and west  $v_2$  measurements to the inclusive  $v_2$  (right).

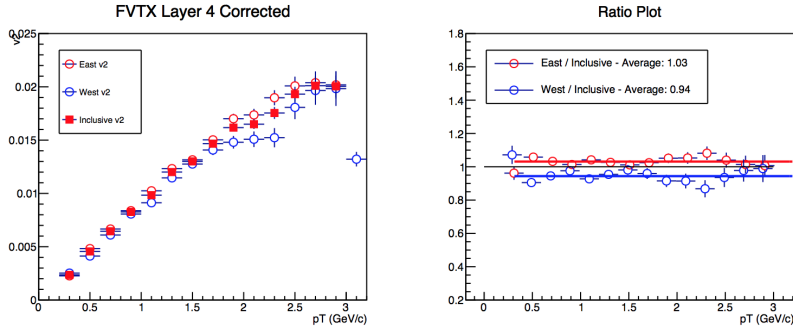


Figure A.17: FVTXS event plane measurement with default correction and FVTX layer 4 of  $v_2(p_T)$  with the for the  $p+\text{Au}$   $\sqrt{s_{NN}} = 200$  GeV (left) and the ratio of the east and west  $v_2$  measurements to the inclusive  $v_2$  (right).

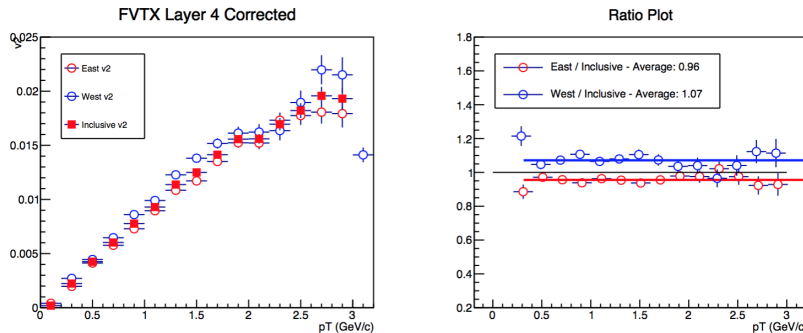


Figure A.18: FVTXS event plane measurement with inverse  $\phi$  weighting and FVTX layer 4 of  $v_2(p_T)$  with the for the  $p+\text{Au}$   $\sqrt{s_{NN}} = 200$  GeV (left) and the ratio of the east and west  $v_2$  measurements to the inclusive  $v_2$  (right).

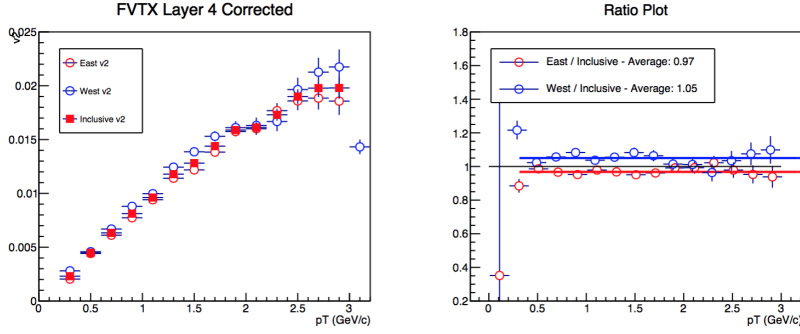


Figure A.19: FVTXS event plane measurement with analytic weighting and a 20% cut and FVTX layer 4 of  $v_2(p_T)$  with the for the  $p+\text{Au}$   $\sqrt{s_{NN}} = 200$  GeV (left) and the ratio of the east and west  $v_2$  measurements to the inclusive  $v_2$  (right).

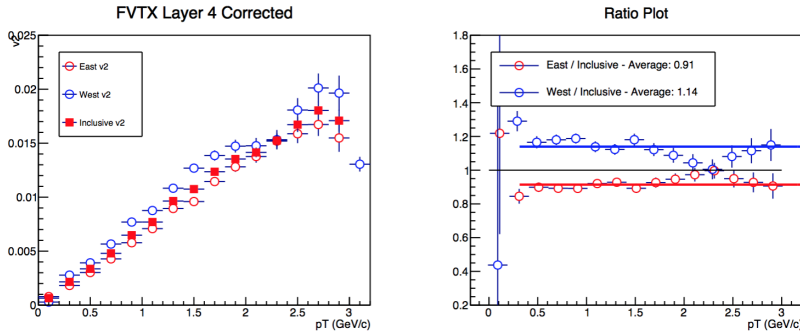


Figure A.20: FVTXS event plane measurement with inverse  $\phi$  weighting and a 20% cut and FVTX layer 4 of  $v_2(p_T)$  with the for the  $p+\text{Au}$   $\sqrt{s_{NN}} = 200$  GeV (left) and the ratio of the east and west  $v_2$  measurements to the inclusive  $v_2$  (right).

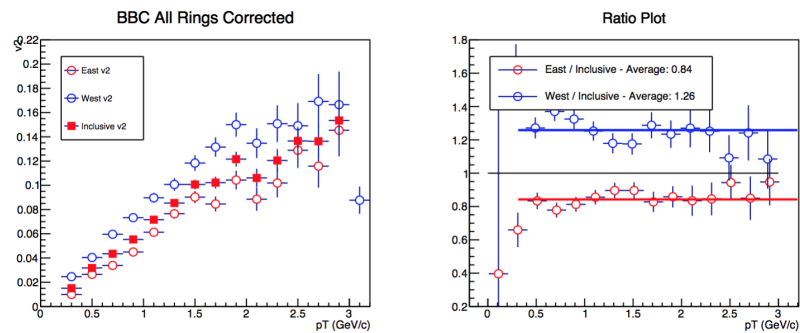


Figure A.21: BBCS event plane measurement with default correction and all BBC rings of  $v_2(p_T)$  with the for the  $p+\text{Au}$   $\sqrt{s_{NN}} = 200$  GeV (left) and the ratio of the east and west  $v_2$  measurements to the inclusive  $v_2$  (right).

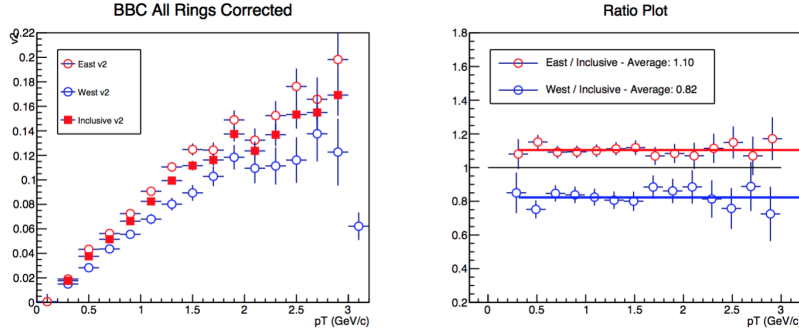


Figure A.22: BBCS event plane measurement with inverse charge correction and all BBC rings of  $v_2(p_T)$  with the for the  $p+\text{Au}$   $\sqrt{s_{NN}} = 200$  GeV (left) and the ratio of the east and west  $v_2$  measurements to the inclusive  $v_2$  (right).

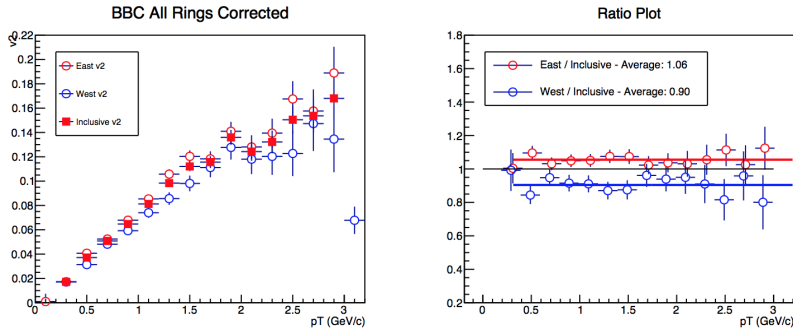


Figure A.23: BBCS event plane measurement with  $p+p/p+\text{Au}$  ratio correction and all BBC rings of  $v_2(p_T)$  with the for the  $p+\text{Au}$   $\sqrt{s_{NN}} = 200$  GeV (left) and the ratio of the east and west  $v_2$  measurements to the inclusive  $v_2$  (right).

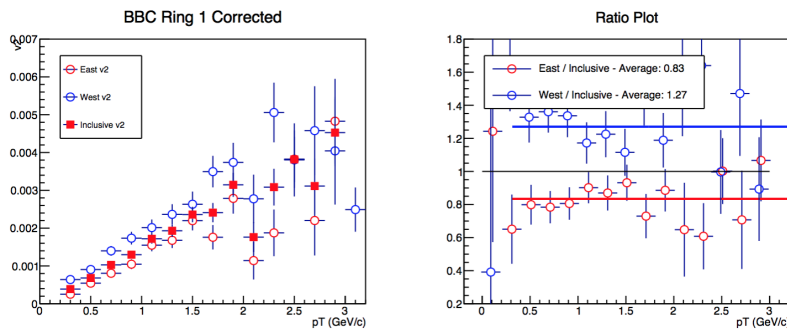


Figure A.24: BBCS event plane measurement with default correction and BBC ring 1 of  $v_2(p_T)$  with the for the  $p+\text{Au}$   $\sqrt{s_{NN}} = 200$  GeV (left) and the ratio of the east and west  $v_2$  measurements to the inclusive  $v_2$  (right).

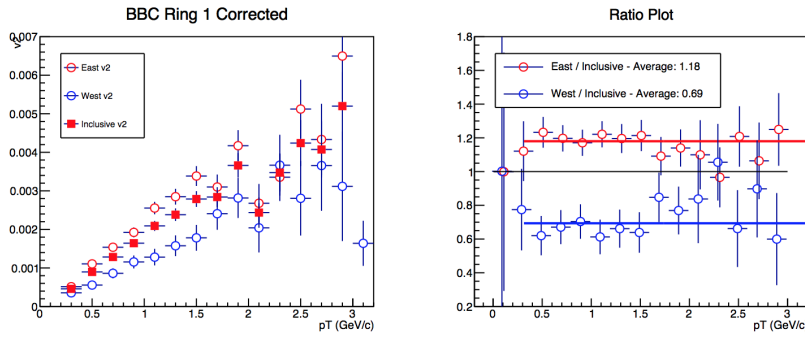


Figure A.25: BBCS event plane measurement with inverse charge correction and BBC ring 1 of  $v_2(p_T)$  with the for the  $p+Au$   $\sqrt{s_{NN}} = 200$  GeV (left) and the ratio of the east and west  $v_2$  measurements to the inclusive  $v_2$  (right).

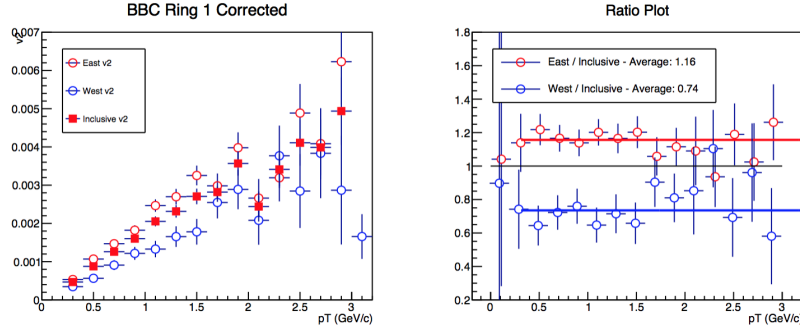


Figure A.26: BBCS event plane measurement with  $p+p/p+\text{Au}$  ratio correction and BBC ring 1 of  $v_2(p_T)$  with the for the  $p+\text{Au}$   $\sqrt{s_{NN}} = 200$  GeV (left) and the ratio of the east and west  $v_2$  measurements to the inclusive  $v_2$  (right).

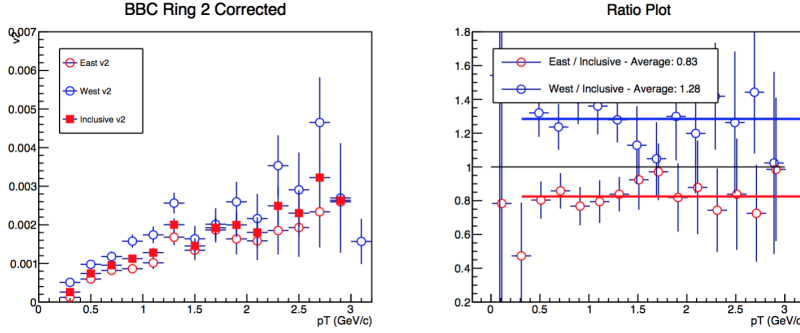


Figure A.27: BBCS event plane measurement with default correction and BBC ring 2 of  $v_2(p_T)$  with the for the  $p+\text{Au}$   $\sqrt{s_{NN}} = 200$  GeV (left) and the ratio of the east and west  $v_2$  measurements to the inclusive  $v_2$  (right).

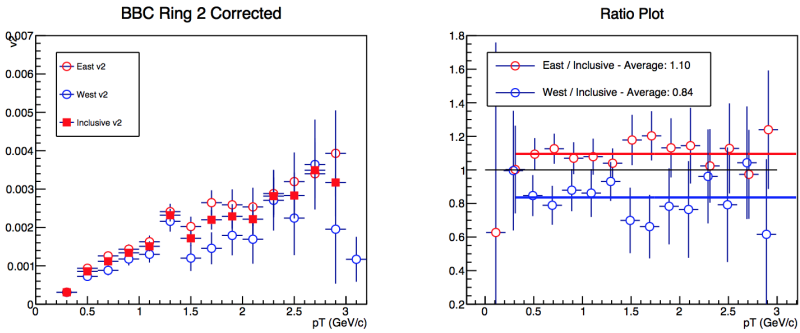


Figure A.28: BBCS event plane measurement with inverse charge correction and BBC ring 2 of  $v_2(p_T)$  with the for the  $p+\text{Au}$   $\sqrt{s_{NN}} = 200$  GeV (left) and the ratio of the east and west  $v_2$  measurements to the inclusive  $v_2$  (right).

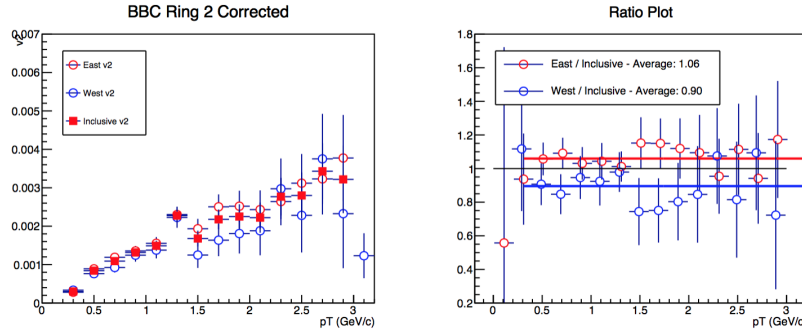


Figure A.29: BBCS event plane measurement with  $p+p/p+\text{Au}$  ratio correction and BBC ring 2 of  $v_2(p_T)$  with the for the  $p+\text{Au}$   $\sqrt{s_{NN}} = 200$  GeV (left) and the ratio of the east and west  $v_2$  measurements to the inclusive  $v_2$  (right).

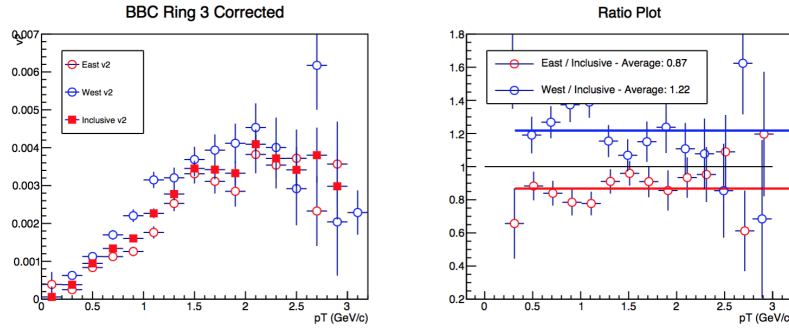


Figure A.30: BBCS event plane measurement with default correction and BBC ring 3 of  $v_2(p_T)$  with the for the  $p+\text{Au}$   $\sqrt{s_{NN}} = 200$  GeV (left) and the ratio of the east and west  $v_2$  measurements to the inclusive  $v_2$  (right).

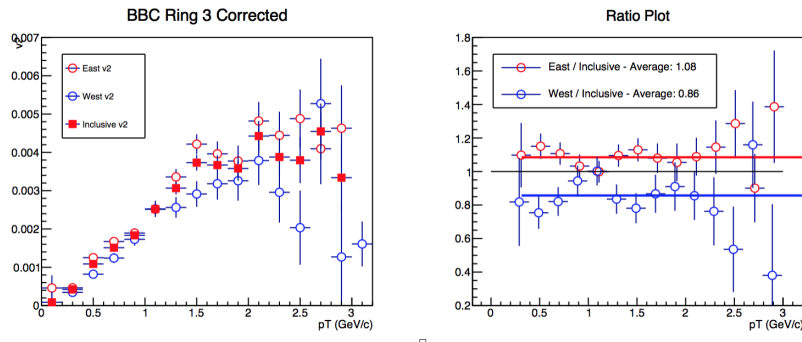


Figure A.31: BBCS event plane measurement with inverse charge correction and BBC ring 3 of  $v_2(p_T)$  with the for the  $p+\text{Au}$   $\sqrt{s_{NN}} = 200$  GeV (left) and the ratio of the east and west  $v_2$  measurements to the inclusive  $v_2$  (right).

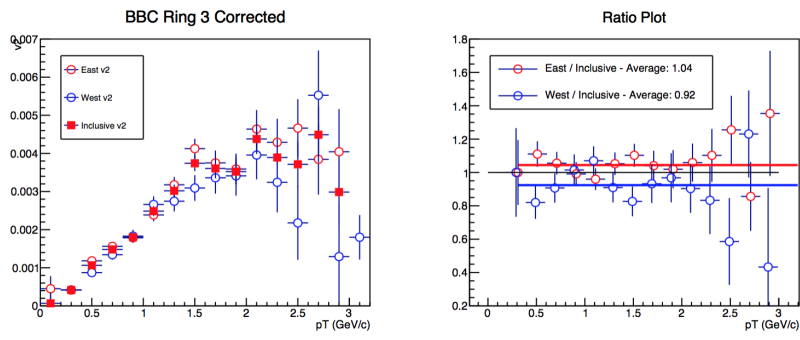


Figure A.32: BBCS event plane measurement with  $p+p/p+Au$  ratio correction and BBC ring 3 of  $v_2(p_T)$  with the for the  $p+Au$   $\sqrt{s_{NN}} = 200$  GeV (left) and the ratio of the east and west  $v_2$  measurements to the inclusive  $v_2$  (right).

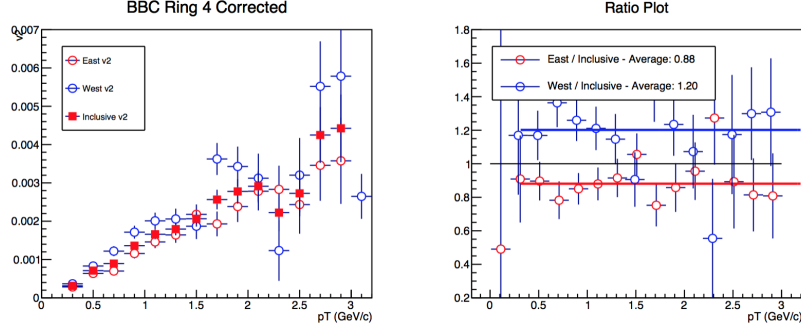


Figure A.33: BBCS event plane measurement with default correction and BBC ring 4 of  $v_2(p_T)$  with the for the  $p+\text{Au}$   $\sqrt{s_{NN}} = 200$  GeV (left) and the ratio of the east and west  $v_2$  measurements to the inclusive  $v_2$  (right).

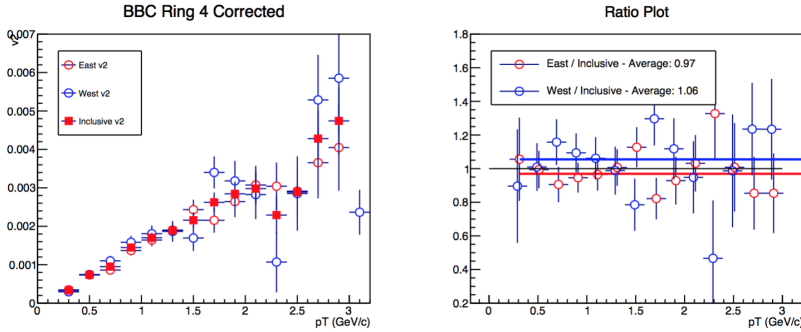


Figure A.34: BBCS event plane measurement with inverse charge correction and BBC ring 4 of  $v_2(p_T)$  with the for the  $p+\text{Au}$   $\sqrt{s_{NN}} = 200$  GeV (left) and the ratio of the east and west  $v_2$  measurements to the inclusive  $v_2$  (right).

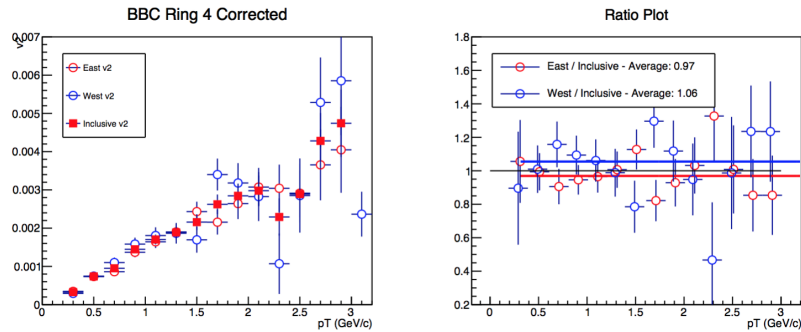


Figure A.35: BBCS event plane measurement with  $p+p/p+\text{Au}$  ratio correction and BBC ring 4 of  $v_2(p_T)$  with the for the  $p+\text{Au}$   $\sqrt{s_{NN}} = 200$  GeV (left) and the ratio of the east and west  $v_2$  measurements to the inclusive  $v_2$  (right).

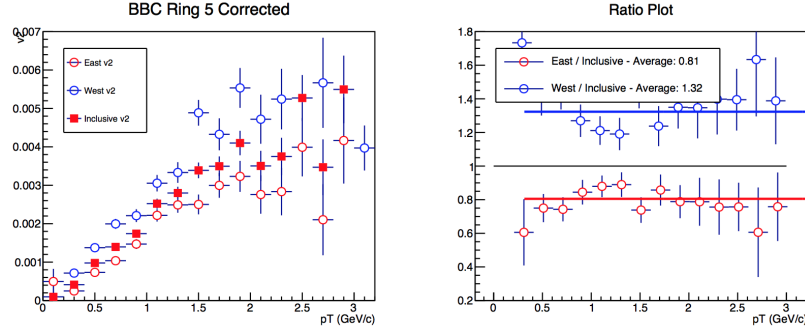


Figure A.36: BBCS event plane measurement with default correction and BBC ring 5 of  $v_2(p_T)$  with the for the  $p+\text{Au}$   $\sqrt{s_{NN}} = 200$  GeV (left) and the ratio of the east and west  $v_2$  measurements to the inclusive  $v_2$  (right).

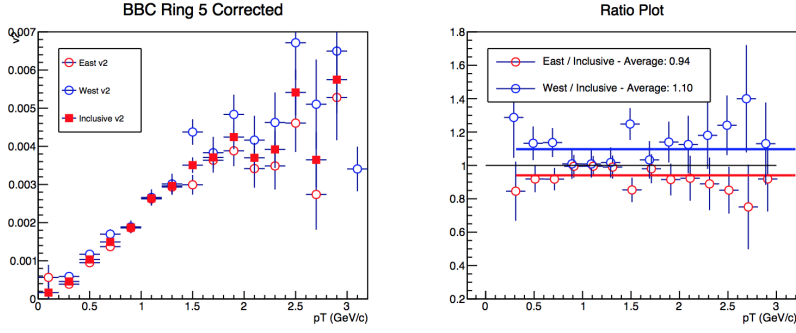


Figure A.37: BBCS event plane measurement with inverse charge correction and BBC ring 5 of  $v_2(p_T)$  with the for the  $p+\text{Au}$   $\sqrt{s_{NN}} = 200$  GeV (left) and the ratio of the east and west  $v_2$  measurements to the inclusive  $v_2$  (right).

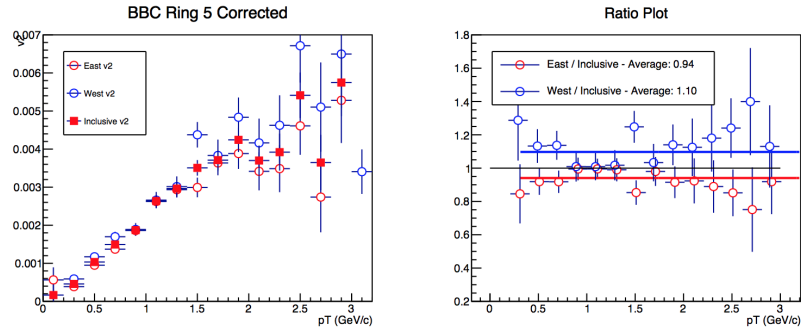


Figure A.38: BBCS event plane measurement with  $p+p/p+\text{Au}$  ratio correction and BBC ring 5 of  $v_2(p_T)$  with the for the  $p+\text{Au}$   $\sqrt{s_{NN}} = 200$  GeV (left) and the ratio of the east and west  $v_2$  measurements to the inclusive  $v_2$  (right).

## Appendix B

### Summary of Acronyms and Terms

QCD - Quantum Chromodynamics

QGP - Quark Gluon Plasma

$\sqrt{s_{NN}}$ - Center of mass energy per nucleon

$\sqrt{s}$ - Center of mass energy

$p_T$ - Transverse momentum

$p$ +Au- Proton and Gold collisions

$d$ +Au- Deuteron and Gold collisions

$^3\text{He}$ +Au- Helium-3 and Gold collisions

Au+Au- Gold and Gold collisions

$p+p$ - Proton and Proton collisions

$R_{\text{AA}}$ - Nuclear modification factor

RHIC - Relativistic Heavy Ion Collider

MeV - Megaelectronvolt (energy)

GeV - Gigaelectronvolt (energy)

TeV - Teraelectronvolt (energy)

$v_2$  - Elliptic flow

$v_n$  - Flow coefficient

SM - Standard Model of particle physics

QFT - Quantum Field Theory

QED - Quantum Electrodynamics

fm/c - Femtometer over speed of light (time)

$\sigma_{NN}$ - Nucleon nucleon cross section

$N_{\text{coll}}$ - Number of binary collisions

$N_{\text{ch}}$ - Number of charged particles

$\phi$  - Azimuthal angle

$\eta$  - Pseudorapidity

$\Psi_n$  - Event Plane angle

$\varepsilon_n$  - Nth order eccentricity

MC-Glauber - Monte Carlo Glauber

SONIC - Super hybrid mOdel simulatioN for relativistic heavy-Ion Collisions

AMPT - A Multi-Phase Transport (model)

PHENIX - Pioneering High Energy Nuclear Interaction Experiment

FVTX - Forward Vertex Tracking Detector

BBC - Beam Beam Counter Detector

CA - Central Arm Detectors

DAQ - Data Acquisition System

PMT - Photomultiplier Tube (BBC)